The University Of Sheffield.

Remote Sensing of Ocean Winds and Waves With Bistatic HF Radar

Rachael Louise Hardman

A thesis submitted in partial fulfilment of the requirements for the degree of Doctor of Philosophy

Supervisor: Professor Lucy R. Wyatt

University of Sheffield
School of Mathematics and Statistics
March 2019

To Ronda, my little chimp...

Abstract

High frequency, or HF, coastal radars collect a vast amount of data on ocean currents, winds and waves. The technology continuously measures the parameters, by receiving and interpreting electromagnetic waves scattered by the ocean surface. Formulating the methods to interpret the radar data, to obtain accurate measurements, has been the focus of many researchers since the 1970s.

Much of the existing research has been in monostatic radar theory, where the transmitter and receiver are stationed together. However, a larger, higher quality dataset can be obtained by utilising bistatic radar theory, whereby the transmitter and receiver are located at separate sites.

In this work, the focus is on bistatic radar, where the most commonly used mathematical model for monostatic radar is adapted for bistatic radar. Methods for obtaining current, wind and wave information from the model are then described and in the case of winds and waves, tested. Investigating the derived model shows that it does not always fit the real data well, due to undesirable effects of the radar. These effects can be incorporated into the model but then the existing methods used to obtain ocean information may not be applicable. Therefore, a new method for measuring ocean waves from the model is developed.

The recent advances in machine learning have been substantial, with the neural network becoming proficient at finding the link between complexly related datasets. In this work, a neural network is used to model the relationship between the developed radar model and the directional ocean spectrum. It is shown to successfully invert both monostatic and (for the first time) bistatic HF radar data and with this success, it becomes a viable option for obtaining ocean surface parameters from radar data.

Acknowledgements

Firstly, I must express my deepest gratitude to my supervisor, Professor Lucy Wyatt, who has been exceptionally generous with her time and wisdom. It goes without saying I couldn't have done this without you, Lucy, and I will remember your kindness every time I look in my garden and see the plants you gave me.

Thanks to all of the other lovely people in the School of Maths and at MASH who have been a joy to work with for the last 4 years. I've met some remarkable people in my time in Sheffield who I will miss working with a lot.

I am grateful to Dr. Daniel Conley and Dr. Guiomar Lopez at the University of Plymouth who provided us with the HF radar data and accompanying wave buoy data to carry out a validation of our method. Further thanks go to Dr. Celine Quentin at the Mediterranean Institute of Oceanography for the bistatic HF radar data and the patience to answer many questions. Also, many thanks to Dr. Yves Barbin who helped me with the details of the bistatic simulation process; he was so forthcoming and enthusiastic, it was a pleasure discussing the problem with him and his suggestions greatly improved the results.

To my two rocks, Hannah and Gabs, who are always there to provide a much-needed pep talk on the not so good days and to share a prosecco with on the great days. They're beyond best friends.

To my unbelievable family, the Hardmen and co., whose unwavering support (both emotional and financial (thanks for all of the orange juice Moomoo)) throughout my entire life means the world; thank you for everything. Also, thanks for pretending so well that you love all of the knitted presents I made for you in the lack of funding days.

Finally to my mentally synchronised partner, Ben. Thank you for not letting me dwell on the bad things in life, for all of your coding help, for your repertoire of songs and for making me laugh every day.

Rachael Hardman, March, 2019

Contents

List of Tables

List of Figures

Nomenclature

(R, θ, φ) radius, polar angle and azimuthal angle measured from the scatter point to the receiver

α_2 dimensionless character in the Pierson Moskowitz spectrum

β spread of the wind wave distribution in the sech directional model

δ angle between the Bragg bearing and a target's direction

ϵ_0 permittivity of free space

η normalised angular frequency, calculated by ω/ω_B

Γ_E electromagnetic coupling coefficient

Γ_H hydrodynamic coupling coefficient

γ_j parameter in the JONSWAP ocean wave spectrum $E_J(f)$

λ ocean wavelength

λ_0 radar wavelength

$\langle\rangle$ ensemble average

$\mathcal{F}(f(t))$ Fourier transform of a function $F(t)$

μ_0 permeability of free space

ν absolute target velocity

ν degrees of freedom

ν_E velocity component in the elliptical direction

ν_R radial velocity of a target

ω angular frequency

ω_0 angular frequency of the emitted radio waves

ω_B Bragg frequency

φ_{bi} bistatic angle

$\Phi(\omega)$ power spectral density over frequency ω

φ_i radar beam angle, measured clockwise from north, for radar number i

σ radar cross section

$\sigma^{(1)}(\omega)$ first order radar cross section over frequency ω

$\sigma^{(2)}(\omega)$ second order radar cross section over frequency ω

σ_0 signal power

$\sigma_B(\omega)$ bistatic radar cross section

σ_c ocean conductivity

$\sigma_M(\omega)$ monostatic radar cross section

σ_s spreading angle

$\sigma_{\cos}$ spread of the $\cos^{2s}$ directional model, in degrees

σ_{sech} spread of the *sech* directional model, in degrees

θ arbitrary angle

θ^* mean wind direction

θ_1 angle between the positive p axis and the wavevector $\mathbf{k_1}$

θ_2 angle between the positive p axis and the wavevector $\mathbf{k_2}$

θ_m mean wave direction

θ_p peak wave direction

$\triangle r$ range resolution of the radar

$\triangle$ effective surface impendance

$\triangle\tau$ time delay of a signal between adjacent antennas

φ_{bi} bistatic angle

$\hat{\mathbf{a}}$ unit vector in the direction of the receiver from the scatter patch

$\hat{\mathbf{k}}_{\mathbf{0}}$ radar unit wavevector (unit vector in the direction of the scatter patch from the trasmitter)

$\mathbf{E}$ electric field

$\mathbf{k_0}$ radar wavevector

a scattering surface wavenumber

$A(\theta, t)$ time signal received at the radar from direction θ at time t

a_1 first Fourier coefficient of the ocean spectrum

A_{mnl}, B_{mnl}, etc. scattered field Fourier coefficients in terms of integers m, n and l

b_1 first Fourier coefficient of the ocean spectrum

B_w bandwidth

$B_{\pm}$ positive and negative Bragg peak values (denoted by the $+$ and $-$ subscript, respectively)

c speed of light

c_p phase speed

D normalisation factor for directional ocean wave spectra

d distance between antennas

d ocean depth in metres

$E(f)$ non directional ocean spectral density at wave frequency f

$E(k)$ non directional ocean spectral density at wavenumber k

E_0 incident electric field strength

E_θ vertically polarised component of the electric field

$E_J(f)$ JONSWAP ocean wave spectrum in terms of frequency f

E_s scattered electric field strength

$E_x()$, $E_y()$, $E_z()$ x, y and z components of the electric field $\mathbf{E}$ (sometimes subscripted with an additional ' or superscripted with (i) or (s) to denote incident and scattered fields)

$E_{PM}(f)$ Pierson Moskowitz spectrum in terms of ocean wave frequency f

f frequency

$f(x, y, t)$ ocean surface height at location x and y at time, t

f_B bistatic Doppler shift

f_d frequency shift caused by the motion of a target, for a FMCW radar

f_M monostatic Doppler shift

f_p peak frequency

f_t frequency difference between the transmitted and received signals, for an FMCW radar

g acceleration due to gravity

$G(f, \theta)$ normalised directional distribution to model the directionality of the ocean wave spectrum

G_r receiver gain

G_t transmitter gain

h_s significant waveheight

k wavenumber

k_0 radar wavenumber

k_B Bragg wavenumber

k_i ocean wavenumber

L scattering surface spatial period

L_f ocean fetch

L_r propagation losses over the receiver-to-target path

L_s radar system losses

L_t propagation losses over the transmitter-to-target path

N number of antennas

p wavenumber in the x direction

$P(m,n,l)$ ocean surface Fourier coefficients in terms of integers m, n and l (sometimes superscripted to denote the order)

p_f pulse repetition frequency

P_r received power

P_t transmitted power

q wavenumber in the y direction

R Bragg peak ratio

R range from the radar to the scatter point

R_B range of a target, for a bistatic radar

R_M range of a target, for a monostatic radar

R_R distance from the scatter point to the receiver

R_T distance from the scatter point to the transmitter

s spread of the wind wave distribution in the cos^{2s} directional model

$S(\mathbf{k})$ directional ocean wave density at wavevector $\mathbf{k}$

$S(f,\theta)$ ocean spectral density at wave frequency f travelling in direction θ

$S(k,\theta)$ ocean spectral density at wavenumber k travelling in direction θ

$S_s(k_x,k_y)$ or, equivalently, $S_s(\mathbf{k})$ surface roughness spectrum in terms of wavenumbers k_x and k_y or, equivalently, in terms of vector k where $\mathbf{k}=(k_x,k_y)$

$S_s(k_x,k_y,\omega)$ surface roughness spectrum in terms of wavenumbers k_x and k_y, and frequency ω

T scattering surface time period

t time

t_0 sampling interval

t_E energy period

t_p	peak period
U_{10}	wind speed 10 metres above the ocean surface
w	scattering surface angular frequency
w_l	l^{th} component of a window function
$x(t)$	function x at time t
z	ocean surface height
Z_s	conductor surface impendance
SNR	signal to noise ratio

Introduction

Research Background

Covering over 70% of the Earth's surface, the ocean is imperative to life. The ocean regulates our climate, is a key food source, provides renewable energy, is a vital part of many countries' economies and is a hub of recreation and beauty. It can also cause devastation; when a home is lost to the ocean due to coastal erosion, when a tsunami hits, or when its climate-change-driven rising temperatures and ocean levels cause flooding and freak weather events. Gaining insight into its behaviour can help us to harness or counter its power. High frequency, or HF (3-30 MHz), coastal radars are a tool that can provide such insight, by either analysing the datasets of ocean surface parameters derived from the radar data or assimilating the measurements into wave models, the importance of which has been documented by Cavaleri *et al.* [14].

HF radars can continuously provide information about the ocean, exceeding distances of 200 km from the coast, with high resolution. Compared to a wave buoy, which only provides data in one location, or a satellite, which only provides data sporadically, it is an attractive option as long as the information is accurate.

In 1955, Crombie [19] hypothesised about the relationship between the ocean and HF radar signals. He backed his claim up numerically but it was not formally proven until 1972, when Barrick [5][7], applied the perturbation analysis of Rice [78] to the moving ocean and presented the radar cross section of the ocean, to second order, in terms of the ocean spectrum. Since then, many researchers have formulated methods for inverting Barrick's equations, to obtain accurate ocean information on currents, winds and waves from HF radar data.

The radar cross section expression of Barrick [5][7] is only applicable to monostatic radar, whereby the transmitter and receiver are co-located. A bistatic radar, on the other hand, corresponds to a radar where the transmitter and receiver are separated by a distance, so that the scatter is reflected at some angle, θ. The advantages of employing such a radar

setup are (1) it can reduce the cost of setting up/maintaining a HF radar and (2) it can increase spatial coverage and data quality as shown by Whelan & Hubbard [99].

In 1975, Johnstone [50] and then, in 2001, Gill and Walsh [27] presented radar cross section expressions of the ocean surface for bistatic radar. However, neither of the expressions reduce exactly to the monostatic term of Barrick [5][7] (which many operational radar inversion programs depend on) when $\theta = 0$. Johnstone's derivation appears to have a notable error which causes the difference in the resulting expressions; Gill and Walsh followed a more complicated method, however, it has been shown that the monostatic form of their radar cross section is similar to Barrick's and it is, therefore, unnecessary to adapt the existing operational monostatic inversion programs, which are based on Barrick's expression, to use theirs instead.

A bistatic radar cross section that reduces exactly to the monostatic term of Barrick [5][7] would be beneficial to systems that are based on Barrick's expression as, in the radar coverage area, the scattering angle θ can vary between 0° and 90°, so the discontinuity between the monostatic and bistatic radar cross section expressions would cause a discontinuity in the inversion program used and perhaps, then, the results. Therefore, in this work, we follow the method of Barrick, whilst retaining θ, to derive the bistatic radar cross section of the ocean surface.

Inversion methods for obtaining current, wind direction and wave measurements, historically applied to monostatic radar data, are then described. The theory of obtaining bistatic current measurements is included for completeness, however, no experimental results are presented in this work. In the case of wind direction measurements, the maximum likelihood method of Wyatt *et al.* [108] is adapted and used to obtain wind directions from a bistatic radar dataset.

Wyatt *et al.* [109] outlined the limitations of the wave inversion methods when large sidelobes are coupled with a strong surface current. When this happens, the radar cross section model does not apply and therefore the existing wave inversion methods - which are based on the radar cross section model of Barrick [5][7] - cannot reliably invert these data. A similar problem has been shown to occur for bistatic HF radars by Grosdidier *et al.* [29], when a radar has low spatial resolution and one wishes to analyse the signal measured at a location where the value of θ varies substantially. At such a location, an assumption made in the derivation of the radar cross section expression is invalid and thus, again, the inversion methods cannot reliably invert these data. Grosdidier *et al.* attempted to model the expected radar return in such a situation, by including the effects of the radar, and achieved good results. However, no attempt has yet been made at inverting the model.

In this work, a method different from that of Grosdidier *et al.* [29] is proposed to model both

monostatic and bistatic radar data that includes the radar effects. A method for inverting the model is then proposed and tested. The proposed model is not expressed analytically, due to its complexity, and hence finding an analytical/numerical solution is not feasible. Artificial neural networks have become increasingly popular when one wishes to find the mapping between two datasets with a complex relationship, and they are hence tasked, here, with inverting the proposed radar data model to obtain the directional ocean spectrum. To test the method, a neural network is trained using simulated radar data and then a measured radar dataset is inverted and the results compared to those from a directional wave buoy; this experiment is carried out for monostatic radar data, where the radar effects are not included, and bistatic radar data, where the radar effects are included.

Research Aims

To summarise, the research aims of this thesis are:

1 To derive an expression for the bistatic radar cross section of the ocean surface which reduces to the monostatic expression of Barrick [5][7], when $\theta = 0$.

2 To model bistatic radar data where the radar effects are included.

3 To infer values of ocean surface parameters - namely wind direction and directional wave spectrum information - from bistatic radar data.

4 To see whether machine learning, in particular, artificial neural networks, can be used to estimate ocean surface parameters from HF radar data.

Thesis Outline

Chapter 1 gives an introduction to both radar theory and oceanography as well as a brief history of how HF radar is used to remotely measure ocean surface parameters.

In Chapter 2, an expression for the bistatic radar cross section of the ocean surface is derived, analogously to the method of Barrick [5][7] where the equivalent monostatic radar cross section was derived. The limitations of the theory are discussed and the derived term is shown to reduce to the monostatic expression of Barrick under the appropriate scattering conditions.

In Chapter 3, the bistatic radar cross section is numerically calculated so that one can simulate the expected radar return for any directional ocean spectrum. A new simulation method is then proposed which includes the effects of the radar and the local geography, which are shown

to substantially affect some bistatic HF radar data. Both simulation methods are validated using measured radar data.

Chapter 4 gives an overview of inversion methods for currents, wind directions and waves. A new inversion method for obtaining wave information from HF radar data is then proposed, which uses an artificial neural network trained on simulated HF radar data. To accompany the proposed method, an introduction to neural networks is given.

In Chapter 5, the results of the inversion experiments are presented. Firstly the maximum likelihood method of Wyatt *et al.* [108], is tested on bistatic HF radar data and the results are validated with ASCAT scatterometer data. Secondly, the artificial neural network wave inversion method for two experimental datasets is tested: (1) Monostatic radar data and (2) Bistatic radar data where the effects of the radar are substantial. In both cases, the results are validated using directional wave buoy data.

Finally, in Chapter 6, the key findings of the work are summarised and the scope for any future work is discussed.

Chapter 1

Introduction to Remote Sensing of the Ocean Using HF Radar

§ 1.1 Introduction to Radar

In 1866, the notion of a radar became a possibility when the theories of Maxwell were experimentally tested by Heinrich Hertz, who demonstrated that radio waves embody the same characteristics as light waves. Hertz showed that analogous to light waves, radio waves can be reflected by metallic bodies. These reflected waves contain information about the target, as was then shown in the key works of Hülsmeyer [47], Marconi [65] and Taylor *et al.* [87], and their theory was first utilised in World War II when the *radar* was established.

When a radio wave hits an object, it is reflected - or *reradiated* - in many different directions. The reflecting of a radio wave off a target is the fundamental idea behind radar. To detect a target, a radar transmitter emits radio waves, towards the reflecting object which then scatters the wave. The portion of energy that radiates back to the radar, is picked up by the receiving antennas and is then directed into the processor, which transforms the data into a meaningful form. The output data contains information such as the distance, direction and speed of a target, which has many direct applications.

Radar has been used in many applications since detecting enemy vessels in WWII. A few notable examples are air traffic control, speed guns, weather monitoring [70], remote sensing of the Earth e.g. project RADAM (mapping of the Amazon rainforest) [93], oil/gas discovery [95], underground probing [16] and, as studied in this work, ocean sensing [107].

In this section, important aspects of radar, relevant to the chapters to follow, will be introduced; the differences between monostatic and bistatic radar will be made clear and methods

for obtaining information from the two radar setups will be presented. For further information, more rigorous accounts of radar theory and its history can be found in the works of Skolnik [81][82], Kingsley and Quegan [53] and, with an emphasis on bistatic radar, Willis [100].

1.1.1 Radar Setup

A radar can be monostatic, where the transmitter and receiver are co-located or it can be bistatic, where the transmitter and receiver are situated some distance apart. The combination of both, i.e. having one receiver and multiple transmitters or vice versa is called a multistatic radar. The geometry of monostatic and bistatic radars is shown in figure 1.1 and a possible multistatic setup, for two transmitters and one receiver is shown in figure 1.2.

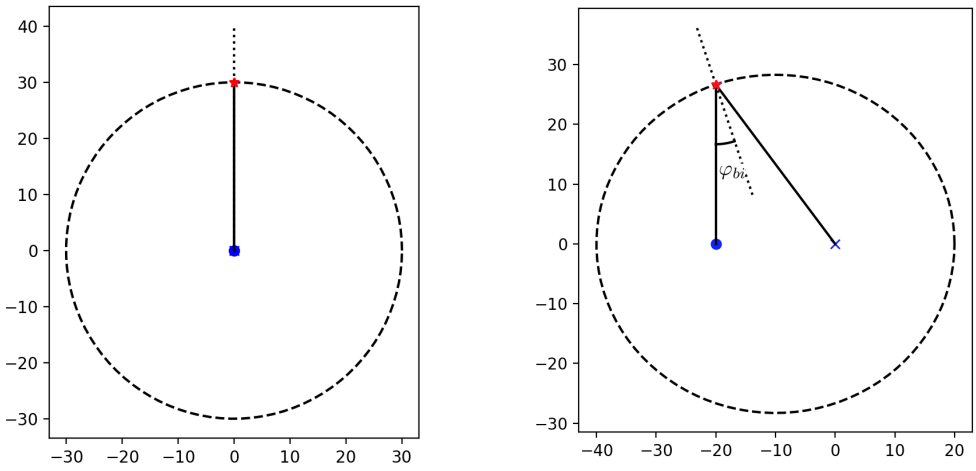

(a) Monostatic (b) Bistatic

Figure 1.1: Comparison of monostatic and bistatic radar geometries. In both cases, the transmitter is shown at point $(0, 0)$ and the receiver is shown by the blue circle (which, in the monostatic case, is also at point $(0, 0)$). An example scatter point is shown by the red star and the path the signal takes is shown by the solid black line. The line of constant range for each particular range is shown by the dashed black line and the angle shown, φ_{bi}, is the bistatic angle.

For a monostatic radar, a transmitted signal hits a target and the received signal is backscatter. The lines of constant range are therefore circles around the radar location where the signal has travelled a distance of twice the radius of the circle. On the other hand, for a bistatic setup, the transmitted signal hits the target and the received signal is no longer backscatter, it is the signal scattered at a non-zero angle, here $2\varphi_{bi}$ (for the *bistatic angle* φ_{bi}) as shown in figure 1.1, in the direction of the transmitter. The lines of constant range are ellipses, where the transmitter and the receiver are located at the foci of the ellipse; see figure 1.3 for the

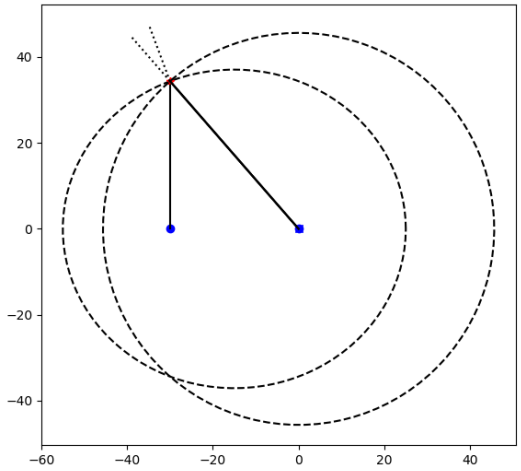

Figure 1.2: Possible multistatic radar geometry including one transmitter and receiver operating in monostatic mode (shown at point $(0, 0)$) and a further transmitter, situated a distance away, at point $(-30, 0)$, operating in bistatic mode. An example scatter point is shown at the intersection of the two dashed rings - both of which represent a line of constant propagation distance.

lines of constant range for both monostatic and bistatic radars.

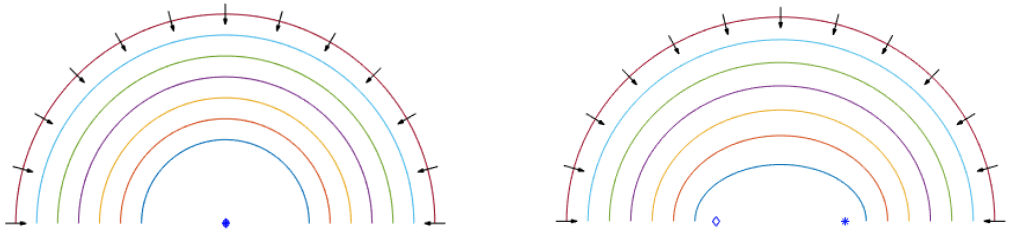

(a) Monostatic (b) Bistatic

Figure 1.3: Lines of constant propagation distance for a monostatic and bistatic radar. In both cases, the ranges are in 10 km increments from 40 km to 100 km. The transmitter and receiver are shown by the markers where, for the bistatic radar, they are separated by a distance of 30 km. The Bragg bearings, as discussed in section 1.1.2, for different radar beams are shown by the arrows.

1.1.2 Calculating Target Distance, Speed and Direction

For monostatic and bistatic radars, the different geometries mean that the calculations for a target's distance, speed and direction are different.

The distance is conventionally measured as the distance from the radar to the target (in the case of monostatic radar), however, for bistatic radar, this must be altered to account for the

separated sites. This is also the case when calculating the speed and direction of a target. When a radio wave interacts with a moving object, the motion of the object causes a change, or shift, in the frequency of the incident radio wave. This is due to the *Doppler effect*. The magnitude of the frequency shift depends on the speed and the propagation direction of the target and also the radar setup.

1.1.2.1 Monostatic

The distance to the target from the radar, R_M, is found by calculating

$$R_M = \frac{ct}{2}, \tag{1.1}$$

where c is the speed of light and t is the time the signal takes to travel from the transmitter to the object and then back to the receiver.

For a monostatic radar, if the object is travelling toward the receiver, the returned signal will be emitted from a point closer to the radar meaning each successive wave will take less time to travel back to the receiver than the one before. This means that the frequency of the returned signal increases and thus a positive shift occurs. Analogously, an object travelling away from the receiver will cause a negative shift. The monostatic Doppler shift, $\triangle f_M$, of a radio wave when interacting with a moving object is found by calculating [82]

$$\triangle f_M = \frac{2\nu_R}{\lambda_0}, \tag{1.2}$$

where $\triangle f_M$ is in Hz, ν_R is the velocity of the object in the radial direction, in m/s, and λ_0 is the wavelength of the transmitted signal, in metres. Rearranging equation 1.2 gives ν_R in terms of the measurable $\triangle f_M$ and thus one can measure a target's speed. Furthermore, the radial velocity is related to the actual velocity of the target, ν, by

$$\nu_R = \nu \cos\theta,$$

where θ is the angle between the direction of motion and the radar beam.

The direction of motion relevant to the Doppler shift (in this case, the radial direction) is henceforth called the *Bragg bearing*. An object moving perpendicularly to the Bragg bearing will cause no change in frequency as there is no movement towards or away from the radar, in this case, i.e. $\cos\theta = 0$. Additionally, for one radar with one measurement, the velocity ν cannot be resolved; to resolve the direction, one can use multiple radars in different locations.

1.1.2.2 Bistatic

The distance to a target, R_B, as measured by a bistatic radar is calculated by

$$R_B = \frac{1}{2}(R_R + R_T), \tag{1.3}$$

where R_R and R_T are the distances from the receiver and transmitter to the scatter point, respectively. If $R_R = R_T$, then $R_B = R_M$, from equation 1.1, as expected.

From Willis [100], the bistatic Doppler shift, $\triangle f_B$, is defined by

$$\triangle f_B = \frac{1}{\lambda_0}\left(\frac{d}{dt}\left(R_T + R_R\right)\right). \tag{1.4}$$

As $\frac{dR_R}{dt}$ and $\frac{dR_T}{dt}$ define the rate of change of the target's distance from the receiver and transmitter, respectively, they are equivalent to the target's velocity, ν, projected onto the respective paths. Therefore, defining δ as the angle between the Bragg bearing and the target's direction as shown in figure 1.4,

$$\frac{dR_R}{dt} = \nu\cos(\delta + \varphi_{bi}) \quad \text{and} \quad \frac{dR_T}{dt} = \nu\cos(\delta - \varphi_{bi})$$

which, upon substitution into equation 4.2, gives

$$\triangle f_B = \frac{2\nu}{\lambda_0}\cos\delta\cos\varphi_{bi}.$$

By letting $\nu_E = \nu\cos\delta$, namely the velocity component in the elliptical direction, the Doppler shift, in Hz, can be written as

$$\triangle f_B = \frac{2\nu_E\cos\varphi_{bi}}{\lambda_0}. \tag{1.5}$$

Therefore, in this case the Bragg bearing is in the elliptical direction as shown in figures 1.1, 1.3 and 1.4. In equation 1.5, under monostatic conditions (when $\cos\varphi_{bi} = 1$), $\triangle f_B = \triangle f_M$ from equation 1.2 as expected.

1.1.3 Waveforms

Radar systems are designed to emit radio waves in a particular form depending on the purpose. Perhaps the most simple type is the *pulse radar*. In a pulse radar, the transmitting antenna is switched on for a predetermined amount of time to emit waves. It is then switched off for another set time whilst the receive antenna is switched on to receive the scattered waves.

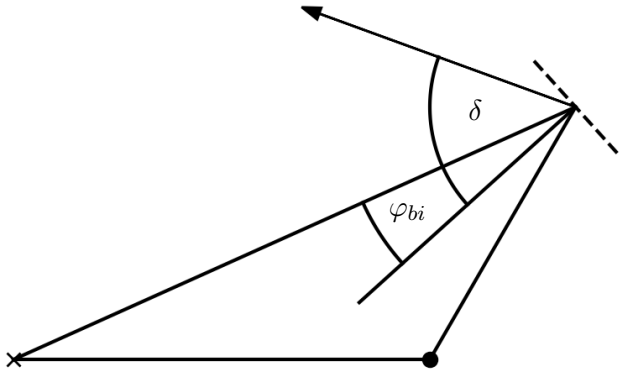

Figure 1.4: Geometry for calculating the bistatic Doppler shift. The transmitter and receiver are shown by the cross and the circle respectively, the third triangle vertex is at the scatter point. The arrow depicts the target velocity and the bistatic angle is shown by φ_{bi}. The Bragg bearing is shown perpendicular to the dashed line and δ is the angle measured from this to the direction of motion of the target.

The reason for this alternating process is to avoid interference between the transmitted and scattered signals; if the radar was both sending and receiving signals at the same time, they would be hard to separate. The duration of the pulse must be long enough to ensure that echoes from all possible ranges are received; if the duration of the pulse is too short, echoes from more distant targets may arrive during sequential pulses causing ambiguities in the received data. For a certain number of pulses per second sent (i.e. the *pulse repetition frequency*), p_f, the maximum unambiguous range, R, is

$$R = \frac{c}{2p_f}.$$

Alternatively, a continuous signal of a fixed frequency can be emitted. This is known as a *continuous waveform* (CW). In this case, the transmitting and receiving antennas are both constantly on so isolating the return signal is a greater challenge than for a pulse radar. The benefit of using a CW is that the mean power is higher and so greater distances can be achieved. However, as there is no time mark, the distance to the target cannot be calculated and, thus, this mode is not ideal for most radar applications. To enable distance calculations, the signal must be modulated in some way. The signal can be modulated in either amplitude or frequency (AM or FM radio waves). In ocean radar, frequency modulated continuous waveforms (FMCW) and frequency modulated interrupted continuous waveforms (FMiCW) are used and are described below.

An FMCW is a continuously emitted signal of varying frequency. The emitted signal is

'swept' through a range of frequencies - the size of which is the bandwidth of the signal - in a repeated pattern. The distance to the target is found by detecting the frequency difference, $\triangle f_t$, between the transmitted and received signals, where echoes from targets close to the radar return with a smaller change in frequency than those coming from further away. Any motion of the target imparts an additional shift of $\triangle f_d$ to the signal. Figure 1.5 depicts how the two shifts affect the incident waveform. Sawtooth modulation is shown in the figure, although there are a number of other modulation forms.

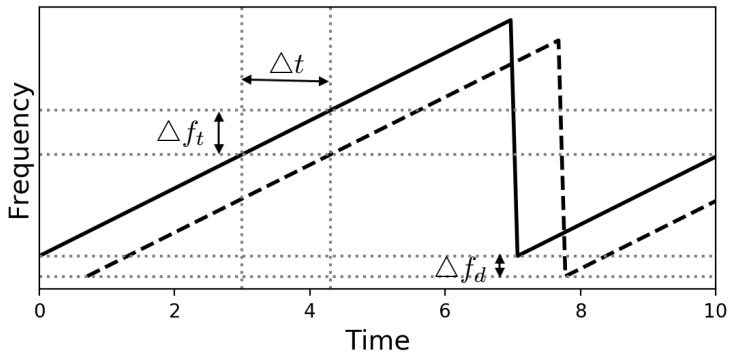

Figure 1.5: A frequency modulated continuous waveform, with linear sawtooth modulation. The emitted waveform is shown by the solid line and the received, shifted, waveform by the dashed line. The time delay is denoted by $\triangle t$ and the frequency shift associated with $\triangle t$ is denoted by $\triangle f_t$. The frequency shift caused by the motion of the target is denoted by $\triangle f_d$.

The main drawback of FMCW radar is that the transmitted signal will leak into the receiver. To reduce the transmitter noise, two methods can be used in HF radar systems. Firstly a null can be created in the direction of the receiver, which cancels out the transmitted signal. However, this process is never perfect and thus is a motivation of bistatic radar, where the null is not as important due to the increased distance between the transmitter and receiver. Secondly, the transmitted waves can be 'interrupted', where - like a pulse radar - the transmitter is intermittently switched off in order to receive signals. More commonly known as FMiCW radar, higher transmission power can be used meaning greater distances can be achieved.

In this work, data from two HF FMCW radars are used.

1.1.4 Wave Propagation

Wave propagation describes how a radio wave travels from one point to another; the frequency (where a wave is classified as shown in table 1.1), the polarisation and the mode - whether it be direct (line-of-sight), along the Earth (ground wave) or via reflection from the ionosphere (sky

wave) - are all defining characteristics. These characteristics affect how far the radio waves can travel and what types of object they can detect, due to processes such as polarization, reflection and diffraction. Therefore, depending on the radar application, one must choose appropriate wave characteristics.

Both ground waves and sky waves are used in HF radar for remote sensing of the ocean. In sky wave propagation, the transmitted wave is reflected off the ionosphere, which is the layer of the Earth's atmosphere made up of ionised, or charged, atoms. At some HF frequencies the ionosphere becomes a reflective surface for the waves and Maresca *et al.* [66] and Georges *et al.* [26] have shown that good measurements of sea state can be achieved through skywave radar. Barrick [6], however, states that the window where propagation via the ionosphere is possible is fairly small, in the HF band, and even then it can be unusable due to the randomness of the charged particles. Due to this, ground wave radars are more commonly used in this application; they are also assumed in this work.

In ground wave propagation, the radio waves propagate along a path following the curvature of the Earth by interacting with the conductive properties of the ground/sea. As the wave travels, it is attenuated due to a number of factors. One of the major contributing factors is frequency, where a higher frequency constitutes a greater loss of energy. The conductivity of the ground, which is positively correlated with the salinity level of the water, also affects how well the wave can propagate via ground wave. The more conductive the ground, the less energy will be attenuated and so greater distances can be reached. Therefore, the ocean - a highly conductive medium - is ideal. Polarisation, which represents the orientation of the electric field in the radio wave, is also a contributing factor. Vertical polarisation (i.e. a wave with a vertical electric field) is much more suitable for ground wave propagation as the electric field of a horizontally polarised wave would short circuit due to the conductivity of the ground and hence not be able to sustain energy over any notable distance.

Frequency	Band
30 GHz - 300 GHz	Extremely High Frequency - EHF
3 GHz - 30 GHz	Super High Frequency - SHF
300 MHz - 3 GHz	Ultra High Frequency - UHF
30 MHz - 300 MHz	Very High Frequency - VHF
3 MHz - 30 MHz	High Frequency - HF
300 kHz - 3 MHz	Medium Frequency - MF
30 kHz - 300 kHz	Low Frequency - LF
3 kHz - 30 kHz	Very Low Frequency - VLF

Table 1.1: Radio wave bands.

1.1.5 Radar Resolution

The accuracy with which a radar can resolve where a scattered signal has arrived from is known as the *spatial resolution* of the radar. Spatial resolution can be divided into two categories; range resolution and azimuthal resolution.

The range resolution of a radar, $\triangle r$, is defined as the distance that the radar can distinguish measurements from. For an FMCW wave with chosen bandwidth, B_w kHz, the range resolution in km is found by calculating

$$\triangle r = \frac{c}{2B_w}, \tag{1.6}$$

where $c \approx 300$ ms^{-1}. Therefore, to get finer resolution, one needs higher bandwidth.

The bandwidth is specified by the operator but must be licensed by the local government and, generally, the wider the bandwidth, the more vulnerable it is to interference from other radio waves. This means it can be hard to achieve broader bandwidths; at frequencies under 10 MHz it can be challenging to get more than 50 kHz of bandwidth [101].

The azimuthal resolution is analogous to range resolution but the physical distance that the angular resolution represents will increase with range. The resolution depends on the size of the main lobe of the antenna pattern, which in turn depends on the type of receiver and the signal processing methods used.

For remote sensing of the ocean, there are two main types of receiver (1) compact radar (2) phased array radar. The main difference between the two radar systems is how they direct the radar beam. The phased array system creates a narrow - more concentrated - beam, directed in a desired direction, whereas the compact system directs a broad beam.

For a phased array radar, the antenna pattern is governed by how the receiving antennas are set up. The receiver consists of a number of antennas usually placed in a straight line, perpendicular to the direction required for the main radar beam, with (ideally) $\lambda_0/2$ spacing, for radar wavelength λ_0. Then, to create a narrow beam, a process called beamforming, as explained in section 1.1.6, can be used. Direction finding methods are an alternative option and details can be found in the work of Gurgel *et al.* [30].

In the case of the compact radar, beamforming cannot be used and the received signal must be processed using direction finding methods.

1.1.6 Beamforming

In a phased array radar, each antenna receives a time series of complex valued amplitudes from signals returning from a number of directions. At antenna j, the received discrete signal, $A_j(t)$, can be written as

$$A_j(t) = \sum_{l=0}^{M-1} x_j(t)\delta(t - lt_0), \tag{1.7}$$

where M is the number of samples taken, t_0 is the sampling interval and $x(t)$ is the signal measured at time t. To filter the signal received from a desired direction, the time series must be combined in a particular way. One method is *beamforming*, which delays each time series by a specific amount to separate the signals.

If a plane wave is parallel to and travelling towards the linear array of antennas, it will reach the antennas at the same time. However, if it is travelling at an angle θ, which is not parallel to the array (see figure 1.6 for orientation), the signal will arrive at the antennas at different times. For an equispaced array with spacing d between the antennas, the extra distance the signal must travel between antennas, $\triangle d$, is

$$\triangle d = d \sin\theta.$$

Therefore, the time delay between adjacent antennas[1] is

$$\triangle\tau = \frac{d \sin\theta}{c}. \tag{1.8}$$

To get the signal from a direction θ (as shown in figure 1.6), the signals expressed in equation 1.7 are delayed by an amount proportional to their distance from the end of the array before they are summed. The time delay at antenna j is given by $j\triangle\tau$, where $\triangle\tau$ is given in equation 1.8. Thus, the time domain signal received from a direction θ is given by

$$A(\theta, t) = \sum_{j=0}^{N-1} \sum_{l=0}^{M-1} w_j x_j(t - j\triangle\tau)\delta(t - lt_0 - j\triangle\tau), \tag{1.9}$$

where w_j is an amplitude weight at antenna j used to control the width of the mainlobe and to minimise the sidelobes, by tapering the complex signals to avoid spectral leakage as explained by Harris [34]. The weights w are values from a *windowing function* and there are a number of different possible windows; three commonly used windows are shown in figure 1.7.

[1] Note that if the array is not linear and/or not equispaced, then a different formula for $\triangle t$ must be used.

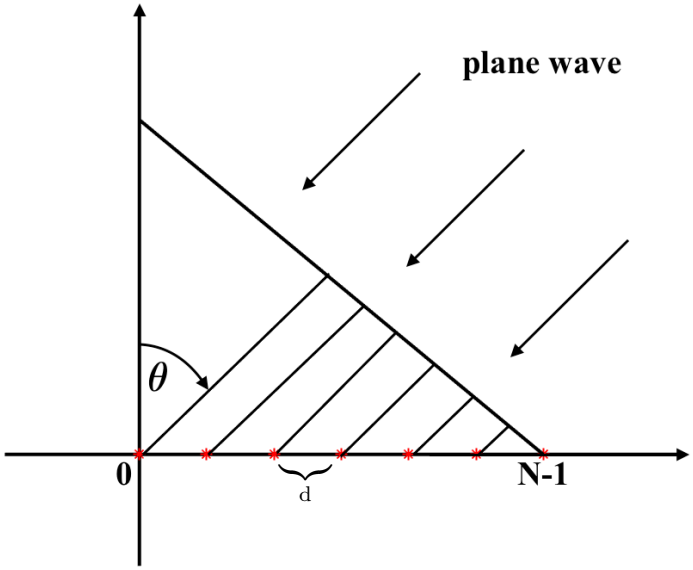

Figure 1.6: Beamforming geometry for a plane wave with angle of arrival, θ, and N antennas as shown by the crosses along the x axis, with spacing d.

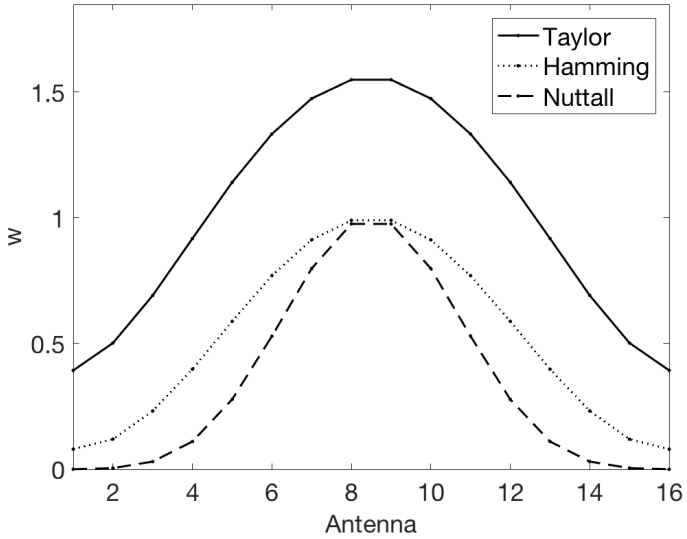

Figure 1.7: Different windowing functions as described by Harris [34], for a receive array comprising 16 antennas. In each case, a 16 point sample of the function has been taken to show the weight at each antenna.

A delay in time in the time domain is equal to a phase shift in the frequency domain, such

that

$$\mathcal{F}\{g(t-a)\} = G(f)\mathrm{e}^{-2\pi i f a}, \tag{1.10}$$

where a is the time shift and $G(f)$ is the Fourier transformed $g(t)$. Furthermore, a useful property of the delta function is

$$\mathcal{F}\{f(t)\delta(t-t_0)\} = f(t_0)\mathrm{e}^{-2\pi i f t_0} \tag{1.11}$$

which, alongside equation 1.10, gives the Fourier transform of the time delayed signal, from angle θ, in equation 1.9, as

$$\mathcal{F}\{A(\theta,t)\} = \sum_{j=0}^{N-1}\sum_{l=0}^{M-1} w_l w_j x_j(lt_0)\mathrm{e}^{-2\pi i f j \triangle\tau}\mathrm{e}^{-2\pi i f l t_0}, \tag{1.12}$$

where w_l is the l^{th} component of a second windowing function, this time applied across the time series to minimise spectral leakage when the Fourier transform is taken. Figure 1.8 shows the beam patterns for two phased array radars, each with a different number of antennas, where the above beamforming method has been used.

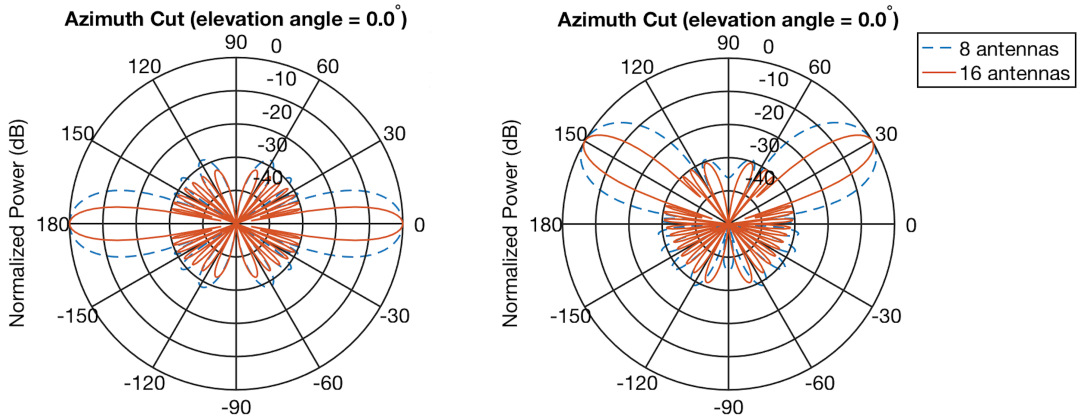

(a) 0° (b) 30°

Figure 1.8: Beam patterns for two linear phased array radars, with 8 and 16 antennas, operating at 16.512 MHz with $\lambda_0/2$ antenna spacing for radar wavelength λ_0. A phased shift beamformer with a Taylor window has been used to steer the beam to 0° and 30° (noting that boresight - namely the direction perpendicular to the antenna array - is at 0°).

1.1.7 Radar Cross Section and the Radar Equation

The term that defines the relationship between a target and the amount of energy it scatters is the *radar cross section*, σ. With units of area (m^2), it measures how much power a target will re-radiate in a particular direction (usually toward a receiver). The value of σ depends on the characteristics of the target such as its size, shape, reflectivity and electrical properties. If the properties of the target are such that it reflects all of the incident power isotropically, then the radar cross section would be equal to the target's cross-sectional area as seen by the transmitter. However, this is not usually the case and more importantly, for this work, it is not true for the scattering of radio waves off the ocean surface. To find σ for a scatterer such as the ocean, Skolnik [81] defines the radar cross section as

$$\sigma = \lim_{R\to\infty} 4\pi R^2 \frac{|E_s|^2}{|E_0|^2}, \tag{1.13}$$

where R is the distance from the target to the receiver, E_0 denotes the strength of the electric field of the incident wave and E_s denotes that of the scattered wave. The radar cross section alone does not provide the measurement one would expect to receive at a radar though, as other factors (such as attenuation of the radio waves over the travel path) affect the returned signal. Therefore σ is used in a larger equation, which takes all of the other contributing terms into account, called the *radar equation*.

The bistatic radar equation, which calculates the expected power at the receiver, P_r, when radio waves are scattered off a particular target is given by

$$P_r = \frac{P_t G_t G_r \lambda_0^2 \sigma}{(4\pi)^3 R_t^2 R_r^2 L_t L_r L_s}, \tag{1.14}$$

where P_t is the transmitted power, G_r and G_t are the receiver and trasmitter gains respectively, σ is the radar cross section as in equation 1.13, λ_0 is the radar wavelength, R_r and R_t are the distances from the target to the receiver and transmitter respectively, L_s represents system losses (such as transmission losses) and, L_r and L_t are the propagation losses over the receiver-to-target and transmitter-to-target paths respectively (caused by attenuation due to finite conductivity, etc.).

This is not usually the only source of power at the receiver, though. Signals from other undesirable sources may also be received, which are categorised as *noise* and these provide a *noise floor*. The strength of a desired signal in relation to the noise floor is measured by the

signal to noise ratio, or SNR. By definition, it is the ratio

$$\mathrm{SNR} = \frac{P_{\mathrm{signal}}}{P_{\mathrm{noise}}},$$

which in dB becomes

$$\mathrm{SNR} = 10\log_{10} P_{\mathrm{signal}} - 10\log_{10} P_{\mathrm{noise}},$$

where P_{signal} is the power in the signal and P_{noise} is the average noise level.

§ 1.2 Introduction to Ocean Waves

In this section, an introduction to ocean waves is given. Although the works of Kinsman [54] and Holthuijsen [44] can provide the reader with more in-depth discussions of ocean waves, the key points, necessary for the chapters to follow, are provided. Firstly, the notion of an ocean spectrum is introduced before different ways of measuring and modelling the spectrum are discussed. Important ocean statistics, such a significant waveheight and mean wave direction are also defined in terms of the spectrum.

1.2.1 Waves in The Ocean

The turbulence of the wind produces random pressure fluctuations at the sea surface. These fluctuations cause small waves to appear, known as capillary waves, which surface tension acts on to try and restore the ocean to a flat state. The wind acts further on these capillary waves, causing them to become larger, and once the wavelength exceeds $\sim$1.73cm, they are called gravity waves, where gravity is now the restorative force. Both capillary and gravity waves are labelled as *wind waves* because they are created by the wind, however, they are distinguished by how the Earth tries to restore the ocean to a flat state. An example of wind waves in the ocean is shown in figure 1.9, where (in this particular example) the larger gravity waves are dominant.

The wind continues to act on the gravity waves causing them to become larger, in both length and height, however, there is a limit to their growth. The limit is dependent not only on the wind speed but on the distance the wind blows over (the fetch) and the duration of the wind too. As stated by Kinsman "the wind needs not only strength, but also time and elbowroom, to do its work". Energy is imparted to the waves through the direct wind but frictional drag of the wind and pressure differences in the air also contribute. Energy is lost through the turbulent motion and viscosity of the water and wave-breaking. Once the energy-in is balanced with the energy-out, the waves have reached their limit and the sea is said to be

Figure 1.9: Wind waves in the ocean.

fully developed.

For changes to occur to the ocean after it is fully developed, there must be a change in the energy level of the wind. If the speed of the wind, increases, the waves will continue to grow. If the wind subsides, or the waves leave the area the wind is blowing in, the remaining waves become swell, as shown in figure 1.10, which can travel hundreds of miles.

Figure 1.10: Swell waves in the ocean.

By linear wave theory [17], the dispersion relation of ocean waves in water of finite-depth, is

$$\omega = \sqrt{gk \tanh(kd)}. \tag{1.15}$$

for acceleration due to gravity g, wavenumber k, ocean depth d and angular frequency ω.

From equation 1.15, phase speed, c_p, can be calculated using $c_p = \omega/k$ as

$$c_p = \sqrt{\frac{g}{k}\tanh(kd)}. \tag{1.16}$$

Equation 1.16, alongside $\lambda = k/(2\pi)$, for ocean wavelength λ, shows that the longer the ocean wave, the faster it propagates. Consequently, as swell waves propagate, the longer waves travel faster and the different frequencies become spread out.

Both swell and wind wave systems may be present in the ocean at the same time and by looking at the ocean, one can see that waves of different heights and periods occur. At any given point, the ocean height is due to a superposition of a large number of waves, of varying amplitudes and wavelengths, travelling in different directions. This complexity makes the sea a completely random process and due to the range of different sized waves present in the ocean, a convenient way to describe the ocean surface is with an energy spectrum, denoted by $S(f, \theta)$, for frequency f and direction θ.

1.2.2 Measuring Ocean Spectra

Measuring the ocean spectrum is predominantly done in two ways: (1) in-situ techniques, where a measuring device is deployed into the ocean directly or (2) remote sensing techniques, where a device (such as a HF radar) is situated a distance away from the ocean.

1.2.2.1 In-situ Measurements

In-situ devices, such as a wave buoy, record a time series of the vertical motion of the ocean in one place. Different types of wave buoy measure this differently, however, one option is to use an accelerometer which measures the vertical acceleration of the buoy. The recorded acceleration data is then integrated twice to produce a time series of vertical displacement as shown in figure 1.11.

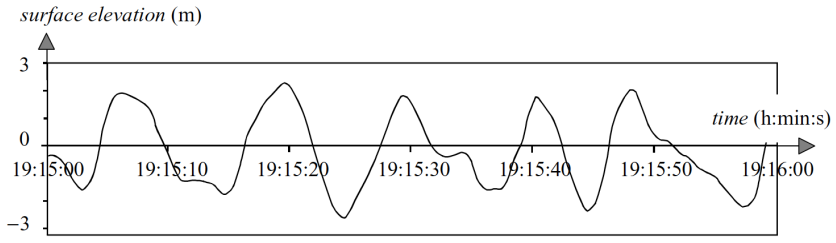

Figure 1.11: An example of a wave-buoy measured time series of the ocean wave height as depicted by Holthuijsen [44].

To obtain directional information, the buoy must record horizontal movement as well as vertical movement. This can be done, for example, by an inclinometer, which measures the tilt of the buoy. The raw buoy data can then be used to estimate the directional spectrum which can be done using a method such as the maximum entropy or maximum likelihood method. The methods have different advantages and disadvantages, as different assumptions are made in order to maximise the functions. More details on these techniques, amongst others, can be found in the works of Kahma *et al.* [37] and Hashimoto [35]. A directional spectrum, obtained from a wave buoy using a MATLAB toolbox [13] is shown in figure 1.12.

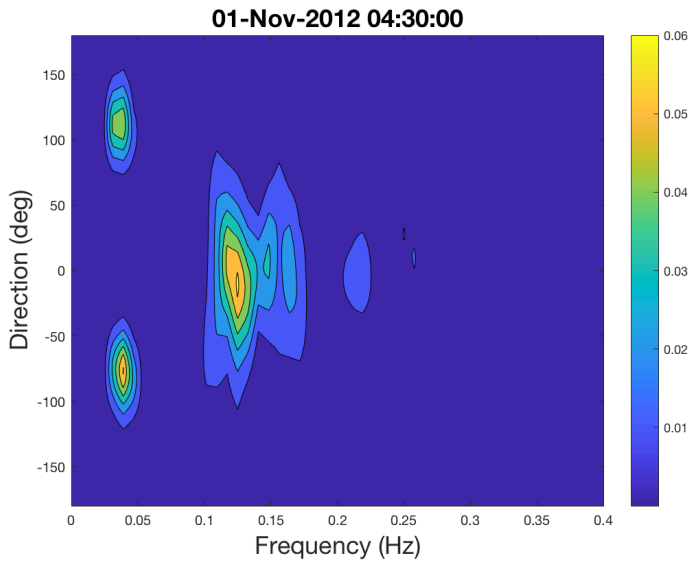

Figure 1.12: An example of a wave buoy directional spectrum, from the Wave Hub dataset described in section 5.2.1. The colour shows the wave energy in m^2/Hz/deg.

To average out the randomness of the ocean, longer time series are desirable. However, the data should only be collected for a time when the ocean is statistically stationary, which is more likely for a shorter period. Therefore, measuring an ocean spectrum becomes a balance of maximising the size of the data sample whilst minimising the effects of the changing ocean conditions. In Kahma *et al.* [37], the typical measuring time is said to be 30 minutes, and in Holthuijsen [44], is said to be 15-30 minutes.

The main advantages of a wave buoy are the accuracy of the derived parameters and its ability to provide continuous measurements. Due to their accuracy, wave buoys are often used to validate remote sensing methods in one location, as is the case in Chapter 5. Compared to a satellite, which may only pass over a given location once a day, a buoy provides the user with a vast, continuous dataset. On the other hand, the fixed location of the buoy means that only data for its exact position is measured and furthermore, if the device becomes damaged, it is

not in a convenient location to repair it.

To combat the disadvantages mentioned for in-situ devices, remote sensing tools are an alternative method of measuring the ocean spectrum and a number of techniques are used.

1.2.2.2 Remote Sensing Measurements

Ground-based radar methods, such as monostatic HF radar, have been showed to measure accurate directional spectra from back-scattered Doppler spectra. HF radar is not limited to measuring in one position, like a wave buoy, and can measure across a larger expanse of the coastal ocean, over an area of the order of 100 km^2. Marine radars, which operate in the X frequency band (8-12 GHz), are another ground-based radar used to measure the directional spectrum, just on a smaller scale (of a few km^2). The marine radar measures the wave pattern of the ocean by exploiting the relationship between the radio waves and the wind-driven ripples on the sea surface. A time series of these 'images' are collected and then the series is analysed to obtain the directional spectrum. With this method, the propagation of individual waves and wave groups can also be measured.

As an alternative to ground-based radar, spaceborne altimeters use microwaves to measure the distance between the measuring device which is attached to a satellite and the sea surface. From these data, measurements of significant waveheight can be made, as described by Cheney *et al.* [83]. If the altimeter is instead attached to an aircraft, the device is called a scanning altimeter and measurements of the directional spectrum can be made.

Synthetic aperture radar, also known as SAR, is an airborne/spaceborne method able to provide continuous measurements of the directional ocean spectrum on a global scale. Operating in one of the X (8-12 GHz), C (4-8 GHz) or L (1-2 GHz) bands, SAR (like the marine radar) measures wave patterns with high resolution and then image processing and wave retrieval methods are used to estimate the directional ocean spectrum.

A more thorough introduction to each of the remote sensing methods mentioned, where further references are cited, is given by Kahma *et al.* [37].

1.2.3 Statistics of Ocean Spectra

A directional ocean spectrum $S(f, \theta)$, can contain too much information for many applications. One usually cares more about statistics, derived from $S(f, \theta)$, which describe the general size and direction of the waves. Firstly, the nondirectional spectrum, $E(f)$ is calcu-

lated from $S(f,\theta)$ by

$$E(f) = \int_0^{2\pi} S(f,\theta)\, d\theta \tag{1.17}$$

and the first Fourier coefficients a_1 and b_1 (see Kuik *et al.* [56]) are

$$a_1 = \int_0^{2\pi} S(f,\theta)\cos\theta\, d\theta \tag{1.18}$$

and

$$b_1 = \int_0^{2\pi} S(f,\theta)\sin\theta\, d\theta. \tag{1.19}$$

From Tucker [94], the historical measure of the height of ocean waves was defined as the average height of the largest 1/3 of the waves. However, this definition has largely been abandoned and the current, universally acknowledged, measure of the significant waveheight, h_s, is defined as

$$h_s = 4\sqrt{\int E(f)\, df}. \tag{1.20}$$

Unlike h_s, the period of the ocean is measured in a number of ways. In this work, peak period, t_p, which is the inverse of the spectral peak frequency, f_p, and the energy period, t_E, which measures approximately where the power is based in frequency, defined by Wyatt [104] as

$$t_E = \frac{\int f^{-1}E(f)\, df}{\int E(f)\, df}, \tag{1.21}$$

are used.

To capture directional information from the spectrum, the peak direction, θ_p, which is the direction of the most energetic waves in the spectrum is defined as

$$\theta_p = \arctan\left(\frac{b_1(f_p)}{a_1(f_p)}\right), \tag{1.22}$$

for $f_p = 1/t_p$, and a_1 and b_1 as in equations 1.18 and 1.19. The mean wave direction, on the other hand, is defined as

$$\theta_m = \arctan\left(\frac{\int b_1(f)\, df}{\int a_1(f)\, df}\right). \tag{1.23}$$

For uni-modal spectra, θ_m and θ_p will be similar. However, for bi-modal spectra, perhaps for a sea including a locally wind driven spectrum alongside a swell spectrum, the two may be far apart and in this case neither parameter will represent the distribution particularly well. In a situation such as this, *partitioning methods* can be used, whereby the different systems which the sea state comprises are separated as shown in figure 1.13. Image processing methods can be used to separate the spectra, as described by Vincent and Soille [96].

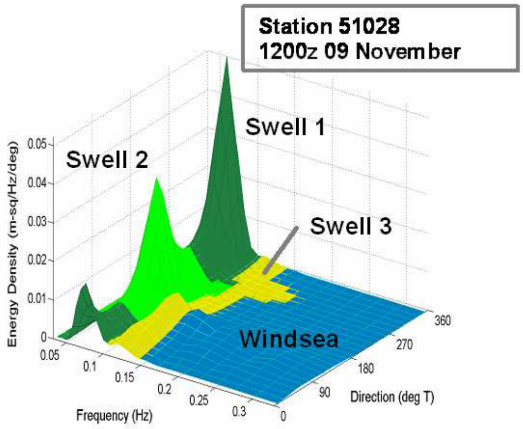

Figure 1.13: A directional ocean spectrum comprising one wind-sea system and three swell systems, where each system has been partitioned as shown by colour and label, by Tolman *et al.* [92]. The partitioning method used here is based on the work of Vincent and Soille [96].

1.2.4 Modelling Directional Ocean Spectra

Sometimes it is not feasible to have a measurement device at all - perhaps due to financial constraints or location issues. In such circumstances, a Wave Model can be used instead, which uses fluid dynamics and numerical techniques to create predictions of the sea state in a desired area. Three notable Wave Models are

- WaveWatch III, henceforth referenced to as 'WW3' [92][91],
- SWAN [12], and
- WAM [55].

All three of these third-generation models consider the physical processes that govern wave development to create hindcasts and forecasts of the ocean spectrum. Initial conditions are input into the model, the governing equations are solved and then wavenumber-direction spectra are output, on a grid of user-defined resolution. Data acquired from various sources,

such as satellite measured wind data, can be used as the input to the model to make accurate predictions, however, if no data are available, earlier model data can be input instead.

Depending on the simulation, the outputs can be full directional spectra or ocean spectrum statistics, such as h_s, t_p and θ_m (single or partitioned), as outlined in section 1.2.3. If only the statistics are returned, ocean spectrum models can be used to simulate an ocean spectrum, which is useful in simulating HF Doppler spectra as shown in Chapters 3-5. Two of the most common models for the non-directional ocean spectrum $E(f)$, the Pierson Moskowitz and JONSWAP spectra, are introduced below.

1.2.4.1 Pierson Moskowitz Spectrum

The Pierson Moskowitz spectrum models how energy is distributed throughout different frequencies in a fully developed sea. It was developed empirically by Pierson and Moskowitz [72][77], using data collected by accelerometers on British weather ships in the North Atlantic. The collected ocean data were processed and averaged by Moskowitz [72] to create a set of power spectra for wind speeds between 20 and 40 knots (see figure 1.14). These spectra were then used to fit an idealised ocean wave spectrum, which Tucker [94] writes as

$$E_{PM}(f) = \frac{\alpha g^2}{(2\pi)^4 f^5} \exp\left(-\frac{5}{4}\left(\frac{f_p}{f}\right)^4\right), \tag{1.24}$$

where f_p is the spectral peak frequency, f is ocean wave frequency in Hz and where $\alpha = 8.1 \times 10^{-3}$ is a dimensionless parameter. Figure 1.15 shows $E_{PM}(f)$ for various wind speeds where the similarities between the real data, in figure 1.14, and the model are evident.

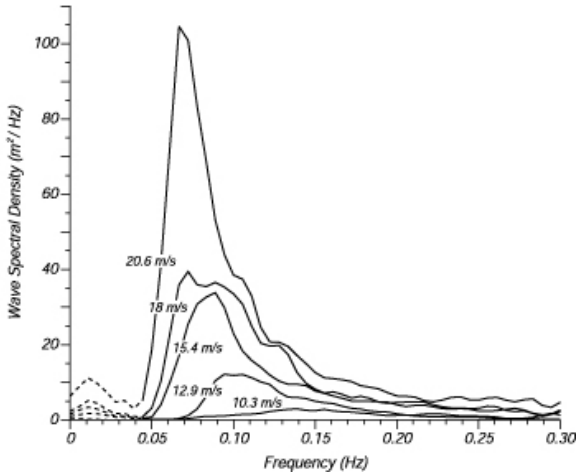

Figure 1.14: The averaged ocean spectra of Moskowitz [72], for different wind speeds.

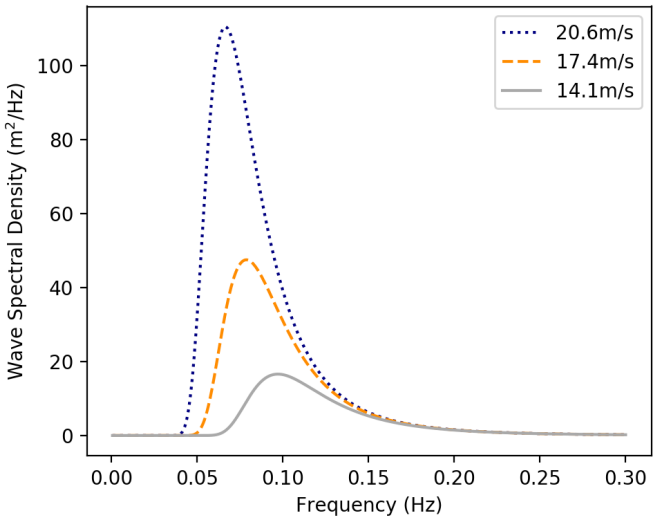

Figure 1.15: Pierson Moskowitz spectra for various wind speeds.

In Chapters 3 and 5, in order to simulate HF radar data, a value of $E(k)$ for wavenumber k is necessary. To transform the Pierson Moskowitz spectrum given in equation 1.24, to be in terms of k, we use the dispersion relation in equation 1.15, alongside the transformation equation

$$E(k) = \left(\frac{df}{dk}\right) E(f), \tag{1.25}$$

to give

$$E(k) = \frac{\alpha_2 \left(\tanh(kd) + kd\,\mathrm{sech}^2(kd)\right)}{2k^3 \tanh^3(kd)} \exp\left(-\frac{20\pi^4}{g^2 t_p^4 k^2 \tanh^2(kd)}\right), \tag{1.26}$$

where

$$\alpha_2 = \frac{5h_s^2\pi^4}{t_p^4 g^2}.$$

1.2.4.2 JONSWAP Spectrum

Another commonly used empirical model is the JONSWAP spectrum of Hasselmann *et al.* [36], which does not assume that the ocean is fully developed. For a partially developed sea, either because of limited fetch (i.e. the length of water over which the wind has blown) or limited duration, there is a greater energy concentration around the peak frequency and this is accounted for, in the JONSWAP model, by a *peak enhancement factor*. The model is given

by Tucker [94] as

$$E_J(f) = \frac{\alpha g^2}{(2\pi)^4 f^5} \exp\left(-\frac{5}{4}\left(\frac{f_p}{f}\right)^4\right) \gamma_j^{r_j},$$

where $\gamma_j = 3.3$ and

$$r_j = \exp\left(\frac{-(f-f_p)^2}{2\sigma^2 f_p^2}\right),$$

in which

$$\sigma = \begin{cases} 0.07 & \text{if } f \leq f_p \\ 0.09 & \text{otherwise.} \end{cases} \tag{1.27}$$

Fetch, L_f, in metres, and wind speed 10 metres above the surface, U_{10}, in m/s, can be incorporated into the model using the relation

$$f_p = \frac{(3.5 g L_f / U_{10}^2 - 0.33) g}{U_{10}}.$$

Figure 1.16 shows how different fetch sizes affect the JONSWAP model and how the model compares to the Pierson Moskowitz model. In figure 1.16 (a), the peak enhancement factor is evident in the modelled JONSWAP spectrum.

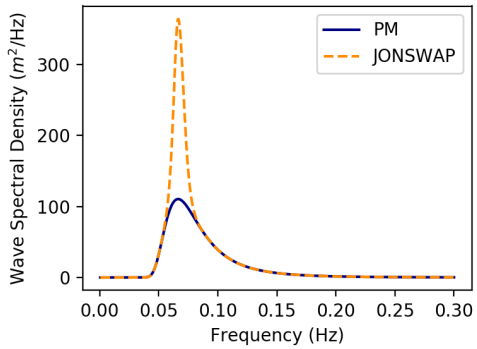

(a) Comparison of the JONSWAP and Pierson Moskowitz models.

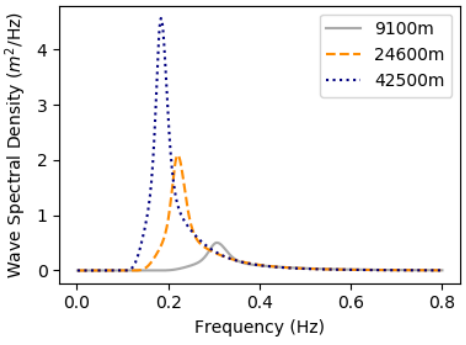

(b) The affect of different fetch sizes on the JONSWAP model.

Figure 1.16: Simulated JONSWAP spectra for a wind speed of 20.6 m/s.

In the following chapters, a Pierson Moskowitz spectrum is used to model the ocean wave spectrum due to difficulties in calculating fetch, in the relevant locations, for the JONSWAP model.

1.2.4.3 The Directional Spectrum

The Pierson Moskowitz and JONSWAP spectra show how the ocean's energy is distributed across a range of frequencies but not across direction. As waves with different frequencies will be propagating in different directions, a directional distribution should be included. The directional ocean spectrum is defined by

$$S(f,\theta) = E(f)G(f,\theta),$$

where $E(f)$ is the omnidirectional ocean spectrum and $G(f,\theta)$ is the normalised directional distribution, such that

$$\int_0^{2\pi} G(f,\theta)\, d\theta = 1.$$

To ensure that $G(f,\theta)$ is normalised, it includes a normalisation factor D, where

$$D = \frac{1}{\int_{-\pi}^{\pi} G(f,\theta)\, d\theta.} \tag{1.28}$$

As with the non-directional spectrum, there are a number of models to choose from. An often-used model for $G(f,\theta)$ is the half cosine squared distribution, of Longuet-Higgins [62], given by

$$G(f,\theta) = D\cos^{2s}\left(\frac{\theta-\theta^*}{2}\right), \tag{1.29}$$

where θ^* is the mean wind direction and s is a spreading function which describes the spread of the distribution. Figure 1.17 depicts the distribution for example values of s.

Another widely used model is the hyperbolic secant distribution of Donelan [20] which includes a small amount of energy in the direction opposite to the mean wind direction. Explicitly,

$$G(f,\theta) = 0.5D\beta\,\mathrm{sech}^2(\beta(\theta-\theta^*)), \tag{1.30}$$

where β denotes the spread of the waves.

1.2.4.4 Modelling Swell

As stated before, the ocean can consist of both wind wave and swell systems. Therefore, in the modelled spectrum, swell must also be included. The superposition of the spectra is

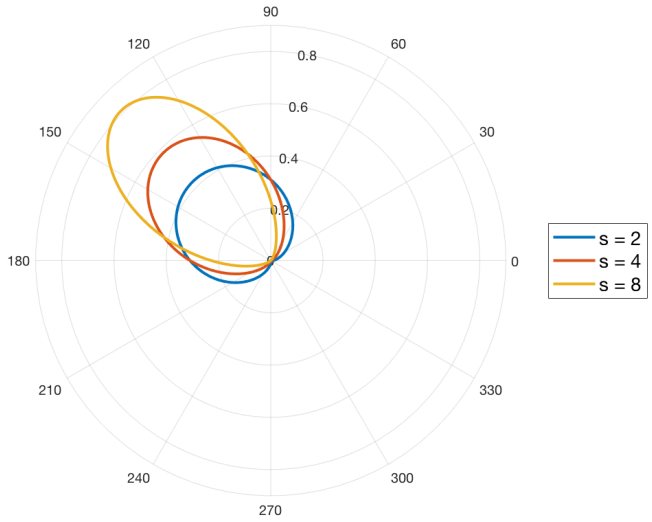

Figure 1.17: Half cosine squared directional distribution, of equation 1.29, with $\theta^* = \frac{3\pi}{4}$ and varying values of s.

written

$$S(f,\theta) = S_{\text{wind}}(f,\theta) + S_{\text{swell}}(f,\theta),$$

where $S_{\text{wind}}(f,\theta)$ defines the wind-sea spectrum and $S_{\text{swell}}(f,\theta)$, the swell spectrum. As before, a number of models can be used to model $S_{\text{swell}}(f,\theta)$, where different models will be more suited to different environments.

When ocean waves leave the area they were generated in, the dispersion relation of waves (equation 1.15) states that the low frequency waves will travel faster. Therefore, after propagating for some time, the ocean system will have lost most of its high frequency components as is shown in figure 1.10. As a result, the spectrum will be more narrow and focussed around the frequency peak. As a JONSWAP model features a more narrow peak for developing seas, this is seemingly a better choice than the broader Pierson Moskowitz model. A general Gaussian distribution - symmetrical about a point with changeable width - could also be a good option. Lucas and Soares [64] compared a Gaussian model for swell with the JONSWAP model, using swell data measured off the coast of Nigeria and the west coast of New Zealand. In this particular case, they found that the JONSWAP model fitted the measured spectra better; an example of a JONSWAP modelled swell spectrum and its combination with a Pierson Moskowitz wind-sea spectrum can be seen in figure 1.18.

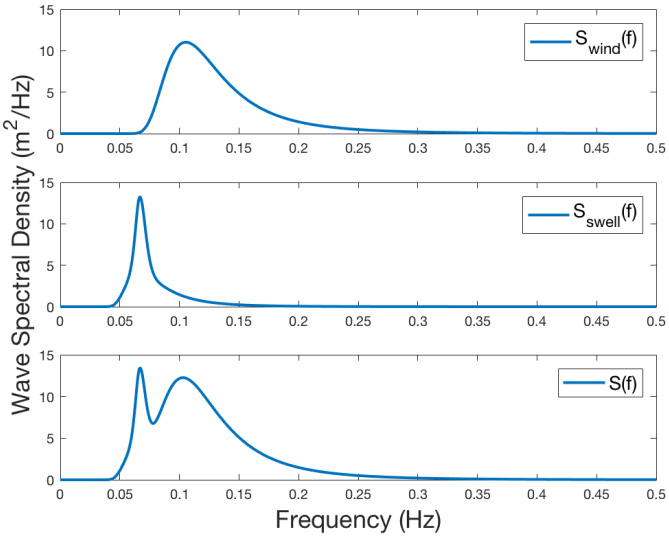

Figure 1.18: The top figure shows a Pierson Moskowitz spectrum for a wind speed of 13 m/s. The middle figure shows a JONSWAP swell spectrum, for a h_s value of 1.4 m and the bottom figure shows the superposition of the wind wave and swell spectra.

§ 1.3 Radar and The Ocean

The relationship between radar and the ocean was first observed during WWII when radar systems had been implemented to track approaching aircraft and ships [10]. During the war, the interest in the returned signal was the identification of a vessel, however, there was other information in the signal too. At the time it was deemed to be noise and was discarded but the majority of the extra information was actually backscatter from the ocean.

The amalgamation of many different-sized waves travelling in different directions in the ocean means that, due to the Doppler effect, an incident wave of a single frequency will return a power spectrum (usually referred to as a Doppler spectrum to reflect the importance of the Doppler effect), consisting of a range of frequencies, when scattered off the ocean surface. An example Doppler spectrum, when HF radio waves are scattered from the ocean, is shown in figure 1.19. HF radio waves are a subset of radio waves with a frequency of between 3 and 30 MHz, or equivalently with wavelengths of between 100 and 10 metres (see table 1.1). Although HF is the most commonly used frequency for this particular radar system, measurements are also possible using radio waves in the MF band [7]. To explain why these bands are the most appropriate, the scattering process must first be analysed.

The first substantial contribution in understanding the relationship between radar and the ocean came in 1955, when Crombie [19] found that when HF radio waves are scattered from

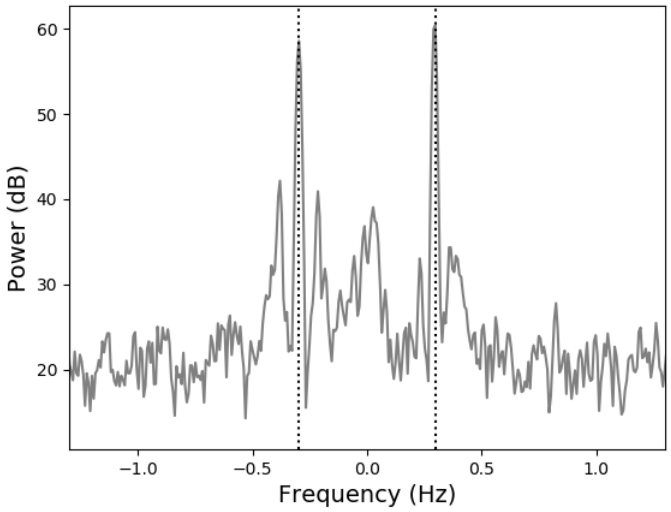

Figure 1.19: An example of a HF radar Doppler spectrum obtained by a monostatic WERA radar operating at 8.512 MHz in Guilderton, Western Australia [38].

the ocean surface, the backscattered signal produces a Doppler spectrum with defining characteristics. When observing a spectrum similar to figure 1.19, Crombie noticed two well-defined peaks (as are highlighted in figure 1.19 by the dotted lines) and recognised that this indicated scattering from two identifiable, distinct targets. He speculated at an explanation for this which he backed up experimentally, but not theoretically.

Crombie said that, due to resonance as shown in figure 1.20, an ocean wave scatterer of wavelength λ would reflect a large signal if λ is half that of the radar wavelength, λ_0. Then, as one of the peaks is positive and the other negative, Crombie speculated that the two identifiable targets were ocean wave trains travelling towards and away from the radar with a wavelength of $\lambda_0/2$. To test his hypothesis, Crombie used the equation for calculating the Doppler shift given in equation 1.2.

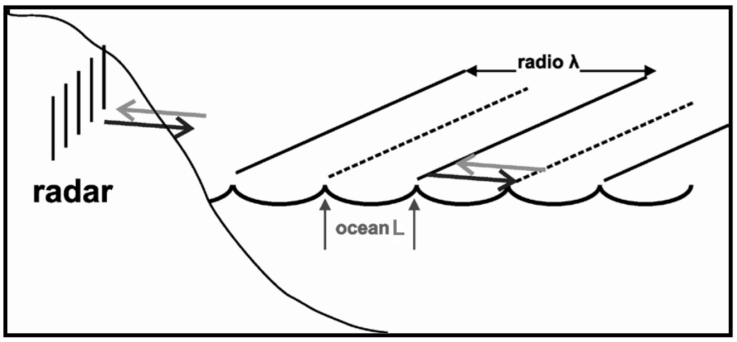

Figure 1.20: How resonance and Bragg scattering are related as depicted by Wyatt [101].

From equation 1.16, the phase speed of a deep water wave (so letting $d \to \infty$ in equation 1.16) is

$$c_p = \sqrt{\frac{\lambda g}{2\pi}}. \tag{1.31}$$

Therefore, substituting $\lambda = \lambda_0/2$ into equation 1.31 and then the resulting expression into equation 1.2 gives the Doppler shift in terms of radar wavelength as

$$\triangle f = \sqrt{\frac{g}{\lambda_0 \pi}}. \tag{1.32}$$

Crombie substituted the wavelength of the carrier frequency into equation 1.32 and found that it was approximately equal to where the peaks were in the spectrum. The position of the dashed lines in figure 1.19 were obtained in the same manner and do, indeed, line up with the prominent peaks of the spectrum.

Then, in 1972, Barrick [5][7] theoretically showed that Crombie's prediction was correct, using the perturbation analysis of the scattering process first presented by Rice [78]. Barrick presented a monostatic radar cross section of the ocean, σ, to second order, which is in terms of the ocean spectrum $S(\mathbf{k})$ and radar wavenumber k_0. The expression for σ can be split into the first and second order terms, $\sigma^{(1)}(\omega)$ and $\sigma^{(2)}(\omega)$ respectively. Explicitly,

$$\sigma^{(1)}(\omega) = 2^6 \pi k_0^4 \sum_{m=\pm 1} S(m\mathbf{k_B})\delta(\omega - m\omega_B), \tag{1.33}$$

and

$$\sigma^{(2)}(\omega) = 2^6 \pi k_0^4 \sum_{m,m'=\pm 1} \iint_{-\infty}^{\infty} |\Gamma_T|^2 S(m\mathbf{k_1}) S(m'\mathbf{k_2}) \delta(\omega - m\omega_1 - m'\omega_2)\, dp\, dq, \tag{1.34}$$

where the terms will be derived and explained thoroughly in Chapters 2 and 3. To summarise, the strong signal produced by $\sigma^{(1)}(\omega)$ is due, as Crombie said, to ocean waves with wavelength $\lambda/2$ travelling towards and away from the radar. These waves will henceforth be referred to as the Bragg waves and the signal that they produce is shown by the dashed lines in figure 1.19. The signal shown around the highlighted peaks is caused by $\sigma^{(2)}(\omega)$. Defining $\mathbf{k_B}$ as the wavevector of the Bragg wave travelling towards the radar, the signal produced by $\sigma^{(2)}(\omega)$ is due to pairs of ocean waves with wavenumbers $\mathbf{k_1}$ and $\mathbf{k_2}$ such that

$$\mathbf{k_1} + \mathbf{k_2} = \mathbf{k_B}.$$

Equations 1.33 and 1.34 represent the *forward problem* of remotely sensing the ocean. That is, given an ocean spectrum $S(\mathbf{k})$, they model the expected radar Dopper spectrum $\sigma(\omega)$. Solving the *inverse problem*, i.e. obtaining ocean information from $\sigma(\omega)$, has enabled researchers to measure ocean currents, winds and waves from HF radar Doppler spectra.

1.3.1 HF Radar Systems

The methods of inverting the measured Doppler spectrum for current, wind and wave measurements are now reliable enough such that there are hundreds of coastal radar HF systems worldwide, providing data. There are a number of different brands of radar for this purpose, both compact and phased-array systems. The Seasonde [2], developed by CODAR, is the most notable compact radar and they state that they have 'produced approximately 80% of all HF radars ever built worldwide, with a total operating time of over 2,000,000 hours'. They mostly provide current measurements as shown in the works of Lipa *et al.* [75] and Hodgins [42] due to the broad beam, however, directional wave information [60][25] is also possible if one assumes that the ocean spectrum is stationary and homogenous for each radar range. The Wellen and Pisces [74] radar systems are established phased array radar systems and as Wellen radar data is used in this work, a more detailed description follows.

1.3.1.1 WERA Radar System

The Wellen Radar, henceforth referred to as WERA, was created by Gurgel *et al.* [31][3] at the Univerity of Hamburg in the late 1990s. The WERA system is one of the most common HF phased array radars around the world, especially for HF radars which measure ocean wave spectra. The transmitter emits FMCW chirps and a receiver array (as shown in figure 1.21), of up to 16 antennas placed along coastal regions, receives the scattered signals which are beamformed, as in section 1.1.6, to provide good azimuthal resolution. For a particular radar site, the radar frequency and bandwidth are chosen such that they are optimal for the local conditions.

Identifying the optimal frequency and bandwidth depends on the ocean waves that exist in the coverage area and the frequencies of any other interfering radio waves. From section 1.1.4, the longer the radio wavelength the further the maximum range will be. However, for longer radio wavelengths, the Bragg ocean waves will also be longer and in certain areas - perhaps due to limited fetch or finite-depth - they may not appear frequently, if at all. Consequently, the returned Doppler spectrum will have a low SNR and thus, wave information in the signal will be hard to retrieve. Therefore an appropriate frequency must be chosen such that adequate

Figure 1.21: Example of a WERA linear receive array on the coast, consisting of 16 antennas [45].

SNR levels are achieved. Long-term observations of the radio band coverage using a spectrum analyser are carried out before a frequency is selected; interference from other signals at the same frequency would also have a negative impact on the SNR.

Gurgel [45] presented the working ranges for surface current measurements from WERA radars, for particular carrier frequencies and salinity levels. The full list is shown in figure 1.22, however it should be highlighted that wave measurements, due to the requirement of the second order signal (which is less strong), do not achieve the same ranges. If the information in the table is extrapolated to higher frequencies, the working range will soon become negligible. At the other end of the spectrum, toward the MF band, the Bragg wave wavelengths become uncommonly large and consequently, the signal will have a low SNR. In both cases, the data becomes less useful and this is why HF radar is used for ocean sensing.

The capability of HF radar to provide accurate current, wind and wave measurements has led to it being used in a number of important applications.

1.3.2 Applications

Remotely sensing the ocean has an impact on numerous coastal engineering topics, including testing of and assimilation in operational wave models, sea vessel navigation, land/beach erosion, designing offshore structures and, in supporting marine activities. Additionally, collecting ocean data over a long period of time can be useful in climate change studies; the same data can also be used to assess the potential of a coastal region to become a wave/wind farm as shown by Wyatt [105].

f_0 [MHz]	P_{Bragg} [s]	W_{Bragg} [m]	R_8 [km]	R_{16} [km]	R_{35} [km]	R_{opt} [km]	R_{min} [km]	R_{resol} [km]
8.00	3.47	18.75	107.0	158.5	218.0	300.0	200.0	5.0
12.00	2.83	12.50	65.0	100.0	143.0	180.0	115.0	3.0
16.00	2.45	9.38	45.5	70.5	102.5	130.0	75.0	1.5
20.00	2.19	7.50	34.0	53.0	78.0	100.0	60.0	1.0
25.00	1.96	6.00	25.5	40.0	59.5	75.0	45.0	0.5
30.00	1.79	5.00	20.0	32.0	47.0	50.0	30.0	0.25

f_0 Radar frequency
P_{Bragg} Period of Bragg scattering ocean wave
W_{Bragg} Length of Bragg scattering ocean wave
R_8 Working range at 8 PSU salinity (propagation model)
R_{16} Working range at 16 PSU salinity(propagation model)
R_{35} Working range at 35 PSU salinity(propagation model)
R_{opt} Working range at 35 PSU salinity, optimum sea state (literature)
R_{min} Working range at 35 PSU salinity, high sea sea state (literature)
R_{resol} Highest range resolution possible

Working ranges are given for surface current measurements; processing of ocean wave parameters requires an increased Signal/Noise ratio which reduces the working range by about 30%.

Figure 1.22: Table produced by Gurgel [45] showing the ranges possible for obtaining surface current measurements from WERA HF radar Doppler spectra.

A notable group of radar systems, collecting and providing ocean data is part of the Integrated Ocean Observing System (IOOS), whose website shows real-time HF radar current data along the American coast. Likewise, in Australia, the Integrated Marine Observing System (IMOS) provides real-time coastal surface currents and wave parameters measured by HF radar. The measurements are provided by the Australian Coastal Ocean Radar Network (ACORN) facility [38] which consists of 6 pairs of HF radars in four regions; the data for each radar can be downloaded from the IMOS website [48] and is available from 2007, for some radars.

Coastal monitoring systems such as the IMOS and IOOS networks lend themselves to an extremely important topic: the early warning of a tsunami. The use of HF Radar current measurements in predicting a tsunami approaching has been investigated by Heron [39] and Dzvonkovskaya [22], where it was shown to be a helpful, complementary tool. It is now implemented in the 'National Multi Hazard Warning Center' in Oman along with data from other sensor systems including seismic stations and tide gauges. Two 9 MHz and two 13 MHz WERA ocean radar systems have been situated on the coast to provide tsunami warnings and also to predict the size of the approaching waves.

Another important application of HF radar current data is in predicting the area an off-shore oil spill will cover. The positive effect that HF radar current measurements have on the mapping of a trajectory of an oil spill has been shown by Abascal [1]. In this work, the trajectory of a buoy, along the Galician coast, was simulated using numerical wind data, with and without the HF current data, to evaluate the effectiveness of HF radar in this scenario.

When the simulations for both cases were run, the resulting area to be tracked when the HF current data was included, was reduced by 62%. When a crisis such as an oil spill occurs, the reaction time and accuracy of the search location is imperative. The decrease in the search area by 62% in this experiment means that more resources can be devoted to the appropriate area which will save time, money and, potentially, lives. The theory of forecasting the buoy trajectory can be applied to other aspects such as human search and rescue, as shown by Harlan *et al.* [33].

Final Remark

With important applications such as those mentioned in the preceding section, the methods for obtaining ocean parameters from HF radar data must be accurate and reliable. In the next chapter, the bistatic radar cross section of the ocean surface will be derived which will then be used in the chapters that follow, to formulate methods to infer ocean parameters from bistatic HF radar data.

Chapter 2

Derivation of the Bistatic Radar Cross Section of the Ocean Surface

§ 2.1 Introduction

In this chapter, the bistatic radar cross section of the ocean surface, σ, is derived. From equation 1.13, the radar cross section of a target is an expression in terms of the scattered electric field, E_s, and thus, in order to derive σ, we must first derive E_s.

The scattered field, E_s, has dependence on both the incident radio waves and the surface properties. The ocean is a good conductor and hence, to maximise the range that radio waves can reach, the incident waves defined in the problem will propagate as vertically polarised ground waves (as will the resulting scattered waves). Furthermore, as the ocean varies in both time and space, by assuming that these variations are periodic and the surface is of infinite extent, the surface, $f(x, y, t)$, can be defined as a Fourier series expansion. So, letting the spatial period (in both the x and y directions) be L and the temporal period be T we can then define

$$z = f(x, y, t) = \sum_{mnl=-\infty}^{\infty} P(m, n, l) \mathrm{e}^{ia(mx+ny)-iwlt}, \tag{2.1}$$

for wavenumber $a = 2\pi/L$, angular frequency $w = 2\pi/T$ and Fourier coefficients $P(m, n, l)$ which are dependent on the integers m, n and l. In calculating the scattered field produced when the incident radio waves interact with surface $f(x, y, t)$, we follow Rice [78], like Barrick [5] and Johnstone [50]. A full derivation is given in section 2.2 for completeness, as the referenced works derive the scattered field for horizontally polarised incident waves, not vertical. Supplementary to Rice's work, and similarly to Barrick and Johnstone, time

dependence has been included in the scattering surface so that the results are applicable to the (time-varying) ocean surface.

Both the scattering surface and the incident radio waves are assumed to be of infinite extent in section 2.2. However, in practice, a radar will cover only a finite patch of this overall surface and therefore the infinitely scattered fields must be related to finitely scattered fields; this will be carried out in section 2.3. Once the finitely scattered electric field is derived, the bistatic radar cross section is calculated in section 2.4. This follows the methodology of Johnstone [50] but some discrepancies between the works of Johnstone and Barrick [5] have been discovered and more detail is included for clarity. In sections 2.2 to 2.4, the surface is assumed to be perfectly conducting to simplify the necessary boundary condition, however, as the ocean surface is not a perfect conductor, this will be addressed in section 2.5.

§ 2.2 Derivation of the Scattered Electric Field

The scattered field created when the incident waves scatter from $f(x, y, t)$, in equation 2.1, consists of two components; the specular and nonspecular fields. The specular field occurs when the incident plane wave, travelling in the positive x direction at an angle θ measured from the z axis, impinges on a perfectly smooth plane (see figure 2.1). Therefore, the incident electric field, with wavenumber k_0, angular frequency ω_0 and magnitude E_0 can be defined as

$$\begin{aligned} E_x^{(i)} &= E_0 \cos\theta \mathrm{e}^{ik_0(x\sin\theta - z\cos\theta)}\mathrm{e}^{-i\omega_0 t} \\ E_y^{(i)} &= 0 \\ E_z^{(i)} &= E_0 \sin\theta \mathrm{e}^{ik_0(x\sin\theta - z\cos\theta)}\mathrm{e}^{-i\omega_0 t} \end{aligned} \tag{2.2}$$

and the specular scattered electric field as

$$\begin{aligned} E_x^{(s)} &= -E_0 \cos\theta \mathrm{e}^{ik_0(x\sin\theta + z\cos\theta)}\mathrm{e}^{-i\omega_0 t} \\ E_y^{(s)} &= 0 \\ E_z^{(s)} &= E_0 \sin\theta \mathrm{e}^{ik_0(x\sin\theta + z\cos\theta)}\mathrm{e}^{-i\omega_0 t}. \end{aligned} \tag{2.3}$$

Summing the incident and reflected fields (from equations 2.2 and 2.3) gives the total specular field, with components

$$\begin{aligned} E_x &= 0 \\ E_y &= 0 \\ E_z &= 2\mathrm{e}^{ik_0 x}\mathrm{e}^{-i\omega_0 t}, \end{aligned}$$

where we have taken $E_0 = 1$, for consistency with the existing literature[1], and set $\theta = 90°$, as we are interested in ground wave propagation. The benefit of hindsight has been used here, as setting $\theta = 90°$ at this point does not affect the final result but simplifies the calculations to follow.

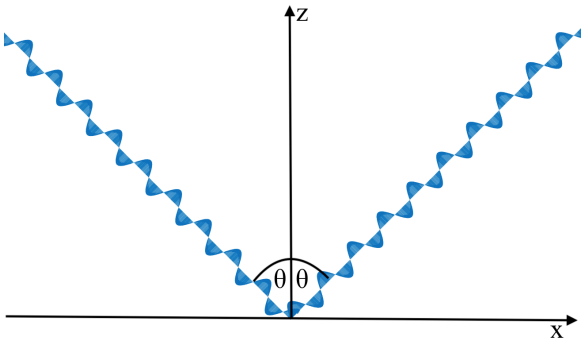

Figure 2.1: Specular scatter, of vertically polarised radio waves at incidence angle θ. The electric field intensity in the relevant direction is shown by the blue wave.

Radio waves scattered by a rough surface make up the nonspecular fields. As the surface defined in equation 2.1 is periodic, these scattered fields are also periodic in x and y with period L and periodic in time with period T. Therefore, like the surface, the non specular scattered fields can be defined by a three dimensional Fourier series expansion. Additionally, to ensure the periodicity of the incident field, let

$$k_0 = \nu a \tag{2.4}$$

for some integer ν and surface wavenumber, $a = 2\pi/L$. Therefore, the components of the total electric field strength, $\mathbf{E} = (E_x, E_y, E_z)$, above the surface (where the specular field has been included) are defined as

$$\begin{aligned} E_x &= \sum_{mnl} A_{mnl} E(m,n,z,l) \mathrm{e}^{-i\omega_0 t} \\ E_y &= \sum_{mnl} B_{mnl} E(m,n,z,l) \mathrm{e}^{-i\omega_0 t} \\ E_z &= 2\mathrm{e}^{ia\nu x} \mathrm{e}^{-i\omega_0 t} + \sum_{mnl} C_{mnl} E(m,n,z,l) \mathrm{e}^{-i\omega_0 t}, \end{aligned} \tag{2.5}$$

where A_{mnl}, B_{mnl} and C_{mnl} are Fourier coefficients to be found for integers m, n and l

[1]The value of E_0 does not have an impact on the resulting expression, as the radar cross section equation used (see equation 1.13) includes a $1/E_0$ term and, therefore, the two are cancelled.

and,

$$E(m,n,z,l) = \mathrm{e}^{i(a(mx+ny)+b(m,n)z)}\mathrm{e}^{-iwlt} \tag{2.6}$$

where $w = 2\pi/T$. The value of $b(m,n)$ is found by ensuring that $\mathbf{E}$ satisfies the wave equation,

$$\nabla^2\mathbf{E} - \frac{1}{c}\frac{\partial^2\mathbf{E}}{\partial t^2} = 0.$$

Differentiating the components of $\mathbf{E}$ in equation 2.5 with respect to t gives

$$\begin{aligned}
\frac{\partial^2 E_x}{\partial t^2} &= -(\omega_0 + wl)^2 E_x \\
\frac{\partial^2 E_y}{\partial t^2} &= -(\omega_0 + wl)^2 E_y \\
\frac{\partial^2 E_z}{\partial t^2} &= -2\omega_0^2 \mathrm{e}^{ia\nu x}\mathrm{e}^{-i\omega_0 t} - (\omega_0 + wl)^2 \sum_{mnl} C_{mnl} E(m,n,z,l)\mathrm{e}^{-i\omega_0 t}.
\end{aligned} \tag{2.7}$$

By assuming the surface is slowly varying, wl will be much smaller than ω_0 (which will be at least to the order of 10^6 at HF), and so we can take $\omega_0 + wl \approx \omega_0$ in the amplitude terms of equation 2.7 with little impact. Thus,

$$\nabla^2\mathbf{E} + k_0^2\mathbf{E} = 0, \tag{2.8}$$

which upon substituting $\mathbf{E}$ in, from equation 2.5, leads to

$$b(m,n) = \begin{cases} (k_0^2 - a^2m^2 - a^2n^2)^{1/2} & \text{if } m^2+n^2 < k_0^2/a^2 \\ i(a^2m^2 + a^2n^2 - k_0^2)^{1/2} & \text{if } m^2+n^2 > k_0^2/a^2. \end{cases} \tag{2.9}$$

In the solutions for $b(m,n)$, the positive root for the imaginary solution is chosen to ensure the exponential decays in $\mathbf{E}$, for increasing z.

To determine the Fourier coefficients A_{mnl}, B_{mnl} and C_{mnl} in equation 2.5, Maxwell's equations and properties of the scattering surface are used. Due to the complexity of the problem and knowing that $k_0 f$, f_x and f_y are of the same order of smallness, the solution is perturbed around the flat surface $z = f = 0$ and terms of up to second order are retained (where terms such as $k_0 f$, f_x and f_y are $O(f)$ and, $k_0^2 f^2$ and f_x^2 are $O(f^2)$).

Firstly, from Maxwell's equations for a source free volume, $\nabla \cdot \mathbf{E} = 0$. So, with $\mathbf{E}$ as in

equation 2.5,

$$\nabla \cdot \mathbf{E} = amA_{mnl} + anB_{mnl} + b(m,n)C_{mnl} = 0. \tag{2.10}$$

Secondly, the tangential electric field boundary condition for a perfectly conducting surface is employed. In a perfect conductor, the electrons are free to move around and thus will cancel out any potential tangential electric field which may occur along the surface. As the tangential electric field at any point on the surface is found by deducting the electric field normal to the surface from the total electric field,

$$\mathbf{E} - \hat{\mathbf{n}}(\mathbf{E} \cdot \hat{\mathbf{n}}) = 0, \tag{2.11}$$

where $\hat{\mathbf{n}}$ is the unit vector normal to the surface. As the surface is defined as $z = f(x,y,t)$, let

$$F(x,y,z,t) = z - f(x,y,t) = 0$$

and therefore, as the unit normal of the surface, $\hat{\mathbf{n}}$, is given by

$$\hat{\mathbf{n}} = \frac{\nabla F}{\mid \nabla F \mid} = \frac{(-f_x, -f_y, 1)}{\sqrt{f_x^2 + f_y^2 + 1}},$$

$$\begin{aligned} n_x &= -f_x(1 + f_x^2 + f_y^2)^{-1/2} = -f_x n_z, \\ n_y &= -f_y(1 + f_x^2 + f_y^2)^{-1/2} = -f_y n_z, \\ n_z &= (1 + f_x^2 + f_y^2)^{-1/2}. \end{aligned}$$

Since n_z expands to $1 + O(f^2)$,

$$\begin{aligned} n_x &= -f_x + O(f^3) \\ n_y &= -f_y + O(f^3) \end{aligned} \tag{2.12}$$

and consequently, to second order, the tangential boundary condition components, of equation 2.11, become

$$\begin{aligned} E_x + f_x E_z &= 0 \\ E_y + f_y E_z &= 0, \end{aligned} \tag{2.13}$$

noting that the z component becomes trivially zero when these two equations are satisfied.

The individual terms in the total electric field components given in equation 2.5 are now also

expanded to second order around the flat surface, $f = 0$. Namely,

$$\begin{aligned} E(m,n,f,l) &= [1 + ib(m,n)f + \cdots]E(m,n,0,l) \\ J_{mnl} &= J^{(1)}_{mnl} + J^{(2)}_{mnl} + \cdots , \end{aligned} \tag{2.14}$$

where the bracketed superscript of a Fourier coefficient, here J_{mnl}, denotes its order.

Therefore, the total electric field components in equation 2.5 become

$$E_x = \sum_{mnl} \left(A^{(1)}_{mnl} + A^{(2)}_{mnl} \right) [1 + ib(m,n)f]E(m,n,0,l)\mathrm{e}^{-i\omega_0 t} \tag{2.15}$$

$$E_y = \sum_{mnl} \left(B^{(1)}_{mnl} + B^{(2)}_{mnl} \right) [1 + ib(m,n)f]E(m,n,0,l)\mathrm{e}^{-i\omega_0 t} \tag{2.16}$$

$$E_z = 2\mathrm{e}^{ia\nu x}\mathrm{e}^{-i\omega_0 t} + \sum_{mnl} \left(C^{(1)}_{mnl} + C^{(2)}_{mnl} \right) [1 + ib(m,n)f]E(m,n,0,l)\mathrm{e}^{-i\omega_0 t} \tag{2.17}$$

and equations 2.15-2.17 are used in the two boundary conditions, in equation 2.13, to give

$$2f_x\mathrm{e}^{ia\nu x} + \sum_{mnl} \left(A^{(1)}_{mnl} + A^{(2)}_{mnl} + f_x C^{(1)}_{mnl} \right) [1 + ib(m,n)f]E(m,n,0,l) = 0 \tag{2.18}$$

and

$$2f_y\mathrm{e}^{ia\nu x} + \sum_{mnl} \left(B^{(1)}_{mnl} + B^{(2)}_{mnl} + f_y C^{(1)}_{mnl} \right) [1 + ib(m,n)f]E(m,n,0,l) = 0. \tag{2.19}$$

2.2.1 First Order Terms

First order terms, in both equations 2.18 and 2.19, are equated to determine $A^{(1)}_{mnl}$, $B^{(1)}_{mnl}$ and $C^{(1)}_{mnl}$. From equation 2.18,

$$2f_x\mathrm{e}^{ia\nu x} + \sum_{mnl} A^{(1)}_{mnl} E(m,n,0,l) = 0 \tag{2.20}$$

and equation 2.19 gives

$$2f_y\mathrm{e}^{ia\nu x} + \sum_{mnl} B^{(1)}_{mnl} E(m,n,0,l) = 0. \tag{2.21}$$

From equation 2.1,

$$f_x = \sum_{m'n'l'} iam' P(m',n',l')\mathrm{e}^{ia(m'x+n'y)-iwl't}$$

$$= \sum_{m'n'l'} iam' P(m', n', l') E(m', n', 0, l')$$

and multiplying both sides by $\mathrm{e}^{ia\nu x}$ gives

$$\begin{aligned} f_x \mathrm{e}^{ia\nu x} &= \sum_{m'n'l'} iam' P(m', n', l') E(m' + \nu, n', 0, l') \\ &= \sum_{mnl} ia(m - \nu) P(m - \nu, n, l) E(m, n, 0, l), \end{aligned}$$

by setting $m' + \nu = m$, $n' = n$ and $l' = l$. As $a\nu = k_0$,

$$f_x \mathrm{e}^{ik_0 x} = \sum_{mnl} ia(m - \nu) P(m - \nu, n, l) E(m, n, 0, l) \tag{2.22}$$

and similarly,

$$f \mathrm{e}^{ik_0 x} = \sum_{mnl} P(m - \nu, n, l) E(m, n, 0, l) \tag{2.23}$$

and

$$f_y \mathrm{e}^{ik_0 x} = \sum_{mnl} ianP(m - \nu, n, l) E(m, n, 0, l). \tag{2.24}$$

By use of equations 2.22-2.24, equation 2.20 becomes

$$A^{(1)}_{mnl} = (2ik_0 - 2iam) P(m - \nu, v, l) \tag{2.25}$$

and equation 2.21 becomes

$$B^{(1)}_{mnl} = -2ianP(m - \nu, v, l). \tag{2.26}$$

The values for $A^{(1)}_{mnl}$ and $B^{(1)}_{mnl}$, from equations 2.25 and 2.26, are now substituted into equation 2.10 to find $C^{(1)}_{mnl}$, i.e.

$$C^{(1)}_{mnl} = -2i \frac{(a(m - \nu)k_0 + b^2(m, n)) P(m - \nu, n, l)}{b(m, n)} \tag{2.27}$$

where the definition of $b(m, n)$ from equation 2.9 has been used to give a more convenient form.

2.2.2 Second Order Terms

The two expressions for the second order terms in equations 2.18 and 2.19 are, respectively,

$$\sum_{mnl}(A^{(2)}_{mnl} + iA^{(1)}_{mnl}b(m,n)f + C^{(1)}_{mnl}f_x)E(m,n,0,l) = 0 \tag{2.28}$$

and

$$\sum_{mnl}(B^{(2)}_{mnl} + iB^{(1)}_{mnl}b(m,n)f + C^{(1)}_{mnl}f_y)E(m,n,0,l) = 0. \tag{2.29}$$

These both include terms of the form $J^{(1)}_{mnl}f_iE(m,n,0,l)$ and, for this, Rice [78] derives three relations in the time invariant case which can be adapted to the time varying case. Namely,

$$\sum_{mnl} f_xJ_{mnl}E(m,n,0,l) = \sum_{mnlqrs} ia(m-q)J_{qrs}P(m-q,n-r,l-s)E(m,n,0,l), \tag{2.30}$$

$$\sum_{mnl} fJ_{mnl}E(m,n,0,l) = \sum_{mnlqrs} J_{qrs}P(m-q,n-r,l-s)E(m,n,0,l) \tag{2.31}$$

and

$$\sum_{mnl} f_yJ_{mnl}E(m,n,0,l) = \sum_{mnlqrs} ia(n-r)J_{qrs}P(m-q,n-r,l-s)E(m,n,0,l). \tag{2.32}$$

By using equations 2.30-2.32, equation 2.28 becomes

$$\begin{aligned} A^{(2)}_{mnl} &= -i\sum_{qrs}\left(A^{(1)}_{qrs}b(q,r) + a(m-q)C^{(1)}_{qrs}\right)P(m-q,n-r,l-s) \\ &= 2\sum_{qrs}(a^2(m-q)(\nu-q)k_0 + (k_0-am)b^2(q,r))Q(m,n,l,q,r,s) \end{aligned} \tag{2.33}$$

and equation 2.29 becomes

$$\begin{aligned} B^{(2)}_{mnl} &= -i\sum_{qrs}\left(B^{(1)}_{qrs}b(q,r) + a(n-r)C^{(1)}_{qrs}\right)P(m-q,n-r,l-s) \\ &= 2\sum_{qrs}\left(a^2(n-r)(\nu-q)k_0 - anb^2(q,r)\right)Q(m,n,l,q,r,s), \end{aligned} \tag{2.34}$$

where

$$Q(m,n,l,q,r,s) = \frac{P(q-\nu,r,s)P(m-q,n-r,l-s)}{b(q,r)}. \tag{2.35}$$

The value of $C^{(2)}_{mnl}$ is now calculated using equation 2.10 with equations 2.33 and 2.34 to give

$$\begin{aligned} C^{(2)}_{qrs} = \frac{2}{b(m,n)} \sum_{qrs} \big(& a^3(q-\nu)(m^2+n^2-qm-rn)k_0 \\ & + a(a(m^2+n^2)-mk_0)b^2(q,r)\big)\, Q(m,n,l,q,r,s). \end{aligned} \tag{2.36}$$

Substituting the first and second order Fourier coefficients (equations 2.25, 2.26, 2.27, 2.33, 2.34 and 2.36) into the total electric field components of equation 2.5 completes the derivation of the total scattered field for vertically polarised waves. The components are

$$\begin{aligned} E_x =& 2\sum_{mnl} E(m,n,z,l)\mathrm{e}^{-i\omega_0 t} \Bigg[i(k_0 - am)P(m-\nu,n,l) \\ & + \sum_{qrs} \left\{ a^2(m-q)(\nu-q)k_0 + (k_0-am)b^2(q,r) \right\} \\ & Q(m,n,l,q,r,s) \Bigg], \end{aligned} \tag{2.37}$$

$$\begin{aligned} E_y =& 2\sum_{mnl} E(m,n,z,l)\mathrm{e}^{-i\omega_0 t} \Bigg[-ianP(m-\nu,n,l) \\ & + \sum_{qrs} \left\{ a^2(n-r)(\nu-q)k_0 - anb^2(q,r) \right\} Q(m,n,l,q,r,s) \Bigg] \end{aligned} \tag{2.38}$$

$$\begin{aligned} E_z =& 2\mathrm{e}^{ik_0 x}\mathrm{e}^{-i\omega_0 t} \\ & + 2\sum_{mnl} \frac{E(m,n,z,l)}{b(m,n)} \mathrm{e}^{-i\omega_0 t} \Bigg[\big(-i(a(m-\nu)k_0 + b^2(m,n)\big) \\ & P(m-\nu,n,l) + \sum_{qrs} \big\{ (a^3(q-\nu)(m^2+n^2-qm-rn)k_0) \\ & + \; a(a(m^2+n^2)-mk_0)b^2(q,r) \big\} Q(m,n,l,q,r,s) \Bigg]. \end{aligned} \tag{2.39}$$

§ 2.3 Transformation of the Field to Account for the Scattering Patch Size

2.3.1 Derivation of the Transformation Equation

The electric field in equations 2.37, 2.38 and 2.39 correspond to the scattering of infinite plane waves from a surface of infinite extent. To transform the fields to finitely scattered fields, the equation given by Johnstone [50] (therein credited to Stratton [86]) is used. The derivation of the equation can be found in Johnstone's work and further details are given by Stratton. To summarise, for some volume, V, enclosed by a surface S on which the electric field $\mathbf{E}$

is known, then, by a combination of the divergence theorem, Stoke's theorem and Green's second identity, we can calculate the electric field at any point within V.

This principle can then be applied to a volume, approximated by a hemisphere like that shown in figure 2.2, whose surface consists of two parts: an infinite S, where $\mathbf{E}$ is zero, and a finite portion of this, S_1 where $\mathbf{E}$ is the infinitely scattered field from equations 2.37 to 2.39. Then, whilst making sure the discontinuity on the surface is accounted for, we can again show that we can find the electric field at any point within V using the value of $\mathbf{E}$ on S_1. Explicitly, the finitely scattered electric field, at a point (x', y', z'), can be expressed as

$$\begin{aligned}\mathbf{E}(x', y', z') =& \frac{\mathrm{e}^{ik_0 R}}{4\pi R} \int_{S_1} \Bigg\{ \left[\left(\frac{\partial E_x}{\partial z} - \frac{\partial E_z}{\partial x} \right) \hat{\mathbf{a}}_x + \left(\frac{\partial E_y}{\partial z} - \frac{\partial E_z}{\partial y} \right) \hat{\mathbf{a}}_y \right]_{z=0} \\ &+ ik_0 \left[E_x \cos\theta \hat{\mathbf{a}}_x + E_y \cos\theta \hat{\mathbf{a}}_y - (E_x \sin\theta\cos\varphi + E_y \sin\theta \sin\varphi) \hat{\mathbf{a}}_z \right]_{z=0} \\ &+ \left[\left(\frac{\partial E_z}{\partial x} - \frac{\partial E_x}{\partial z} \right) \sin\theta\cos\varphi + \left(\frac{\partial E_z}{\partial y} - \frac{\partial E_y}{\partial z} \right) \sin\theta\sin\varphi \right]_{z=0} \\ &\left[\sin\theta\cos\varphi \hat{\mathbf{a}}_x + \sin\theta\sin\varphi \hat{\mathbf{a}}_y + \cos\theta \hat{\mathbf{a}}_z \right] \Bigg\} \mathrm{e}^{-i\mathbf{k_0}\cdot\boldsymbol{\rho}} dS_1,\end{aligned} \tag{2.40}$$

where $\boldsymbol{\rho}$ is the vector (x, y, z) on S_1, (R, θ, φ) are the radius, polar angle and azimuthal angle measured from the origin to (x', y', z'), $\hat{\mathbf{a}}_x$, $\hat{\mathbf{a}}_y$ and $\hat{\mathbf{a}}_z$ represent the x, y and z components of $\mathbf{E}$, respectively, and $\mathbf{k_0}$ is the radar wavevector given by

$$\mathbf{k_0} = k_0(\sin\theta\cos\varphi, \sin\theta\sin\varphi, \cos\theta).$$

Figure 2.2 gives a visual representation of these quantities.

Now, the scattered electric field, given in equations 2.37, 2.38 and 2.39, is substituted into equation 2.40. The specular term $2\mathrm{e}^{ik_0 x}\mathrm{e}^{-i\omega_0 t}$ in equation 2.39 is henceforth omitted, as including it in the following radar cross section calculation proves unnecessary. The term contributes to scatter at the incident frequency (i.e. zero Doppler) in the specular direction, which is not relevant to ocean sensing because the zero Doppler frequency is usually contaminated with signals scattered from stationary objects, such as land. Furthermore, the receiver tends not to be in the specular direction. The contibution of this term at zero Doppler is somewhat intuitive though, as this particular term describes scatter from a perfectly smooth

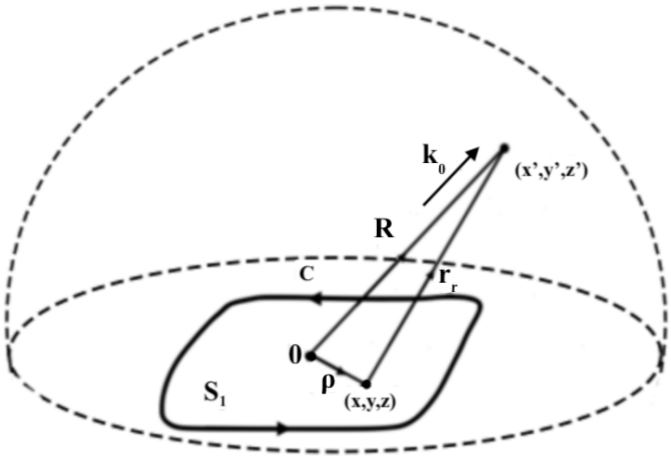

Figure 2.2: The finite scattering surface, S_1, with boundary C, as part of a hemispherical surface. The vector $\boldsymbol{\rho}$ denotes the position on S_1 (x, y, z); the vector $\mathbf{r}_r$ is the vector from (x, y, z) to some distant point (x', y', z') where the scattered electric field is desired. The vector $\mathbf{k_0}$ is the radar wavevector in the direction of the scattered radio wave, $\mathbf{R}$.

surface. With this omission, equation 2.40 gives

$$\begin{aligned} E_{x'}(t) =& \frac{2ie^{ik_0R}}{4\pi R}\int_{S_1}\sum_{mnl}\Big\{ \big(b(m,n)(1-\sin^2\theta\cos^2\varphi)+k_0\cos\theta\big)\{x \text{ terms}\} \\ &+\sum_{mnl}(-b(m,n)\sin^2\theta\sin\varphi\cos\varphi)\{y \text{ terms}\} \\ &+\sum_{mnl}(am(\sin^2\theta\cos^2\varphi-1)+an\sin^2\theta\sin\varphi\cos\varphi)\frac{1}{b(m,n)}\{z \text{ terms}\} \\ &\Big\} E(m,n,0,l)e^{-i\mathbf{k_0}\cdot\boldsymbol{\rho}}dS_1 \end{aligned} \tag{2.41}$$

where

$$\begin{aligned} \{x \text{ terms}\} =& -i(am-k_0)P(m-\nu,n,l) \\ &+\sum_{qrs}\left[a^2(m-q)(\nu-q)k_0+(k_0-am)b^2(q,r)\right]Q(m,n,l,q,r,s) \end{aligned} \tag{2.42}$$

$$\begin{aligned} \{y \text{ terms}\} =& -ianP(m-\nu,n,l) \\ &+\sum_{qrs}\left[a^2(n-r)(\nu-q)k_0-anb^2(q,r)\right]Q(m,n,l,q,r,s) \end{aligned} \tag{2.43}$$

$$\begin{aligned} \{z \text{ terms}\} =& -i\left(a(m-\nu)k_0+b^2(m,n)\right)P(m-\nu,n,l) \\ &+\sum_{qrs}\big[a^3(q-\nu)(m^2+n^2-qm-rn)k_0 \\ &+a\left(a(m^2+n^2)-mk_0\right)b^2(q,r)\big]Q(m,n,l,q,r,s). \end{aligned} \tag{2.44}$$

Similarly,

$$\begin{aligned} E_{y'}(t) =& \frac{2i\mathrm{e}^{ik_0R}}{4\pi R}\int_{S_1}\sum_{mnl}\Bigg\{ \left(-b(m,n)(\sin^2\theta\cos\varphi\sin\varphi\right)\{x \text{ terms}\} \\ &+\sum_{mnl}(b(m,n)(1-\sin^2\theta\sin^2\varphi)+k_0\cos\theta)\{y \text{ terms}\} \\ &+\sum_{mnl}\left(am\sin^2\theta\cos\varphi\sin\varphi+an(\sin^2\theta\sin^2\varphi-1)\right)\frac{1}{b(m,n)}\{z \text{ terms}\} \\ &\Bigg\} E(m,n,0,l)\mathrm{e}^{-i\mathbf{k_0}\cdot\boldsymbol{\rho}}dS_1 \end{aligned} \tag{2.45}$$

and

$$\begin{aligned} E_{z'}(t) =& \frac{2i\mathrm{e}^{ik_0R}}{4\pi R}\int_{S_1}\sum_{mnl}\Bigg\{ \left(-k_0\sin\theta\cos\varphi-\sin\theta\cos\theta\cos\varphi b(m,n)\right)\{x \text{ terms}\} \\ &+\sum_{mnl}\left(-k_0\sin\theta\sin\varphi-\sin\theta\cos\theta\sin\varphi b(m,n)\right)\{y \text{ terms}\} \\ &+\sum_{mnl}\left(am\sin\theta\cos\theta\cos\varphi+an\sin\theta\sin\varphi\cos\theta\right)\frac{1}{b(m,n)}\{z \text{ terms}\} \\ &\Bigg\} E(m,n,0,l)\mathrm{e}^{-i\mathbf{k_0}\cdot\boldsymbol{\rho}}dS_1. \end{aligned} \tag{2.46}$$

To calculate equations 2.41, 2.45 and 2.46, the integral over S_1 - or equivalently over x and y (where the surface is size $L\times L$) - must be evaluated. As the only terms with x and y dependence are $\mathrm{e}^{i(a(mx+ny))}$ and $\mathrm{e}^{-i\mathbf{k_0}\cdot\boldsymbol{\rho}}$, we therefore need to calculate

$$\iint_{-L/2}^{L/2}\mathrm{e}^{i(a(mx+ny))}\mathrm{e}^{-i\mathbf{k_0}\cdot\boldsymbol{\rho}}\,dx\,dy,$$

which, using the definitions of $\mathbf{k_0}$ and $\boldsymbol{\rho}$, is equal to

$$L^2\,\mathrm{sinc}(XR)\,\mathrm{sinc}(YR), \tag{2.47}$$

where $XR=\frac{L}{2}\left(am-k_0\sin\theta\cos\varphi\right)$ and $YR=\frac{L}{2}\left(an-k_0\sin\theta\sin\varphi\right)$. Therefore the scat-

tered electric fields from a finite surface, given in equations 2.41, 2.45 and 2.46, become

$$\begin{aligned}
E_{x'}(t) =& \frac{2ie^{ik_0R}}{4\pi R}L^2\sum_{mnl}\Bigg\{\Bigg[\ \big(b(m,n)(1-\sin^2\theta\cos^2\varphi)+k_0\cos\theta\big)\ \{x\text{ terms}\}\\
&+\sum_{mnl}(-b(m,n)\sin^2\theta\sin\varphi\cos\varphi)\{y\text{ terms}\}\\
&+\sum_{mnl}(am(\sin^2\theta\cos^2\varphi-1)+an\sin^2\theta\sin\varphi\cos\varphi)\frac{\{z\text{ terms}\}}{b(m,n)}\ \Bigg]\\
&\operatorname{sinc}(XR)\operatorname{sinc}(YR)\Bigg\}e^{-i(wl+\omega_0)t},
\end{aligned} \tag{2.48}$$

$$\begin{aligned}
E_{y'}(t) =& \frac{2ie^{ik_0R}}{4\pi R}L^2\sum_{mnl}\Bigg\{\Bigg[\ \big(-b(m,n)(\sin^2\theta\cos\varphi\sin\varphi)\big)\ \{x\text{ terms}\}\\
&+\sum_{mnl}(b(m,n)(1-\sin^2\theta\sin^2\varphi)+k_0\cos\theta)\{y\text{ terms}\}\\
&+\sum_{mnl}\big(am\sin^2\theta\cos\varphi\sin\varphi+an(\sin^2\theta\sin^2\varphi-1)\big)\ \frac{\{z\text{ terms}\}}{b(m,n)}\ \Bigg]\\
&\operatorname{sinc}(XR)\operatorname{sinc}(YR)\Bigg\}e^{-i(wl+\omega_0)t},
\end{aligned} \tag{2.49}$$

$$\begin{aligned}
E_{z'}(t) =& \frac{2ie^{ik_0R}}{4\pi R}L^2\sum_{mnl}\Bigg\{\Bigg[\ (-k_0\sin\theta\cos\varphi-\sin\theta\cos\theta\cos\varphi b(m,n))\ \{x\text{ terms}\}\\
&+\sum_{mnl}(-k_0\sin\theta\sin\varphi-\sin\theta\cos\theta\sin\varphi b(m,n))\ \{y\text{ terms}\}\\
&+\sum_{mnl}(am\sin\theta\cos\theta\cos\varphi+an\sin\theta\sin\varphi\cos\theta)\ \frac{\{z\text{ terms}\}}{b(m,n)}\ \Bigg]\\
&\operatorname{sinc}(XR)\operatorname{sinc}(YR)\Bigg\}e^{-i(wl+\omega_0)t}.
\end{aligned} \tag{2.50}$$

2.3.2 The Vertically Polarised Components

The scattered fields in equations 2.48-2.50 include components of all different polarisations. As the receiver will be designed to receive only vertically polarised components, the rest must be removed. To do this, we notice that the spherical unit vector $\hat{\boldsymbol{\theta}}$ has the same orientation as the defined vertically polarised electric field. Therefore, the vertically polarised components are found by calculating $\mathbf{E}\cdot\hat{\boldsymbol{\theta}}$, i.e.

$$E_\theta = E_{x'}\cos\varphi\cos\theta + E_{y'}\sin\varphi\cos\theta - E_{z'}\sin\theta \tag{2.51}$$

and, using equations 2.48, 2.49 and 2.50, equation 2.51 becomes

$$\begin{aligned} E_\theta = \frac{i\mathrm{e}^{ik_0R}}{2\pi R}L^2 \sum_{mnl} \Bigg\{ \Bigg[& \cos\varphi(k_0 + b(m,n)\cos\theta)\{x \text{ terms}\} \\ & + \sum_{mnl} \sin\varphi(k_0 + b(m,n)\cos\theta)\{y \text{ terms}\} \\ & - \sum_{mnl} \cos\theta(am\cos\varphi + an\sin\varphi \frac{\{z \text{ terms}\}}{b(m,n)} \Bigg] \\ & \operatorname{sinc}(XR)\operatorname{sinc}(YR) \Bigg\} \mathrm{e}^{-i(wl+\omega_0)t}. \end{aligned} \tag{2.52}$$

By defining

$$B(t) = \sum_{mnl} \cos\varphi(k_0 + b(m,n)\cos\theta)\operatorname{sinc}(XR)\operatorname{sinc}(YR)\mathrm{e}^{-i(wl+\omega_0)t} \tag{2.53}$$

$$C(t) = \sum_{mnl} \sin\varphi(k_0 + b(m,n)\cos\theta)\operatorname{sinc}(XR)\operatorname{sinc}(YR)\mathrm{e}^{-i(wl+\omega_0)t} \tag{2.54}$$

$$D(t) = \sum_{mnl} -\cos\theta(am\cos\varphi + an\sin\varphi)\frac{\operatorname{sinc}(XR)\operatorname{sinc}(YR)}{b(m,n)}\mathrm{e}^{-i(wl+\omega_0)t}, \tag{2.55}$$

and

$$\begin{aligned} \{x \text{ terms}\} &= -i(am - k_0)P(m-\nu,n,l) \\ &\quad + \sum_{qrs} \left[a^2(m-q)(\nu-q)k_0 + (k_0 - am)b^2(q,r)\right] Q(m,n,l,q,r,s) \\ &= -ix_1 P(m-\nu,n,l) + \sum_{qrs} x_2 Q(m,n,l,q,r,s) \end{aligned} \tag{2.56}$$

$$\begin{aligned} \{y \text{ terms}\} &= -ianP(m-\nu,n,l) \\ &\quad + \sum_{qrs} \left[a^2(n-r)(\nu-q)k_0 - anb^2(q,r)\right] Q(m,n,l,q,r,s) \\ &= -iy_1 P(m-\nu,n,l) + \sum_{qrs} y_2 Q(m,n,l,q,r,s) \end{aligned} \tag{2.57}$$

$$\begin{aligned} \{z \text{ terms}\} &= -i\left(a(m-\nu)k_0 + b^2(m,n)\right) P(m-\nu,n,l) \\ &\quad + \sum_{qrs} \Big[a^3(q-\nu)(m^2+n^2-qm-rn)k_0 \\ &\qquad + a\left(a(m^2+n^2) - mk_0\right) b^2(q,r)\Big] Q(m,n,l,q,r,s) \\ &= -iz_1 P(m-\nu,n,l) + \sum_{qrs} z_2 Q(m,n,l,q,r,s), \end{aligned} \tag{2.58}$$

equation 2.52 can be written as

$$E_\theta(t) = \frac{i\mathrm{e}^{ik_0R}}{2\pi R}L^2\sum_{mnl}\Bigg(B(t)\left\{-ix_1P(m-\nu,n,l)+\sum_{qrs}x_2Q(m,n,l,q,r,s)\right\} + C(t)\left\{-iy_1P(m-\nu,n,l)+\sum_{qrs}y_2Q(m,n,l,q,r,s)\right\} + D(t)\left\{-iz_1P(m-\nu,n,l)+\sum_{qrs}z_2Q(m,n,l,q,r,s)\right\}\Bigg). \tag{2.59}$$

2.3.2.1 Second Order Hydrodynamic Scatter

In the perturbation method of Rice [78], used to derive the scattered electric field in section 2.2, the Fourier coefficients of the field, A_{mnl}, B_{mnl} and C_{mnl}, were expanded around the flat surface to give an expression with first and second order components. The first order components represent the single scattering of one electromagnetic wave, to the receiver, from one ocean wave. The second order components represent doubly scattered electromagnetic waves, to the receiver, from two single ocean waves. The order of the ocean wave, currently denoted by $P(m-\nu,n,l)$, has not yet been considered and is assumed to be first order. However, in making such an assumption, a second order contribution from first order scattering from second order ocean waves is missed, where a second order ocean wave is the result of the nonlinear interaction between two first order ocean waves.

To allow for the second order hydrodynamic effects, Weber and Barrick [98] used a perturbation method to relate the second order coefficients $P^{(2)}(\mathbf{k},\omega)$, of a surface defined by $z=\sum_{\mathbf{k},\omega}P(\mathbf{k},\omega)\mathrm{e}^{i\mathbf{k}\cdot\mathbf{r}-i\omega t}$, to the first order coefficients $P^{(1)}(\mathbf{k},\omega)$. Their method involved expanding the surface height Fourier coefficients around the flat surface, i.e.

$$P(\mathbf{k},\omega) = P^{(1)}(\mathbf{k},\omega) + P^{(2)}(\mathbf{k},\omega) + \ldots,$$

alongside boundary conditions from the equations of motion, also expanded to second order. The solution was only valid for *deep* oceans, that is where the ocean depth, d, is greater than the wavelength of the ocean wave to be extracted. Barrick and Lipa [11] then extended the work of Weber and Barrick [98] to include the depth of the ocean, and verified it to be an important inclusion for the longer second order waves that the radar receives scatter from. As nonlinear interactions are more prominent in shallow waters [11] and most operational HF radars will be situated on the coast where shallow waters are more likely, ocean depth is an important inclusion. They showed that for ocean waves with wavevectors $\mathbf{k_1}$ and $\mathbf{k_2}$,

with corresponding angular frequencies ω_1 and ω_2 (related by the ocean dispersion relation in equation 1.15),

$$P^{(2)}(\mathbf{k}'', \omega'') = \sum_{\mathbf{k_1 k_2}} \sum_{\omega_1 \omega_2} \Gamma_H(\mathbf{k_1}, \omega_1, \mathbf{k_2}, \omega_2) P^{(1)}(\mathbf{k_1}, \omega_1) P^{(1)}(\mathbf{k_2}, \omega_2), \tag{2.60}$$

where $\mathbf{k}'' = \mathbf{k_1} + \mathbf{k_2}$, $\omega'' = \omega_1 + \omega_2$, and

$$\begin{aligned} \Gamma_H = \frac{1}{2} \Bigg\{ & k_1 \tanh(k_1 d) + k_2 \tanh(k_2 d) + \frac{\omega''}{g} \frac{(\omega_1^3 \operatorname{csch}^2(k_1 d) + \omega_2^3 \operatorname{csch}^2(k_2 d))}{(\omega''^2 - g k'' \tanh(k'' d))} \\ & + \frac{(k_1 k_2 \tanh(k_1 d) \tanh(k_2 d) - \mathbf{k_1} \cdot \mathbf{k_2})}{\sqrt{k_1 k_2 \tanh(k_1 d) \tanh(k_2 d)}} \left(\frac{g k'' \tanh(k'' d) + \omega''^2}{g k'' \tanh(k'' d) - \omega''^2} \right) \Bigg\}, \end{aligned} \tag{2.61}$$

is called the *hydrodynamic coupling coefficient*, in which k_i denotes the magnitude of wavevector $\mathbf{k_i}$.

To include the second order hydrodynamic effects in the scattered electric field, we expand $P(m-\nu, n, l)$ into $P^{(1)}(m-\nu, n, l) + P^{(2)}(m-\nu, n, l)$ and then substitute in the value of $P^{(2)}(m-\nu, n, l)$ using equation 2.60. The expansion gives

$$\begin{aligned} E_\theta(t) = \frac{i e^{ik_0 R}}{2\pi R} L^2 \sum_{mnl} \Bigg\{ & - i(B(t)x_1 + C(t)y_1 + D(t)z_1) \left(P^{(1)}(m-\nu, n, l) + P^{(2)}(m-\nu, n, l) \right) \\ & + \sum_{qrs} (B(t)x_2 + C(t)y_2 + D(t)z_2) Q(m, n, l, q, r, s) \Bigg\}, \end{aligned}$$

and as per equation 2.60 (by letting $\mathbf{k}'' = (m-\nu, n)$ and $\omega = l$),

$$P^{(2)}(m-\nu, n, l) = \sum_{mnlqrs} \Gamma_H P^{(1)}(q-\nu, r, s) P^{(1)}(m-q, n-r, l-s)$$

and so

$$\begin{aligned} E_\theta(t) = \frac{i e^{ik_0 R}}{2\pi R} L^2 \sum_{mnl} \Bigg\{ & - i(B(t)x_1 + C(t)y_1 + D(t)z_1) P^{(1)}(m-\nu, n, l) \\ & + \sum_{qrs} \Bigg\{ - i(B(t)x_1 + C(t)y_1 + D(t)z_1) \Gamma_H b(q, r) \\ & + (B(t)x_2 + C(t)y_2 + D(t)z_2) \Bigg\} Q(m, n, l, q, r, s) \Bigg\}, \end{aligned} \tag{2.62}$$

using the definition of Q from equation 2.35.

§ 2.4 Calculate the Radar Cross Section from the Scattered Electric Field

2.4.1 Radar Cross Section Expression

The radar cross section, σ, definition was given in equation 1.13. Redefining σ as the radar cross section per unit area, where in this case the scattering surface is of size $L \times L$,

$$\sigma = \lim_{R\to\infty} 4\pi R^2 \frac{|E_s|^2}{L^2}, \tag{2.63}$$

where σ has been redefined to σ/L^2 and, as in section 2.2, $E_0 = 1$. As the surface is time-varying and the motion induces doppler shifts on the incident radio frequency, the radar cross section will be a frequency spectrum, defined as $\sigma(\omega)$. Therefore, the scattered electric field, appearing in the radar cross section, is replaced with power spectral density which will lead to a distribution over radio wave frequency, ω. Explicitly,

$$\sigma(\omega) = \lim_{R\to\infty} 4\pi R^2 \frac{\Phi(\omega)}{L^2}, \tag{2.64}$$

where $\Phi(\omega)$ is the power spectral density. By the Wiener-Khinchin theorem, the power spectral density of an ergodic function of time, $f(t)$, is defined as the Fourier transform of the autocorrelation of the function. The ocean is often assumed to be ergodic (see Kinsman [54] for a discussion on the subject), and so the power spectral density can be calculated by

$$\Phi(\omega) = \frac{1}{2\pi} \int_{-\infty}^{\infty} \langle f(t_1) f^*(t_2) \rangle \mathrm{e}^{-i\omega\tau}\, d\tau, \tag{2.65}$$

where the Fourier transform[2] is defined as

$$\mathcal{F}(f(\tau)) = \frac{1}{2\pi} \int_{-\infty}^{\infty} f(\tau) \mathrm{e}^{-i\omega\tau}\, d\tau, \tag{2.66}$$

and an ensemble average is denoted by $\langle\rangle$. Additionally, the definition of the power in the signal, σ_0, using the inverse Fourier transform, is

$$\sigma_0 = \int \sigma(\omega)\, d\omega.$$

[2] Rice [78] and Barrick [5] define their Fourier transforms with a factor of $1/\pi$, however Johnstone [50] defines his with a factor of $1/2\pi$. This is the cause of the scalar difference in the radar cross section expressions derived by Barrick and Johnstone.

By substituting $E_\theta(t)$ for $f(t)$ in equation 2.65, and then substituting the resulting expression into equation 2.64, the radar cross section per unit area per unit frequency is given by

$$\sigma(\omega) = \lim_{R\to\infty} 4\pi R^2 \frac{\mathcal{F}\left[\langle E_\theta(t_1)E_\theta^*(t_2)\rangle\right]}{L^2}. \tag{2.67}$$

In equation 2.67, firstly the average of the term $E_\theta(t_1)E_\theta^*(t_2)$ is calculated, where E_θ is that in equation 2.62. Therefore, the average of

$$\begin{aligned}
&E_\theta(t_1)E_\theta^*(t_2) = \\
&\quad \frac{L^4}{4\pi^2R^2}\sum_{mnl}\Bigg\{ -i(B(t_1)x_1 + C(t_1)y_1 + D(t_1)z_1)P^{(1)}(m-\nu,n,l) \\
&\qquad + \sum_{qrs}\left[-i(B(t_1)x_1 + C(t_1)y_1 + D(t_1)z_1)\Gamma_H b(q,r)\right. \\
&\qquad\quad \left. +(B(t_1)x_2 + C(t_1)y_2 + D(t_1)z_2)\right] Q(m,n,l,q,r,s)\Bigg\} \\
&\sum_{m'n'l'}\Bigg\{ i(B'^*(t_2)x_1' + C'^*(t_2)y_1' + D'^*(t_2)z_1')P^{(1)'*}(m'-\nu,n',l') \\
&\qquad + \sum_{q'r's'}\left[i(B'^*(t_2)x_1' + C'^*(t_2)y_1' + D'^*(t_2)z_1')\Gamma_H b^*(q',r')\right. \\
&\qquad\quad \left. +(B'^*(t_2)x_2' + C'^*(t_2)y_2' + D'^*(t_2)z_2')\right] Q'^*(m',n',l',q',r',s')\Bigg\},
\end{aligned} \tag{2.68}$$

is required, where $'$ denotes the definition of the relevant function in terms of m', n', l', q', r' and s'. To calculate the average of equation 2.68, the averages of the Fourier coefficients $P(m,n,l)$ and $Q(m,n,l,q,r,s)$ must be known. Recalling that Q, defined in equation 2.35, is the product of two P terms, the relevant averages are

1 $\langle PP^*\rangle$

2 $\langle QP\rangle = \langle PPP\rangle$

3 $\langle QQ^*\rangle = \langle PPP^*P^*\rangle$

and in order to calculate these averages, the following properties of P are used.

- Firstly, assume that the random surface fluctuations that these Fourier coefficients represent are normally distributed about zero. Therefore,

$$\langle P(m,n,l)\rangle = 0. \tag{2.69}$$

- Secondly, as the surface is real-valued, $f(x,y,t)$ must be equal to $f^*(x,y,t)$ which is true when

$$P(-m,-n,-l) = P^*(m,n,l). \tag{2.70}$$

- Thirdly, from Thomas [89],

$$\langle P_1P_2P_3\rangle = \langle P_1\rangle\langle P_2P_3\rangle + \langle P_2\rangle\langle P_1P_3\rangle + \langle P_3\rangle\langle P_1P_2\rangle \tag{2.71}$$

and

$$\begin{aligned}\langle P_1P_2P_3P_4\rangle =&\langle P_1P_2\rangle\langle P_3P_4\rangle + \langle P_1P_3\rangle\langle P_2P_4\rangle + \langle P_1P_4\rangle\langle P_2P_3\rangle \\ &- 2\langle P_1\rangle\langle P_2\rangle\langle P_3\rangle\langle P_4\rangle.\end{aligned} \tag{2.72}$$

By equation 2.69, $\langle P_i\rangle = 0$ and therefore equations 2.71 and 2.72 become

$$\langle P_1P_2P_3\rangle = 0 \tag{2.73}$$

and

$$\langle P_1P_2P_3P_4\rangle = \langle P_1P_2\rangle\langle P_3P_4\rangle + \langle P_1P_3\rangle\langle P_2P_4\rangle + \langle P_1P_4\rangle\langle P_2P_3\rangle. \tag{2.74}$$

- Finally (see Appendix A for the proof),

$$\langle P(m,n,l)P(q,r,s)\rangle = \begin{cases}\dfrac{(2\pi)^3 S_s(p,q,wl)}{L^2T} & \text{if } q,r,s = -m,-n,-l \\ 0 & \text{otherwise}\end{cases} \tag{2.75}$$

where $S_s(p,q,wl)$ is the surface roughness spectrum given in terms of

$$p = am \qquad\qquad q = an. \tag{2.76}$$

These averages can now be used to find the average of equation 2.68. By equation 2.73,

$\langle P_1 P_2 P_3 \rangle = 0$, and so

$$\begin{aligned}\langle E_\theta(t_1)\ E_\theta^*(t_2)\rangle = \\ \frac{L^4}{4\pi^2 R^2}\sum_{\substack{mnl\\ m'n'l'}}\Big\{-i\zeta(t_1)i\zeta'^*(t_2)\left\langle P^{(1)}(m-\nu,n,l)P^{(1)'*}(m'-\nu,n',l')\right\rangle \\ +\sum_{\substack{qrs\\ q'r's'}}\Big\{\ [-i\zeta(t_1)b(q,r)\Gamma_H+\xi(t_1)] \\ \left[i\zeta'^*(t_2)b^*(q',r')\Gamma'_H+\xi'^*(t_2)\right]\left\langle QQ'^*\right\rangle\ \Big\}\Big\},\end{aligned} \tag{2.77}$$

where, for brevity,

$$\zeta(t) = B(t)x_1 + C(t)y_1 + D(t)z_1 \qquad\qquad \xi(t) = B(t)x_2 + C(t)y_2 + D(t)z_2$$

and the arguments of $Q(m,n,l,q,r,s)$ have been omitted. Inputting equation 2.77 into the radar cross section calculation in equation 2.67, then gives

$$\begin{aligned}\sigma(\omega) = \frac{1}{\pi}\mathcal{F}\Bigg[L^2\sum_{\substack{mnl\\ m'n'l'}}\Big\{\zeta(t_1)\zeta'^*(t_2)\left\langle P^{(1)}(m-\nu,n,l)P^{(1)'*}(m'-\nu,n',l')\right\rangle \\ +\sum_{\substack{qrs\\ q'r's'}}\Big\{\ [-i\zeta(t_1)b(q,r)\Gamma_H+\xi(t_1)]\left[i\zeta'^*(t_2)b^*(q',r')\Gamma'_H+\xi'^*(t_2)\right]\left\langle QQ'^*\right\rangle\ \Big\}\Big\}\Bigg].\end{aligned} \tag{2.78}$$

In equation 2.78, the average involving two P terms represents first order scatter and that involving two Q terms represents second order. Therefore, the radar cross section can be written as

$$\sigma(\omega) = \sigma^{(1)}(\omega) + \sigma^{(2)}(\omega), \tag{2.79}$$

where the bracketed superscript denotes the order.

2.4.2 First Order Radar Cross Section

From equation 2.78, the first order radar cross section is

$$\sigma^{(1)}(\omega) = \frac{1}{\pi}\mathcal{F}\left[L^2\sum_{\substack{mnl\\ m'n'l'}}\left\{\zeta(t_1)\zeta'^*(t_2)\left\langle P^{(1)}(m-\nu,n,l)P^{(1)'*}(m'-\nu,n',l')\right\rangle\right\}\right],$$

which can be denoted as

$$\sigma^{(1)}(\omega) = \frac{1}{\pi}\Phi_{\zeta\zeta'^*},$$

where the factors L^2 and PP'^* are implied. More precisely,

$$\sigma^{(1)}(\omega) = \frac{1}{\pi}\Phi^{(1)}_{(Bx_1+Cy_1+Dz_1)\left(B'^*x_1'+C'^*y_1'+D'^*z_1'\right)}$$

which is equivalent to finding

$$\sigma^{(1)}(\omega) = \frac{1}{\pi}\left(\Phi^{(1)}_{Bx_1B'^*x_1'} + \Phi^{(1)}_{Cy_1C'^*y_1'} + \Phi^{(1)}_{Dz_1D'^*z_1'} + \Phi^{(1)}_{Bx_1C'^*y_1'} + \cdots\right). \tag{2.80}$$

To calculate the individual terms in equation 2.80, equation 2.70 is used to enforce restrictions on the summation indices and then equation 2.75 is used to introduce the roughness spectrum, S. For completeness, a walkthrough of the calculation of $\Phi^{(1)}_{Bx_1C'^*y_1'}$ is given in Appendix B, along with all of the other individual terms. Upon calculation of equation 2.80,

$$\sigma^{(1)}(\omega) = 2^4\pi k_0^4(\sin\theta - \cos\varphi)^2 S_s(k_0\sin\theta\cos\varphi - k_0, k_0\sin\theta\sin\varphi, \omega - \omega_0) \tag{2.81}$$

and, since we are interested in ground wave propagation, let $\theta = 90^\circ$ and equation 2.81 becomes

$$\sigma^{(1)}(\omega) = 2^4\pi k_0^4(1 - \cos\varphi)^2 S_s(k_0\cos\varphi - k_0, k_0\sin\varphi, \omega - \omega_0). \tag{2.82}$$

As the bistatic angle, φ_{bi}, (see figure 2.3) is

$$\varphi_{bi} = \frac{1}{2}(\pi - \varphi) \tag{2.83}$$

and the *Bragg wavevector* is

$$\mathbf{k_B} = -2k_0\cos\varphi_{bi}(\cos\varphi_{bi}, -\sin\varphi_{bi}), \tag{2.84}$$

equation 2.82 can then be written in terms of φ_{bi} and $\mathbf{k_B}$ as

$$\sigma^{(1)}(\omega) = 2^6\pi k_0^4\cos^4\varphi_{bi} S_s(\mathbf{k_B}, \omega - \omega_0). \tag{2.85}$$

The dispersion relation of ocean waves, discussed in section 1.2, relates an ocean wavenumber,

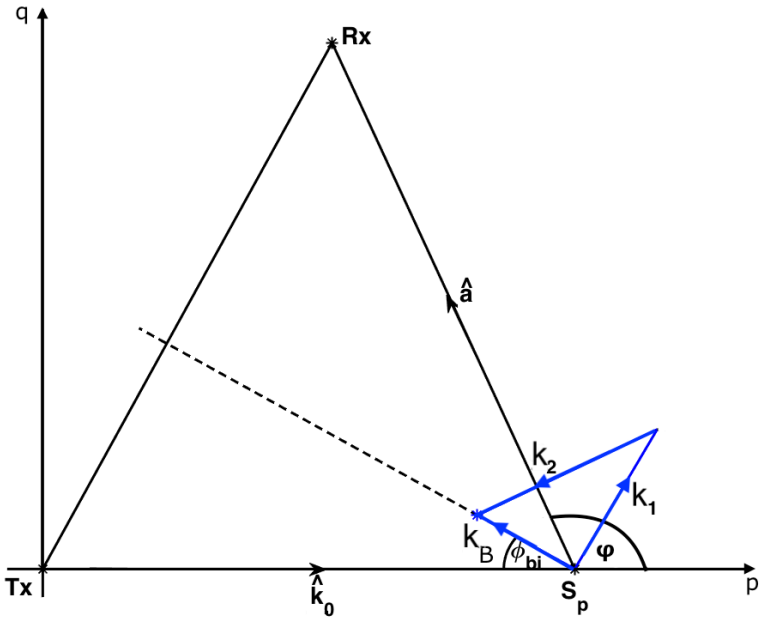

Figure 2.3: Scattering geometry for a bistatic radar where T_x, S_p and R_x denote the transmitter, scatter patch and receiver respectively, φ_{bi} is the bistatic angle, $\mathbf{k_0}$ is the radar wavevector and, p and q are spatial wavenumbers where p is in the direction of the emitted radio wave. The Bragg wavevector $\mathbf{k_B}$ is shown along with the wavevectors $\mathbf{k_1}$ and $\mathbf{k_2}$ where $\mathbf{k_B} = \mathbf{k_1} + \mathbf{k_2}$.

k, and ocean depth, d, to its unique angular frequency, ω_g, by

$$\omega_g^2 = gk\tanh(kd). \tag{2.86}$$

Therefore, Barrick [5] related the ocean spectrum term $S_s(\mathbf{k},\omega)$ to the more simple spectrum, $S_s(\mathbf{k})$, by redefining the surface height, originally given in equation 2.1, as

$$\begin{aligned} f(x,y,t) = \sum_{mn=-\infty}^{\infty} P_+(m,n)\mathrm{e}^{ia(mx+ny)-i\mathrm{sgn}(m)\omega_g t} \\ + \sum_{mn=-\infty}^{\infty} P_-(m,n)\mathrm{e}^{ia(mx+ny)+i\mathrm{sgn}(m)\omega_g t}, \end{aligned} \tag{2.87}$$

where $P_+(m,n)$ and $P_-(m,n)$ represent waves travelling in the positive and negative x directions respectively. He then calculated $S_+(p,q)$ and $S_-(p,q)$ in the same way as $S_s(p,q,\omega)$ (see Appendix A) and equated the results to give

$$S_s(p,q,\omega) = S_+(p,q)\delta(\omega - \mathrm{sgn}(p)w_g) + S_-(p,q)\delta(\omega + \mathrm{sgn}(p)w_g). \tag{2.88}$$

Implementing equation 2.88 in equation 2.85, and relabelling the Doppler shift $\omega - \omega_0$ to ω gives

$$\sigma^{(1)}(\omega) = 2^6 \pi k_0^4 \cos^4 \varphi_{bi} \sum_{m_B=\pm 1} S_s(m_B \mathbf{k_B}) \delta(\omega - m_B \omega_B), \tag{2.89}$$

where

$$\omega_B = \sqrt{2 g k_0 \cos \varphi_{bi} \tanh(2 k_0 d \cos \varphi_{bi})} \tag{2.90}$$

is the *Bragg frequency* and m_B has been introduced to write the expression in a more convenient form.

The spectrum $S_s(\mathbf{k})$ is symmetrical, however the oceanographer-measured spectra, $S(\mathbf{k})$, is asymmetrical. Therefore, like Barrick [8], the relation

$$S_s(\mathbf{k}) = \frac{1}{2} S(\mathbf{k}), \tag{2.91}$$

is used, which upon substitution into equation 2.89 gives

$$\sigma^{(1)}(\omega) = 2^5 \pi k_0^4 \cos^4 \varphi_{bi} \sum_{m_B=\pm 1} S(m_B \mathbf{k_B}) \delta(\omega - m_B \omega_B). \tag{2.92}$$

2.4.3 Second Order Radar Cross Section

In calculating the second order radar cross section contribution, $\sigma^{(2)}(\omega)$, the relevant term from equation 2.78 is

$$\frac{1}{\pi} \mathcal{F} \left[L^2 \sum_{\substack{mnl \\ qrs}} \sum_{\substack{m'n'l' \\ q'r's'}} \left[-i\zeta(t_1) b(q,r) \Gamma_H + \xi(t_1) \right] \left[i\zeta'^*(t_2) b^*(q',r') \Gamma'_H + \xi'^*(t_2) \right] \left\langle QQ'^* \right\rangle \right], \tag{2.93}$$

which can be denoted by

$$\sigma^{(2)}(\omega) = \frac{1}{\pi} \Phi(\omega)^{(2)}_{[-i\zeta b(q,r)\Gamma_H + \xi]\left[i\zeta'^* b^*(q',r')\Gamma'_H + \xi'^*\right]}, \tag{2.94}$$

where L^2 and QQ'^* are implied. To simplify the calculation, equation 2.94 can split into four separate terms, namely

$$\sigma^{(2)}(\omega)_1 = \frac{1}{\pi} \Phi(\omega)^{(2)}_{\xi\xi'^*}, \tag{2.95}$$

$$\sigma^{(2)}(\omega)_2 = \frac{1}{\pi}\Phi(\omega)^{(2)}_{\zeta\zeta'^* b(q,r)b^*(q',r')\Gamma_H\Gamma'^*_H}, \tag{2.96}$$

$$\sigma^{(2)}(\omega)_3 = \frac{1}{\pi}\Phi(\omega)^{(2)}_{-i\zeta b(q,r)\xi'^*\Gamma_H} \tag{2.97}$$

and

$$\sigma^{(2)}(\omega)_4 = \frac{1}{\pi}\Phi(\omega)^{(2)}_{i\xi\zeta'^* b^*(q',r')\Gamma'^*_H}, \tag{2.98}$$

whereby

$$\sigma^{(2)}(\omega) = \sigma^{(2)}(\omega)_1 + \sigma^{(2)}(\omega)_2 + \sigma^{(2)}(\omega)_3 + \sigma^{(2)}(\omega)_4. \tag{2.99}$$

From equation 2.35 and by utilising equation 2.70,

$$\begin{aligned}\langle QQ'^* \rangle = &\frac{\langle P(q-\nu,r,s)P(m-q,n-r,l-s)}{b(q,r)} \\ &\frac{P(\nu-q',-r',-s')P(q'-m',r'-n',s'-l')\rangle}{b^*(q',r')},\end{aligned} \tag{2.100}$$

which is the average of 4 independent random variables. From equation 2.74,

$$\langle P_1P_2P_3P_4\rangle = \underbrace{\langle P_1P_2\rangle\langle P_3P_4\rangle}_{T_1} + \underbrace{\langle P_1P_3\rangle\langle P_2P_4\rangle}_{T_2} + \underbrace{\langle P_1P_4\rangle\langle P_2P_3\rangle}_{T_3}, \tag{2.101}$$

where the three terms, T_1, T_2 and T_3, give three different sets of conditions for non zero averages by equation 2.75. Therefore each $\sigma^{(2)}(\omega)_i$ in equation 2.99, where $i \in \{1,\ldots,4\}$, is the sum of three different averages,

$$\sigma^{(2)}(\omega)_i = (\sigma^{(2)}(\omega))_{i,1} + (\sigma^{(2)}(\omega))_{i,2} + (\sigma^{(2)}(\omega))_{i,3}, \tag{2.102}$$

where the subscripts 1, 2 and 3 denote the different conditions imposed by T_1, T_2 and T_3. The details of calculating the terms are described in Appendix C. By carrying out the calculations, $(\sigma^{(2)}(\omega))_{i,1}$ is found to be representative of specular scattering at the carrier frequency, for all i, and is therefore not included. For the term $(\sigma^{(2)}(\omega))_1$ in equation 2.95,

$(\sigma^{(2)}(\omega))_{1,2}$ and $(\sigma^{(2)}(\omega))_{1,3}$ are calculated, θ set to 90°, and summed to give

$$\begin{aligned}\sigma^{(2)}(\omega)_1 = 2^4\pi k_0^4 \iiint_{-\infty}^{\infty} \Bigg\{ & \frac{\left[(k_0 - p\cos\varphi - q\sin\varphi)(k_0 - p) - (1-\cos\varphi)b^2(p,q)\right]^2}{b(p,q)b^*(p,q)} \\ & + \left[\frac{(k_0 - p\cos\varphi - q\sin\varphi)(k_0 - p) - (1-\cos\varphi)b^2(p,q)}{b(p,q)}\right] \\ & \left[\frac{(k_0\cos\varphi - p)(\cos\varphi(k_0 - p) - q\sin\varphi)}{b^*(k_0\cos\varphi - p + k_0, k_0\sin\varphi - q)}\right. \\ & \left. - \frac{(1-\cos\varphi)b^2(k_0\cos\varphi - p + k_0, k_0\sin\varphi - q)}{b^*(k_0\cos\varphi - p + k_0, k_0\sin\varphi - q)}\right] \Bigg\} \\ & S_s(k_0\cos\varphi - p, k_0\sin\varphi - q, \omega - \omega_0 - \Omega) \\ & S_s(p - k_0, q, \Omega)\, dp\, dq\, d\Omega.\end{aligned} \tag{2.103}$$

By substituting in φ_{bi} (in equation 2.83) and setting

$$\mathbf{k_1} = (p - k_0, q) \tag{2.104}$$

and

$$\mathbf{k_2} = (-k_0\cos(2\varphi_{bi}) - p, k_0\sin(2\varphi_{bi}) - q), \tag{2.105}$$

equation 2.103 can be written as

$$\sigma^{(2)}(\omega)_1 = 2^4\pi k_0^4 \iiint_{-\infty}^{\infty} \frac{a_1}{b_1}\left(\frac{a_1}{b_1^*} + \frac{a_2}{b_2^*}\right) S_s(\mathbf{k_1}, \Omega) S_s(\mathbf{k_2}, \omega - \omega_0 - \Omega)\, dp\, dq\, d\Omega, \tag{2.106}$$

where

$$a_1 = -k_{1x}(\mathbf{k_2}\cdot\hat{\mathbf{a}}) - 2\cos^2\varphi_{bi}(-k_2^2 + 2k_0\,(\mathbf{k_2}\cdot\hat{\mathbf{a}}))\,, \tag{2.107}$$

$$a_2 = -k_{2x}(\mathbf{k_1}\cdot\hat{\mathbf{a}}) - 2\cos^2\varphi_{bi}(-k_1^2 + 2k_0\,(\mathbf{k_1}\cdot\hat{\mathbf{a}}))\,, \tag{2.108}$$

$$b_1 = \sqrt{-k_2^2 + 2k_0(\mathbf{k_2}\cdot\hat{\mathbf{a}})} \tag{2.109}$$

and

$$b_2 = \sqrt{-k_1^2 + 2k_0(\mathbf{k_1}\cdot\hat{\mathbf{a}})} \tag{2.110}$$

where b_1 and b_2 can be real or imaginary depending on the respective argument and $\hat{\mathbf{a}}$ is a unit vector in the direction of the receiver from the scattering patch (see figure 2.3), namely

$$\hat{\mathbf{a}} = (-\cos(2\varphi_{bi}), \sin(2\varphi_{bi})).$$

Johnstone [50] showed that in the case of second order scatter, equation 2.88 is not strictly true; explicitly, an ocean wave train propagating in the positive x direction does not necessarily impart a negative Doppler shift on the incident radio wave. It was instead shown that an ocean wave with wave vector $\mathbf{k_1}$, defined in equation 2.104, imparts a shift of $\omega_1 = \sqrt{gk_1 \tanh(k_1 d)}$ and, similarly, an ocean wave with wave vector $-\mathbf{k_1}$ imparts a shift of $-\omega_1$. The results for wave vectors $\pm\mathbf{k_2}$ are analogous, and each wave Doppler shifts the incident radio wave by $\pm\omega_2$, respectively, for $\omega_2 = \sqrt{gk_2 \tanh(k_2 d)}$. Therefore,

$$S_s(\mathbf{k_1}, \Omega) = \sum_{m_1=\pm 1} S_s(m_1\mathbf{k_1})\delta\left(\Omega - m_1\omega_1\right)$$

and

$$S_s(\mathbf{k_2}, \omega - \omega_0 - \Omega) = \sum_{m_2=\pm 1} S_s(m_2\mathbf{k_2})\delta\left(\omega - \omega_0 - \Omega - m_2\omega_2\right),$$

and then by $\int \delta(x-y)\delta(z-y)\,dy = \delta(x-z)$,

$$S_s(\mathbf{k_1}, \Omega) S_s(\mathbf{k_2}, \omega - \omega_0 - \Omega) = \sum_{m_1, m_2=\pm 1} S_s(m_1\mathbf{k_1}) S_s(m_2\mathbf{k_2})\delta(\omega - m_1\omega_1 - m_2\omega_2) \tag{2.111}$$

where $\omega - \omega_0$ has been relabelled as ω.

Furthermore, for a function f of $\mathbf{k_1}$ and $\mathbf{k_2}$ (which are both functions of p and q), summed over the whole p,q-plane,

$$\sum_{pq} f(\mathbf{k_1}, \mathbf{k_2}) = \sum_{pq} \frac{f(\mathbf{k_1}, \mathbf{k_2}) + f(\mathbf{k_2}, \mathbf{k_1})}{2}$$

and by this,

$$\begin{aligned} \frac{a_1}{b_1}\left(\frac{a_1}{b_1^*} + \frac{a_2}{b_2^*}\right) &= \frac{1}{2}\left(\frac{a_1}{b_1} + \frac{a_2}{b_2}\right)\left(\frac{a_1}{b_1^*} + \frac{a_2}{b_2^*}\right) \\ &= \frac{1}{2}\left|\frac{a_1}{b_1} + \frac{a_2}{b_2}\right|^2. \end{aligned}$$

Therefore define the electromagnetic coupling coefficient, Γ_E, as

$$\Gamma_E = \frac{1}{2^2 \cos^2 \varphi_{bi}} \left(\frac{a_1}{b_1} + \frac{a_2}{b_2} \right) \tag{2.112}$$

and using this definition alongside equation 2.111, whilst introducing the spectrum $S(\mathbf{k})$ from equation 2.91, means that equation 2.106 can be written as

$$\sigma^{(2)}(\omega)_1 = 2^5 \pi k_0^4 \cos^4 \varphi_{bi} \sum_{m_1,m_2=\pm 1} \iint_{-\infty}^{\infty} |\Gamma_E|^2 S(m_1\mathbf{k_1}) S(m_2\mathbf{k_2}) \, \delta(\omega - m_1\omega_1 - m_2\omega_2)\, dp\, dq. \tag{2.113}$$

A similar process reveals

$$\sigma^{(2)}(\omega)_2 = 2^5 \pi k_0^4 \cos^4 \varphi_{bi} \sum_{m_1,m_2=\pm 1} \iint_{-\infty}^{\infty} \Gamma_H^2 S(m_1\mathbf{k_1}) S(m_2\mathbf{k_2}) \, \delta(\omega - m_1\omega_1 - m_2\omega_2)\, dp\, dq, \tag{2.114}$$

$$\sigma^{(2)}(\omega)_3 = -2^5 i\pi k_0^4 \cos^4 \varphi_{bi} \sum_{m_1,m_2=\pm 1} \iint_{-\infty}^{\infty} \Gamma_H \Gamma_E^* S(m_1\mathbf{k_1}) S(m_2\mathbf{k_2}) \, \delta(\omega - m_1\omega_1 - m_2\omega_2)\, dp\, dq \tag{2.115}$$

and

$$\sigma^{(2)}(\omega)_4 = 2^5 i\pi k_0^4 \cos^4 \varphi_{bi} \sum_{m_1,m_2=\pm 1} \iint_{-\infty}^{\infty} \Gamma_H \Gamma_E S(m_1\mathbf{k_1}) S(m_2\mathbf{k_2}) \, \delta(\omega - m_1\omega_1 - m_2\omega_2)\, dp\, dq. \tag{2.116}$$

Substituting equations 2.113-2.116 into equation 2.94 gives

$$\sigma^{(2)}(\omega) = 2^5 \pi k_0^4 \cos^4 \varphi_{bi} \sum_{m_1,m_2=\pm 1} \iint_{-\infty}^{\infty} \left(|\Gamma_E|^2 + \Gamma_H^2 - i\Gamma_H \Gamma_E^* + i\Gamma_H \Gamma_E \right) S(m_1\mathbf{k_1}) S(m_2\mathbf{k_2}) \delta(\omega - m_1\omega_1 - m_2\omega_2)\, dp\, dq$$

and as, for $a \in \mathbb{C}$ and $b \in \mathbb{R}$,

$$|a - ib|^2 = |a|^2 - iba^* + iba + b^2,$$

the total second order radar cross section is

$$\sigma^{(2)}(\omega) = 2^5\pi k_0^4 \cos^4\varphi_{bi} \sum_{m_1,m_2=\pm 1} \iint_{-\infty}^{\infty} |\Gamma_E - i\Gamma_H|^2 \, S(m_1\mathbf{k_1})S(m_2\mathbf{k_2}) \\ \delta(\omega - m_1\omega_1 \ - m_2\omega_2)\, dp\, dq. \tag{2.117}$$

§ 2.5 Finite Conductivity of the Ocean

The bistatic radar cross section, explicitly in equations 2.92 and 2.117, was derived on the assumption that the ocean is a perfect conductor. However, the ocean is not a perfect conductor, hence why radio waves are attenuated by the surface. Barrick [5] showed that the finite conductivity of the surface can be included by finding the radar cross section for a perfectly conducting surface and then multiplying the result by a loss factor, describing the ohmic losses due to the surface.

However, by assuming the surface is a perfect conductor, the derived electromagnetic coupling coefficient, given in equation 2.121, contains two singularities. The singularities occur when either b_1 or b_2 is equal to zero, given in equations 2.109 and 2.110 respectively. The terms b_1 and b_2 both represent the z component of the propagation constant, defined in equation 2.6, and therefore the singularities occur when the propagation of the wave is solely in the x,y-plane or equivalently when the electric field is completely normal to the surface. For a vertically polarised ground wave, near grazing, propagating along a perfectly conducting surface (as was assumed in the preceding sections) there will indeed be no tangential component of the electric field. However, the ocean is not a perfect conductor and some of the energy is lost to the surface and so there must be a tangential component of the electric field and thus a z component in the propagation constant.

To include the tangential component of the electric field, Johnstone [50] replaces $b(p,q)$ in the denominator of his monostatic electromagnetic coupling coefficient with

$$b(p,q) + \delta k_z,$$

where δk_z corresponds to the z component of the propagation constant caused by the ocean's finite conductivity, say σ_c. To find δk_z, using the method of Jordan [51], Maxwell's equation are used to form two sets of equations - one for the air and one for the finitely conducting ocean, where the differing properties of each medium are included. Boundary conditions are then used to find the value of δk_z. The mathematical details are spared here, but can be found in the work of either Johnstone or Jordan. By following the method, whilst changing

the appropriate terms to account for differing definitions in the plane wave formulations of the electric field, it can be shown that

$$\delta k_z = -k_0 \triangle$$

where

$$\triangle = \frac{Z_s}{Z_\eta},$$

is the *effective surface impedance*, in which Z_s is the *conductor surface impedance* given by

$$Z_s = (1-i)\sqrt{\frac{\omega_0 \mu_0}{2\sigma_c}} \tag{2.118}$$

and Z_η is the *characteristic impedance of free space* given by

$$Z_\eta = \sqrt{\frac{\mu_0}{\epsilon_0}}, \tag{2.119}$$

where, in equations 2.118 and 2.119, μ_0 and ϵ_0 are permeability and permittivity of free space.

The value for $\triangle$ is dependent on ocean conductivity, σ_c and hence no fixed value will be completely accurate, given that temperature change, for one, affects the conductivity of the ocean and that frequently changes. However, in order to elicit calculation of the radar cross section, in this work we will use the value presented by Barrick [9] of

$$\triangle = 0.011 - 0.012i. \tag{2.120}$$

Therefore, the electromagnetic coupling coefficient in equation 2.121 becomes

$$\Gamma_E = \frac{1}{2^2 \cos^2 \varphi_{bi}} \left(\frac{a_1}{b_1 - k_0 \triangle} + \frac{a_2}{b_2 - k_0 \triangle} \right), \tag{2.121}$$

where $\triangle$ is given in equation 2.120.

§ 2.6 Monostatic Radar Cross Section of the Ocean Surface

To check that the radar cross section expression derived in the preceding sections reverts back to the monostatic result presented by Lipa and Barrick [59], let $\varphi = 180°$ and equations 2.92 and 2.117 become

$$\sigma^{(1)}(\omega)^{(M)} = 2^5 \pi k_0^4 \sum_{m_B = \pm 1} S_s(m_B \mathbf{k_B}^{(M)}) \delta(\omega - m_B \omega_B^{(M)}), \tag{2.122}$$

where $\omega_B^{(M)}$ is the monostatic Bragg frequency, $\omega_B^{(M)} = \sqrt{2gk_0 \tanh(2k_0 d)}$, $\mathbf{k_B}^{(M)}$ is the Bragg wavevector defined by $(-2k_0, 0)$, and

$$\sigma^{(2)}(\omega)^{(M)} = 2^5 \pi k_0^4 \sum_{m_1, m_2 = \pm 1} \iint_{-\infty}^{\infty} |\Gamma_T^{(M)}|^2 S_s(m_1 \mathbf{k_1}) S_s(m_2 \mathbf{k_2}) \delta(\omega - m_1\omega_1 - m_2\omega_2)\, dp\, dq, \tag{2.123}$$

respectively. In equation 2.123,

$$\mathbf{k_1} = (p - k_0, q) \qquad\qquad \mathbf{k_2} = (-k_0 - p, -q)$$

and

$$\Gamma_T^{(M)} = \Gamma_E^{(M)} - i\Gamma_H,$$

represents the monostatic coupling coefficient, in which

$$\Gamma_E^{(M)} = \frac{1}{2}\left(\frac{(\mathbf{k_1} \cdot \mathbf{k_0})(\mathbf{k_2} \cdot \mathbf{k_0})/k_0^2 - 2\mathbf{k_1} \cdot \mathbf{k_2}}{\sqrt{\mathbf{k_1} \cdot \mathbf{k_2}}}\right)$$

is the monostatic electromagnetic coupling coefficient. Both radar cross section expressions in equations 2.122 and 2.123 are a factor of 2 smaller than the results of Lipa and Barrick [59] due to differing Fourier transform definitions. Both Rice [78] and Barrick [5] use a Fourier transform of

$$F(\omega) = \frac{1}{\pi} \int_{-\infty}^{\infty} f(\tau) \mathrm{e}^{-i\omega\tau}\, d\tau$$

which is a factor of 2 larger than the one used in this work, given in equation 2.66. The resulting difference in the radar cross section is expected, and when the inverse Fourier transform is taken to calculate the power in the spectrum, σ_0, the results are the same. Explicitly, Barrick calculates

$$\sigma_0^B = \frac{1}{2} \int \sigma_B(\omega)\, d\omega$$

whereas we, here, calculate

$$\sigma_0^H = \int \sigma(\omega)\, d\omega,$$

which - accounting for the factor of 2 differences in $\sigma_B(\omega)$ and $\sigma(\omega)$ - leads to $\sigma_0^B = \sigma_0^H$. Additionally, as will be explained in future sections, the Doppler spectrum is usually normalised before it is inverted and hence the scale factor of 2 becomes irrelevant anyway.

The derived monostatic radar cross section expression in equations 2.122 and 2.123 also differs to that of Johnstone [50]. In this work, like Barrick [5], the coupling coefficients are combined as

$$\left|\Gamma_E^{(M)} - i\Gamma_H\right|^2,$$

however Johnstone combines them as

$$\left(\Gamma_E^{(M)}\right)^2 + 4\Gamma_H^2.$$

This is due to the difference in how the second order scattering processes were combined in the derivations. The second order electromagnetic and hydrodynamic scattering processes include the same two sets of ocean wavetrains, at the same time and place. Therefore, in this work, like that of Barrick, they were combined coherently and consequently the terms in equations 2.97 and 2.98 contributed to the second order radar cross section. In the work of Johnstone, the processes were combined incoherently which resulted in the differing, incorrect, form.

Summary

In this chapter, the bistatic radar cross section of the ocean surface has been derived and the derived term was shown to uniquely equal the monostatic radar cross section of Barrick [5][7] when $\varphi_{bi} = 0$. In the following chapter, the numerical solution is calculated and the results verified using measured monostatic and bistatic radar data.

Chapter 3

Evaluation and Simulation of the Radar Cross Section

§ 3.1 Introduction

To summarise the key results of Chapter 2, the bistatic radar cross section of the ocean surface is given by

$$\sigma(\omega) = \sigma^{(1)}(\omega) + \sigma^{(2)}(\omega),$$

where

$$\sigma^{(1)}(\omega) = 2^5 \pi k_0^4 \cos^4 \varphi_{bi} \sum_{m_B=\pm 1} S(m_B \mathbf{k_B}) \delta(\omega - m_B \omega_B) \tag{3.1}$$

and

$$\sigma^{(2)}(\omega) = 2^5 \pi k_0^4 \cos^4 \varphi_{bi} \sum_{m_1, m_2=\pm 1} \iint |\Gamma_E - i\Gamma_H|^2 \, S(m_1 \mathbf{k_1}) S(m_2 \mathbf{k_2}) \delta(\omega - m_1\omega_1 - m_2\omega_2) \, dp \, dq, \tag{3.2}$$

in which Γ_E is the electromagnetic coupling coefficient given in equation 2.121 and Γ_H is the hydrodynamic coupling coefficient given in equation 2.61. The Bragg frequency, ω_B, was given in equation 2.90 as

$$\omega_B = \sqrt{2gk_0 \cos \varphi_{bi} \tanh(2k_0 d \cos \varphi_{bi})}. \tag{3.3}$$

Figure 3.1 shows a WERA Doppler spectrum and is a depiction of what equations 3.1 and 3.2 are modelling. The two peaks highlighted by the dashed lines show the first order scatter,

modelled by equation 3.1, and the surrounding, lesser, continuum shows the contribution from second order scatter, modelled by equation 3.2.

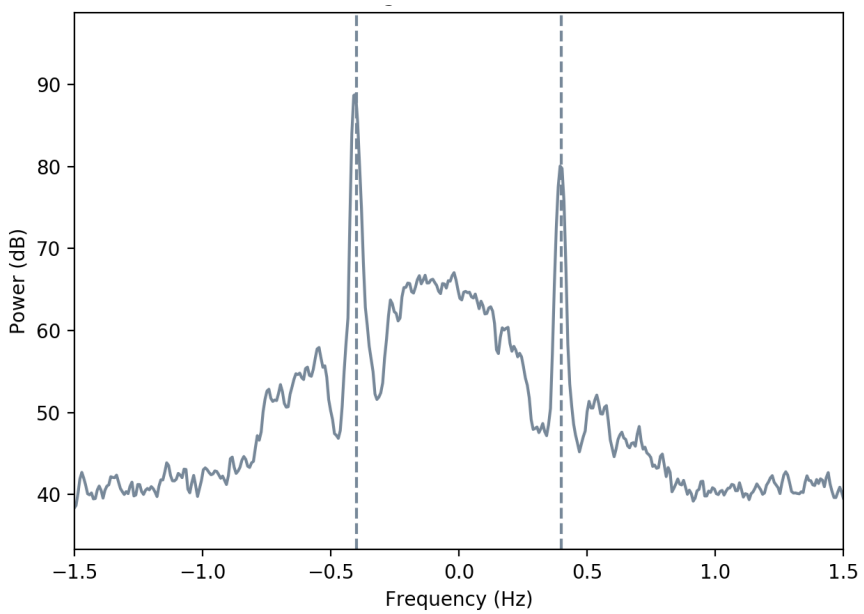

Figure 3.1: Example of a radar Doppler spectrum from the bistatic WERA dataset, described in section 3.2, measured on 12/07/2014 03:21. The spectrum shown is for a bistatic range of 22.18 km and a beam angle of 190° from the receiver (as measured clockwise from north) and hence $\varphi_{bi} \approx 18.6°$. The dashed lines highlight the first order scatter modelled in equation 3.1.

In this chapter, the forward problem will be solved numerically, with a method analogous to the numerical solution of the monostatic radar cross section presented by Holden and Wyatt [43]. That is, for some ocean spectrum, $S(\mathbf{k})$, the corresponding Doppler spectrum, $\sigma(\omega)$, will be calculated, using equations 3.1 and 3.2.

The datasets used in the chapter are described in section 3.2. The numerical details are given in section 3.3, however, when the resulting simulated Doppler spectra are compared to real spectra, substantial differences occur for large values of φ_{bi}. In an attempt to reduce the differences, a more sophisticated simulation method is proposed in section 3.4.

§ 3.2 Datasets

3.2.1 Bistatic WERA Data

To validate the Doppler spectra simulations, a bistatic HF radar dataset has been acquired. The radar site which recorded the data is shown in figure 3.2. The site consists of two WERA systems, maintained by the Mediterranean Institute of Oceanography, who provide

real-time sea surface current monitoring [68]. Situated on the south coast of France, the transmitter is located at (42.98°N, 6.20°E) with a transmission frequency of approximately 16.127 MHz and a bandwidth of 50 kHz. The receiver is located 17.36 km away from the transmitter at (43.09°N, 6.36°E), at Cap Bénat. The receiver comprises 8 vertical electric monopoles with 0.45 EM spacing, placed about 400 m away from shore, at an altitude of 165 m. Boresight is at 200°, measured clockwise from north, and the received time series each consist of 4096 samples with a sample rate of 0.26 seconds. In this work, the time series are processed using a beamforming method, using a Taylor window over the antennas, and a 75% overlapping Nuttall window of size 512 for the Fourier transform. These windows were chosen based on simulated tests, where signals from different direction were simulated and combined appropriately at identically setup antennas; different window combinations were then tested using a phase shift beamforming method, where the windows which recovered a signal from a particular direction the best, were chosen. Additionally, the radar has a range resolution of 3 km and data for 64 ranges are available.

The dataset consists of 280 Doppler spectra, one every 20 minutes, from 00:01, for the dates 09/07/2014, 10/07/2014, 12/07/2014 and 13/07/2014. This dataset will henceforth be referred to as the *bistatic WERA dataset*.

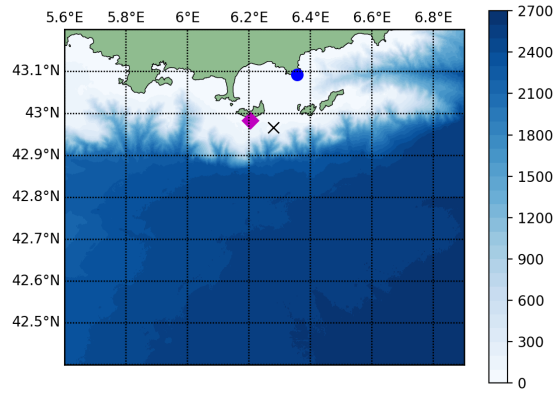

Figure 3.2: Geometry of the bistatic WERA data radar setup on the south coast of France; the transmitter and receiver are shown by the pink diamond and blue circle respectively and, the location of the wave buoy is shown by the black cross. The depth of the Mediterranean sea from the EMODnet database [23] is shown by colour, in metres.

3.2.2 Directional Wave Buoy Data

A directional wave buoy situated in the radar coverage area (6.28°E, 42.97°N), where the ocean depth is 95 m, is used to validate simulated Doppler spectra in this chapter and, to simulate Doppler spectra and validate inversion results in Chapter 5. In both cases, the data

is linearly interpolated when necessary. The Waverider buoy is situated at a bistatic range of 10.9 km with a bearing of 204° from the receiver. Spectra estimated from the buoy data, provided by CANDHIS [73], are in 30 minute intervals for the same time period as the bistatic HF radar data. The specifications of the dataset are given in table 5.2.

Dates	09-10/07/2014 and 12-13/07/2014
Time resolution	30 minutes
Frequency resolution	non linear spacing in [0.025-0.5 Hz] (40 measurements)
Directional resolution	0.087 rads in [0-2π] (72 measurements)

Table 3.1: Specifications of the CANDHIS wave buoy dataset.

3.2.3 Simulation Data

In section 3.4, Doppler spectra are simulated using the local conditions for the bistatic WERA data radar site. As it will be shown in section 3.3, ocean depth, the ocean current and the directional spectrum are all necessary to produce an accurate Doppler spectrum and each has been obtained from a different source.

- Ocean depth data from EMODnet [23] has been used, which has a resolution of approximately 115 m. A contour plot of the data, for the relevant area, is shown in figure 3.2.

- Local current data has been obtained from the Globcurrent database [28], with a temporal resolution of 6 hours and a spatial resolution of 1/8 degree.

- The directional ocean spectra have been modelled using WW3 data from the IOWAGA database [49], input into a Pierson Moskowitz model. The dataset provides values for significant waveheight, peak period, wave spread and wave direction, on a grid with a resolution of $\sim$3.5 km. Data is available with a 3 hour resolution, for the same dates as the bistatic radar data, although the entire dataset spans a larger period of time (2013-2016 are used in Chapter 5).

All three datasets have been linearly interpolated, where necessary.

§ 3.3 Numerical Solution of the Radar Cross Section

3.3.1 First Order

The delta function in equation 3.1 shows that the first order contribution will appear as two peaks, localised at $\pm\omega_B$. The contributing wave vectors are $\pm\mathbf{k_B}$, where

$$\mathbf{k_B} = -2k_0 \cos\varphi_{bi}(\cos\varphi_{bi}, -\sin\varphi_{bi}),$$

for the bistatic angle, φ_{bi}, as shown in figure 2.3. These wavevectors travel in the direction of the Bragg bearing, both toward and away from the radar set-up, also shown in figure 2.3. Furthermore, the magnitude of $\mathbf{k_B}$, k_B, is $2k_0 \cos\varphi_{bi}$. Recalling Crombie's hypothesis [19], discussed in Chapter 1, these particular signals are amplified due to resonance by a process known as *Bragg scattering*. Unlike the monostatic expression, k_B includes a factor of $\cos\varphi_{bi}$; this means that for one radar, using a single carrier frequency, there will be a number of different Bragg waves, dependent on the radar beam range and angle. Figure 3.3 shows the value of φ_{bi} for the bistatic WERA data radar coverage area. The area where $\varphi_{bi} \to 90°$, is known as the *forward scatter* region and for these values of φ_{bi}, both ω_B and k_B tend to 0. Consequently, the wavelengths of the Bragg waves in this region become infinitely long, which is unrealistic. Furthermore, the $\cos^4\varphi_{bi}$ factors in the radar cross section expressions in equations 3.1 and 3.2 will tend to zero, causing a low SNR.

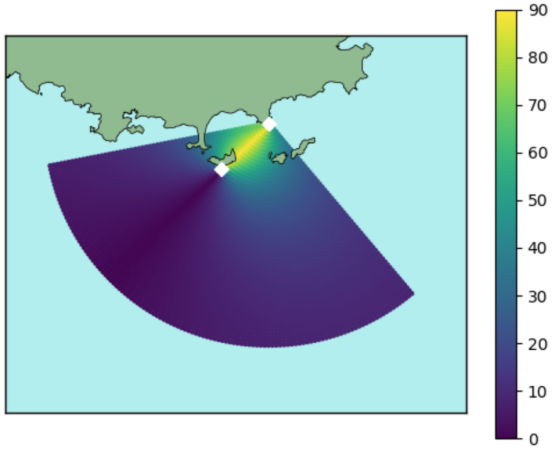

Figure 3.3: Values of the bistatic angle, φ_{bi}, shown by colour for the bistatic WERA data radar setup.

As can be seen in figures 3.1 and 3.4, the peaks are not ideal delta functions, appearing exactly at the Bragg frequency, they are broadened. This is due to ocean current variations and general system noise. Furthermore, specifically for bistatic systems at a scattering location

where φ_{bi} can be large, additional first order peak broadening can occur. This can happen for a radar with a wide main lobe and low range resolution as, in one measurement location, the Bragg frequency can vary substantially. The variation then causes a number of Bragg peaks to occur, which combine to form one broad peak. An example of this, for a measured spectrum, is shown in figure 3.4, where the broadened Bragg peaks are evident. A similar effect can also occur from prominent sidelobes and a large current as was shown, in the monostatic case, by Wyatt *et al.* [109].

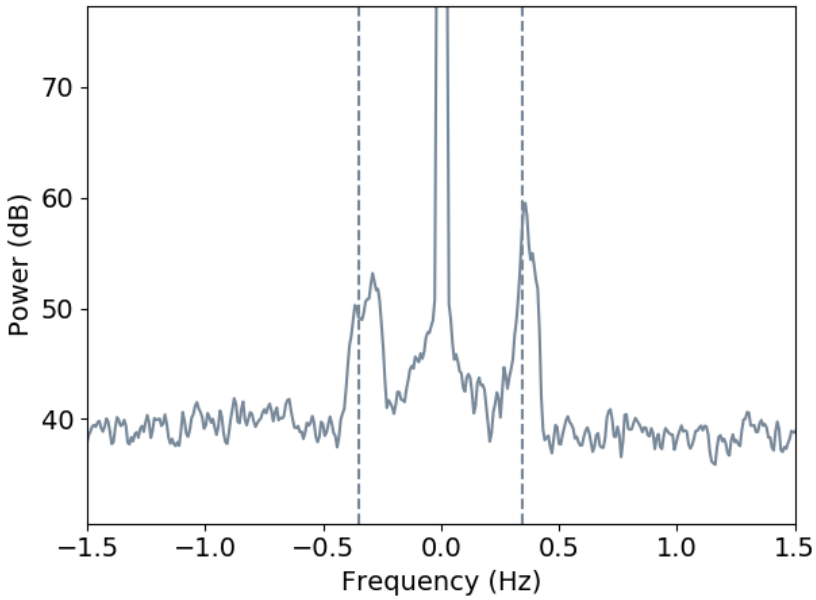

Figure 3.4: A radar Doppler spectrum from the bistatic WERA dataset, described in section 3.2, measured on 09/07/2014 01:01. The bistatic range is 11.7 km and the beam angle is 200°, measured clockwise from north. At this location, $\varphi_{bi} \approx 44°$. The dashed lines show the values of $\pm\omega_B$.

3.3.2 Second Order

The second order contribution, given in equation 3.2, is produced by the nonlinear interaction between two first order ocean waves and by double electromagnetic scattering from two first order ocean waves. The contributing wave vector pair $\mathbf{k_1}$ and $\mathbf{k_2}$ sum to give the Bragg wavevector $\mathbf{k_B}$ and an infinite number of pairs (theoretically) exist in the p,q wavenumber plane; an example pair of such wavevectors are shown in figure 3.5. To find the values of $\mathbf{k_1}$ and $\mathbf{k_2}$, the delta function in equation 3.2, namely,

$$\delta\left(\omega - m_1\sqrt{gk_1\tanh(k_1 d)} - m_2\sqrt{gk_2\tanh(k_2 d)}\right), \tag{3.4}$$

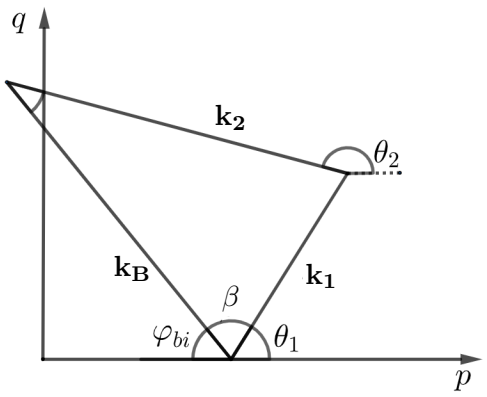

Figure 3.5: Geometry of second order scattering in the wave vector plane, spanned by p and q, where the emitted radar beam is in the direction of the p axis. The wave vector pair $\mathbf{k_1}$ and $\mathbf{k_2}$, at angles θ_1 and θ_2, respectively, as measured from the p axis, are shown, along with the bistatic angle, φ_{bi}, and Bragg wave vector, $\mathbf{k_B}$.

is used, by finding the values for which

$$\omega - m_1\sqrt{gk_1\tanh(k_1d)} - m_2\sqrt{gk_2\tanh(k_2d)} = 0 \tag{3.5}$$

is satisfied. For a given value of ω, the set of solutions of $\mathbf{k_1}$ and $\mathbf{k_2}$ defines a frequency contour in the p,q-plane. As m_1 and m_2 can both take the values of 1 or -1, equation 3.5 can take on four different forms, however it is only necessary to investigate the cases $m_1 = m_2$ and $m_1 \neq m_2$ to understand all four.

3.3.2.1 Case $m_1 = m_2$:

Squaring equation 3.5 gives

$$\omega^2 = g\left(k_1\tanh(k_1d) + k_2\tanh(k_2d) + 2\sqrt{k_1\tanh(k_1d)k_2\tanh(k_2d)}\right)$$

and it can be shown that

$$\omega^2 \geq (k_1 + k_2)g\tanh((k_1 + k_2)d).$$

As the sum of two sides of a triangle is greater than the third (figure 3.5),

$$k_1 + k_2 > 2k_0\cos\varphi_{bi}$$

and therefore

$$\omega^2 > 2gk_0 \cos\varphi_{bi} \tanh(2k_0 \cos\varphi_{bi} d).$$

Taking the square root gives

$$|\omega| > \sqrt{2gk_0 \cos\varphi_{bi} \tanh(2k_0 \cos\varphi_{bi} d)},$$

recognisable as the Bragg frequency, ω_B, given in equation 3.3. This leads to two conditions;

$$\begin{cases} \omega > \omega_B & m_1 = m_2 = 1 \\ \omega \leq -\omega_B & m_1 = m_2 = -1. \end{cases}$$

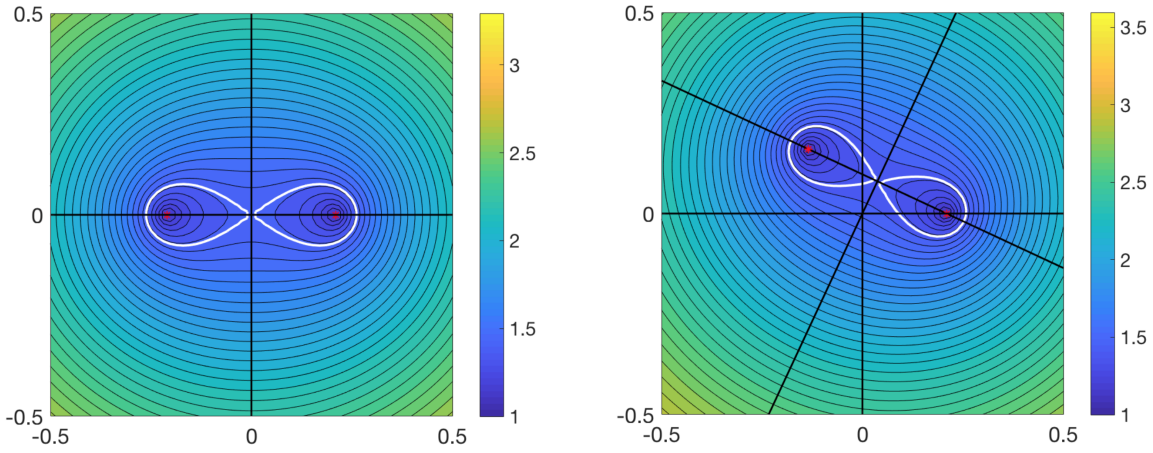

(a) $\varphi_{bi} = 0°$ (b) $\varphi_{bi} = 25°$

Figure 3.6: The frequency contours of equation 3.5 shown for $m_1 = m_2 = 1$ and two values for φ_{bi}. The colour shows the value of the normalised frequency, $\eta = \omega/\omega_B$, for a range of p and q values. The two red stars show the values of $\pm k_0 \cos\varphi_{bi}$ and the white contour shows the value of $\eta = \dfrac{1}{\omega_B} 2\sqrt{gk_0 \cos\varphi_{bi} \tanh(k_0 d \cos\varphi_{bi})}$.

Figure 3.6 shows the frequency contours, defined by equation 3.5, for two different values of φ_{bi}. Close to the Bragg frequencies (i.e. where normalised frequency $\eta = 1$), the contours are circular in shape and centred around the values of $\pm k_0 \cos\varphi_{bi}$. As η increases, the contours become more oval in shape until $|\eta| = \dfrac{1}{\omega_B} 2\sqrt{gk_0 \cos\varphi_{bi} \tanh(k_0 d \cos\varphi_{bi})}$ (shown in white) where they separate.

A non-zero value of φ_{bi} causes the contours to rotate clockwise from being symmetrical about the p and q axes to being symmetrical about some axes, say p' and q'. The additional black lines in figure 3.6 (b) show the p' and q' axes.

3.3.2.2 Case $m_1 \neq m_2$:

When $m_1 \neq m_2$, squaring equation 3.5 gives

$$\omega^2 = g\left(k_1 \tanh(k_1 d) + k_2 \tanh(k_2 d) - 2\sqrt{k_1 \tanh(k_1 d) k_2 \tanh(k_2 d)}\right),$$

and it can be shown that

$$\omega^2 \leq (k_2 - k_1) g \tanh((k_2 - k_1) d).$$

In the right hand plane, when $\mathbf{k_1}$ and $\mathbf{k_2}$ lie in opposite directions along the p' axis, meeting at a point past the Bragg frequency, $k_2 - k_1$ reaches its maximum value of $2k_0 \cos\varphi_{bi}$. Therefore,

$$\omega^2 \leq g(2k_0 \cos\varphi_{bi} \tanh(2k_0 \cos\varphi_{bi} d))$$

and this leads to the conditions

$$\begin{cases} 0 < \omega \leq \omega_B & m_1 = -1, m_2 = 1 \\ -\omega_B < \omega \leq 0 & m_1 = 1, m_2 = -1. \end{cases}$$

In the left hand plane, where $k_2 < k_1$, the result is reversed giving

$$\begin{cases} 0 < \omega \leq \omega_B & m_1 = 1, m_2 = -1 \\ -\omega_B < \omega \leq 0 & m_1 = -1, m_2 = 1. \end{cases}$$

Figure 3.7 shows the normalised frequency contours when $m_1 \neq m_2$ for cases of $\varphi_{bi} = 0°$ and $\varphi_{bi} = 25°$. Again, the contours are symmetrical about the p' and q' axes. However, in this case, they do not cross the q' axis for any value of ω. The contours are tight circles around the Bragg frequencies, growing in size and becoming less circular as the frequency approaches zero.

The frequency contours for all four possible combinations of m_1 and m_2 are symmetrical about the q' axis. Therefore, the integration in equation 3.2 can be taken over one half of the symmetric plane and doubled. Thus, taking the integration of equation 3.2 over the right hand p'-plane, gives

$$\sigma_2(\omega) = 2^6 \pi k_0^4 \cos^4\varphi_{bi} \sum_{m_1, m_2 = \pm 1} \int_{-\infty}^{\infty} \int_{q'}^{\infty} |\Gamma_E - i\Gamma_H|^2 S(m_1 \mathbf{k_1}) S(m_2 \mathbf{k_2}) \, \delta(\omega - m_1\omega_1 - m_2\omega_2) \, dp \, dq. \tag{3.6}$$

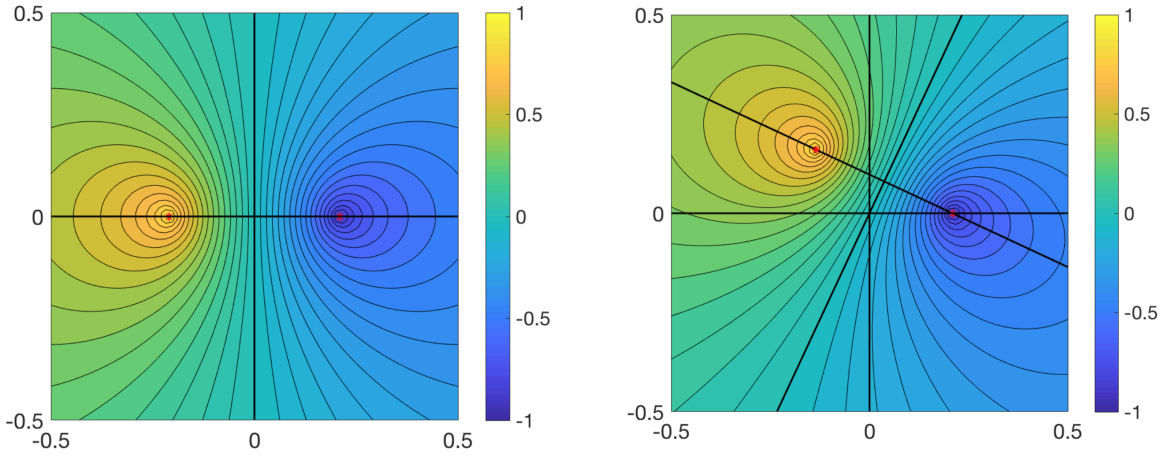

(a) $\varphi_{bi} = 0°$ (b) $\varphi_{bi} = 25°$

Figure 3.7: The frequency contours of equation 3.5 shown for $m_1 \neq m_2$ (where $m_1 = 1$) for two different values for φ_{bi}. The colour shows the value of the normalised frequency, $\eta = \omega/\omega_B$, for a range of p and q values.

In this plane, where $k_1 \leq k_2$, the integration can be carried out in terms of polar coordinates k_1 and θ_1, where θ_1 is the angle between $\mathbf{k_1}$ and the p axis (see figure 3.5). Explicitly,

$$\sigma_2(\omega) = 2^6 \pi k_0^4 \cos^4 \varphi_{bi} \sum_{m_1,m_2=\pm 1} \int_{-\theta_L^-}^{\theta_L^+} \int_0^\infty |\Gamma_E - i\Gamma_H|^2 S(m_1\mathbf{k_1}) S(m_2\mathbf{k_2}) \\ \delta(\omega - m_1\omega_1 - m_2\omega_2) k_1 \, dk_1 \, d\theta_1, \tag{3.7}$$

where θ_L^- and θ_L^+ are the integration limits of θ_1 and vary with frequency.

3.3.2.3 Integration Limits

The general integration limits vary with φ_{bi} such that

$$\theta_L^- = -(\pi + \varphi_{bi}) \quad \text{and} \quad \theta_L^+ = \pi - \varphi_{bi}. \tag{3.8}$$

However, a particular set of ω values requires different limits. It was stated in the discussion of frequency contours that when $m_1 = m_2$ and $|\omega| > 2\sqrt{k_0 g \cos\varphi_{bi} \tanh(k_0 d \cos\varphi_{bi})}$, the frequency contours cross the q' axis and no longer complete full rotations in the right half of the p'-plane. By symmetry, when the contours cross the q' axis, k_1 and k_2 are the same length. Therefore, when $k_2 = k_1$ and $m_1 = m_2$, the delta constraint of equation 3.5 becomes,

$$\omega = \pm 2\sqrt{g k_1 \tanh(k_1 d)} \tag{3.9}$$

and squaring equation 3.9 then gives

$$\frac{\omega^2}{4g} = k_1 \tanh(k_1 d), \tag{3.10}$$

which can be solved numerically for k_1. Introducing a term, β, as the angle between $\mathbf{k_1}$ and $\mathbf{k_B}$ (see figure 3.5), the integration limits are given by

$$\theta_L^+ = \pi - \varphi_{bi} - \beta, \tag{3.11}$$

and

$$\theta_L^- = -\theta_L^+ - 2\varphi_{bi}. \tag{3.12}$$

Therefore, as

$$\beta = \cos^{-1}\left(\frac{k_B}{2k_1}\right), \tag{3.13}$$

where the solution for k_1 from equation 3.10 is used,

$$\theta_L^+ = \pi - \varphi_{bi} - \cos^{-1}\left(\frac{k_B}{2k_1}\right) \tag{3.14}$$

and

$$\theta_L^- = -\pi - \varphi_{bi} + \cos^{-1}\left(\frac{k_B}{2k_1}\right).$$

3.3.2.4 Integration Variables

As the integration variables are k_1 and θ_1, k_2 and θ_2 must be expressed in terms of k_1 and θ_1. By the cosine rule,

$$k_2 = \sqrt{k_1^2 + k_B^2 + 2k_B k_1 \cos(\theta_1 + \varphi_{bi})} \tag{3.15}$$

and, again by the cosine rule whilst using the result from equation 3.15,

$$\theta_2 = \pi + \theta_1 - \cos^{-1}\left(\frac{k_1 + k_B \cos(\theta_1 + \varphi_{bi})}{k_2}\right). \tag{3.16}$$

3.3.2.5 Reducing the Integral

The next step in calculating $\sigma^{(2)}(\omega)$ is to reduce the double integral in equation 3.7 to a single integral using the delta function integration property,

$$\int f(x)\delta(x-a)\,dx = f(a).$$

To do this, define

$$y_s = \sqrt{k_1},$$

$$h(y_s,\theta_1) = m_1 y_s\sqrt{g\tanh(y_s^2 d)} + m_2\sqrt{gk_2\tanh(k_2 d)} \tag{3.17}$$

and

$$I(y_s,\theta_1) = 2^7\pi|\Gamma_E - i\Gamma_H|^2 k_0^4\cos^4\varphi_{bi}S(m_1\mathbf{k_1})S(m_2\mathbf{k_2})y_s^3.$$

which can be used to write equation 3.7 as

$$\sigma_2(\omega) = \int_{-\theta_L^-}^{\theta_L^+}\int_0^\infty I(y_s,\theta_1)\delta\left(\omega - h(y_s,\theta_1)\right)\,dy_s\,d\theta_1. \tag{3.18}$$

In order for the delta function integration property to be valid, equation 3.18 should have an integration variable of h. Therefore, y_s is transformed into h to give

$$\sigma_2(\omega) = \int_{-\theta_L^-}^{\theta_L^+}\int_0^\infty I(y_s,\theta_1)\delta\left(\omega - h(y_s,\theta_1)\right)\left|\frac{\partial y_s}{\partial h}\right|_{\theta_1} dh\,d\theta_1, \tag{3.19}$$

where

$$\left|\frac{\partial h}{\partial y_s}\right|_{\theta_1} = \sqrt{g}\left\{m_1\left(\sqrt{\tanh(y_s^2 d)} + \frac{y_s^2 d(\mathrm{sech}^2(y_s^2 d))}{\sqrt{\tanh(y_s^2 d)}}\right)\right.$$
$$\left. + \frac{m_2(y_s^3 + y_s k_B\cos(\theta_1+\varphi_{bi}))}{k_2^{3/2}}\left\{\sqrt{\tanh(k_2 d)} + k_2 d\frac{\mathrm{sech}^2(k_2 d)}{\sqrt{\tanh(k_2 d)}}\right\}\right\},$$

whose reciprocal is $\left|\frac{\partial y_s}{\partial h}\right|_{\theta_1}$ and where $k_2 = \sqrt{y_s^4 + 2y_s^2 k_B\cos(\theta_1+\varphi_{bi}) + k_B^2}$.

To simplify the double integral in equation 3.19 to a single integral, the solution, y^*, to

$$\omega - h(y^*,\theta_1) = 0 \tag{3.20}$$

is required, which can be sought using a numerical method. For timely convergence in the numerical method, a good initial guess for y^* is important. As the solution for shallow water should not be too different to that for deep water, an initial solution will be found for the deep water case and used as a starting point for the shallow water case. Labelling the expression to be solved for zero as $f(y)$, and substituting equation 3.17 into 3.20,

$$f(y) = \omega - \left(m_1 y \sqrt{g \tanh(y^2 d)} + m_2 \left\{ \left(y^4 + 2y^2 k_B \cos(\theta_1 + \varphi_{bi}) + k_B^2 \right)^{1/4} \cdot \sqrt{g \tanh\left(\left(y^4 + 2y^2 k_B \cos(\theta_1 + \varphi_{bi}) + k_B^2 \right)^{1/2} d \right)} \right\} \right), \tag{3.21}$$

and by letting $d \to \infty$, equation 3.21 becomes

$$f(y) = \omega m_1 - y\sqrt{g} - L\sqrt{g} \left(y^4 + 2y^2 k_B \cos(\theta_1 + \varphi_{bi}) + k_B^2 \right)^{1/4}, \tag{3.22}$$

where $L = m_1 m_2$ has been used. Equation 3.22 can be solved exactly in two cases:

- $L = 1$ and $\theta_1 = -\varphi_{bi}$:

  In this case, $f(y)$ becomes

  $$f(y) = m_1\omega - y\sqrt{g} - \sqrt{g} \left(y^4 + 2k_B y^2 + k_B^2 \right)^{1/4} = 0,$$

  which can be rearranged to

  $$(m_1\omega - y\sqrt{g})^4 = g^2 \left(k_B + y^2 \right)^2$$

  and this can then be solved to give

  $$y_0^* = \frac{\omega^2 - g k_B}{2 m_1 \omega \sqrt{g}}. \tag{3.23}$$

- $L = -1$ and $\theta_1 = \pi - \varphi_{bi}$:

  In this case, $f(y)$ becomes

  $$f(y) = m_1\omega - y\sqrt{g} + \sqrt{g} \left(y^4 - 2k_B y^2 + k_B^2 \right)^{1/4} = 0.$$

  This can be written as

  $$(m_1\omega - y\sqrt{g})^4 = g^2 \left(k_B - y^2 \right)^2$$

and then taking the square root, noting that the $\left(k_B - y^2\right)$ root is taken on the right hand side to ensure it's positive, gives

$$(m_1\omega - y\sqrt{g})^2 = g(k_B - y^2).$$

The solution is then found to be

$$y_0^* = \frac{m_1\omega + \sqrt{2gk_B - \omega^2}}{2\sqrt{g}}, \tag{3.24}$$

where the positive root has again been taken to ensure y_0^* is positive.

3.3.2.6 Calculating the Single Integral

Upon finding y^*, the second order cross section calculation in equation 3.19 reduces to

$$\sigma_2(\omega) = \int_{-\theta_L^-}^{\theta_L^+} I(y_s, \theta_1) \left| \frac{\partial y_s}{\partial h} \right|_{\theta_1} \Bigg|_{y_s = y^*} d\theta_1, \tag{3.25}$$

which can be calculated using a numerical integration method such as the Trapezoid/Simpson's rule. To ensure convergence and to speed up the simulation, the value of y_0^* is updated to the previous y^* value for increasing θ_1. Additionally, in order to compute the integral, there are expressions in the coupling coefficient that need to be expressed in terms of k_1 and θ_1:

- $\mathbf{k_1} \cdot \hat{\mathbf{a}} = -k_1 \cos(2\varphi_{bi} + \theta_1)$,
- $\mathbf{k_2} \cdot \hat{\mathbf{a}} = k_B \cos\varphi_{bi} + k_1 \cos(2\varphi_{bi} + \theta_1)$ and
- $\mathbf{k_1} \cdot \mathbf{k_2} = -k_1 k_B \cos(\theta_1 + \varphi_{bi}) - k_1^2$.

3.3.2.7 Electromagnetic Singularities

The electromagnetic coupling coefficient given in equation 2.121, contains two singularities; either when b_1 or b_2 is equal to zero. As

$$b_1 = b(p, q) = \sqrt{k_0^2 - p^2 - q^2}$$

and

$$b_2 = b(k_0\cos\varphi - p + k_0, k_0\sin\varphi - q) = \sqrt{k_0^2 - (k_0\cos\varphi - p + k_0)^2 - (k_0\sin\varphi - q)^2},$$

setting both equal to zero, squaring and rearranging reveals that the singularities lie on two circles in the p,q-plane, namely

$$p^2 + q^2 = k_0^2 \tag{3.26}$$

and

$$(k_0 \cos\varphi - p + k_0)^2 + (k_0 \sin\varphi - q)^2 = k_0^2. \tag{3.27}$$

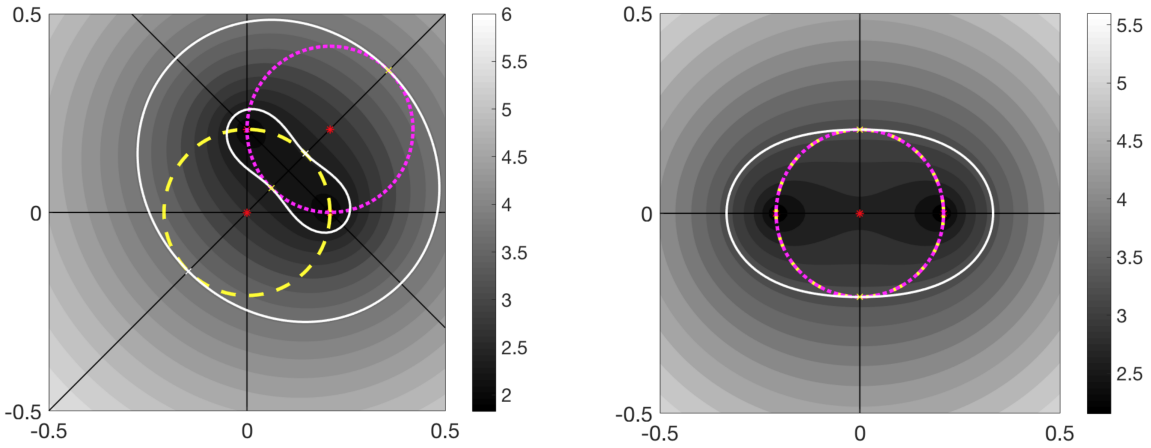

(a) Bistatic ($\varphi_{bi} = 45°$)

(b) Monostatic ($\varphi_{bi} = 0°$)

Figure 3.8: Contours in the p,q-plane defined by equation 3.5 when $m_1 = m_2 = 1$. The electromagnetic singularities are shown for both monostatic and bistatic radars. The yellow dashed circle shows the singularities defined by equation 3.26 and the magenta dotted circle shows those defined by equation 3.27. In the monostatic case, equations 3.26 and 3.27 are equal and hence both circles are in the same location. The frequency contours that are tangential with the singularities are shown in white.

Both singularities are shown in figure 3.8(a), and each singularity will be most prominent when a frequency contour is tangential to the singular circle. In order to find the frequencies for which this is true, we seek the solutions for p and q such that the gradient of the frequency contour expression of equation 3.5 is equal to the gradient of each circle function in equations 3.26 and 3.27. Knowledge of the geometry of the contours and the radii of the circles is exploited to find the solutions for p and q and then the solutions are substituted into equation 3.5 to give the tangential frequencies. The four solutions for p and q are

$$p = k_0 \sin\varphi_{bi} \text{ and } q = k_0 \cos\varphi_{bi}, \tag{3.28}$$

$$p = -k_0 \sin\varphi_{bi} \text{ and } q = -k_0 \cos\varphi_{bi}, \tag{3.29}$$

$$p = k_0 \sin\varphi_{bi} + 2k_0 \sin^2\varphi_{bi} \text{ and } q = k_0 \cos\varphi_{bi} + 2k_0 \sin\varphi_{bi}\cos\varphi_{bi} \tag{3.30}$$

and

$$p = -k_0 \sin\varphi_{bi} + 2k_0 \sin^2\varphi_{bi} \text{ and } q = -k_0 \cos\varphi_{bi} + 2k_0 \sin\varphi_{bi}\cos\varphi_{bi} \tag{3.31}$$

and each solution can be readily verified by substitution into the relevant derivative functions. Substituting the solutions for p and q, from equations 3.28-3.31 into equation 3.5 gives two distinct tangential frequencies: one for the solutions of p and q in equations 3.28 and 3.29,

$$\omega = 2^{3/4}\omega_B \sqrt{\frac{\sqrt{1-\sin\varphi_{bi}}}{\cos\varphi_{bi}}} \frac{\sqrt{\tanh(d\sqrt{2k_0^2(1-\sin\varphi_{bi})})}}{\sqrt{\tanh(2k_0\cos\varphi_{bi}d)}} \tag{3.32}$$

and one for the solutions of p and q in equations 3.30 and 3.31,

$$\omega = 2^{3/4}\omega_B \sqrt{\frac{\sqrt{1+\sin\varphi_{bi}}}{\cos\varphi_{bi}}} \frac{\sqrt{\tanh(d\sqrt{2k_0^2(1+\sin\varphi_{bi})})}}{\sqrt{\tanh(2k_0\cos\varphi_{bi}d)}}. \tag{3.33}$$

These values for ω are highlighted in figure 3.6 by the white contours and are shown to be tangential to the circles expressed in equations 3.26 and 3.27. Both sigularities are highlighted in a simulated Doppler spectrum in figure 3.9 by dashed vertical lines. For deep water, or when $d \to \infty$, the values for ω become

$$\omega = 2^{3/4}\omega_B \sqrt{\frac{\sqrt{1 \pm \sin\varphi_{bi}}}{\cos\varphi_{bi}}}, \tag{3.34}$$

which agree with the results of Gill and Walsh [27].

Setting $\varphi_{bi} = 0$ in equation 3.34 gives the monostatic electromagnetic singularity, namely

$$\omega = 2^{3/4}\omega_B^{(M)},$$

which is shown in figure 3.8(b), noting that $\omega_B^{(M)}$ in the monostatic Bragg frequency defined in section 2.6. In terms of $\mathbf{k_1}$ and $\mathbf{k_2}$, the singularity occurs when

$$b(p,q) = \sqrt{\mathbf{k_1} \cdot \mathbf{k_2}}$$

and hence is due to a *corner reflector*, as $\mathbf{k_1}$ is perpendicular to $\mathbf{k_2}$.

3.3.3 Ocean Currents

An ocean current can affect how an ocean wave propagates, both in direction and speed. The angular frequency, ω, of an ocean wave was given in equation 1.15; it is known as the *relative velocity* and applies if the frame of reference is moving with the current. Holthuijsen [44] likens this to a wave moving as it would but in a tank of water being carried with the speed and direction of the ambient current. However if the frame of reference is fixed, as in the case of an observation of a patch of the ocean from a fixed point, the propagation velocity of the wave with the ambient current included, $\mathbf{c}_{abs}$, is found by adding the current vector, $\mathbf{U}$, to the velocity propagation vector of the wave, $\mathbf{c}_{rel}$, i.e.

$$\mathbf{c}_{abs} = \mathbf{c}_{rel} + \mathbf{U}. \tag{3.35}$$

Therefore, as the current is causing a change in speed to the waves, the Doppler effect causes an additional shift, $\triangle\omega$, to the entire returned spectrum. From equation 1.5, the additional shift is

$$\triangle\omega = 2k_0\nu_E(\varphi)\cos\varphi_{bi}, \tag{3.36}$$

where $\nu_E(\varphi)$ is the component of the current velocity in the elliptical direction for beam angle φ.

To include the current effects in the simulation, the current speed and direction are input and the respective Doppler shift is calculated as per equation 3.36.

3.3.4 Simulation

A Python 3 code has been written to simulate Doppler spectra, following the method in this section. In the code, there are two options for the input values of $S(\mathbf{k})$; either partition values for h_s, t_p, s (for the directional $\cos^{2s}$ model) and θ_m are input and a Pierson Moskowitz spectrum is used to model the values of $S(\mathbf{k})$, or a pre-determined matrix of the values for $S(\mathbf{k})$ can be used, which is linearly interpolated for the calculations. The current speed and direction are also input, as well as general radar information such as the carrier frequency and the distance between the transmitter and receiver. To make the simulation more realistic, the calculated $\sigma(\omega)$ is convolved with a Nuttall window [34] and noise, randomly generated from a Gaussian distribution with a user-defined variance and floor level, is added to emulate the signal processing effects.

An example of a Doppler spectrum, simulated by the program, is shown in figure 3.9. The timing of the simulation varies, depending on the resolution of the integration in both θ_1 and ω, as shown in figure 3.10. A recommended compromise is to simulate a 512 point Doppler spectrum, between -1.27 and 1.27 Hz (a range which encapsulates the important parts of the spectrum with some surrounding noise), with 50 θ_1 points per frequency value; a simulation with these settings takes approximately 0.31 seconds (executed on a machine with an Intel Core i5 processor and 8 GB of RAM).

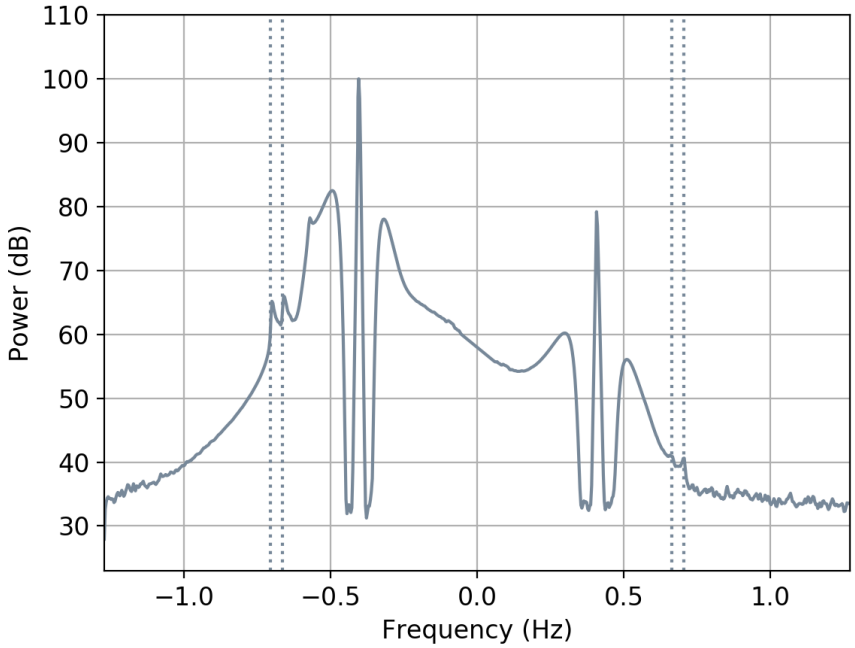

Figure 3.9: A bistatic Doppler spectrum where the Tx and Rx are set 60 km apart, with $\varphi_{bi} \approx 20°$. The directional spectrum $S(\mathbf{k})$ is modelled with $h_s \approx 4$ m, $t_p \approx 10.2$ s with $\theta_m = 170°$, clockwise from north, and $s = 2$. The carrier frequency is set to 16 MHz and in this case no current has been added. The spectrum has been calculated over 768 evenly spaced points between -1.27 Hz and 1.27 Hz and for each frequency, a 500 point integration has been carried out over θ_1. The electromagnetic singularities are highlighted by the dashed lines and a noise floor has also been added.

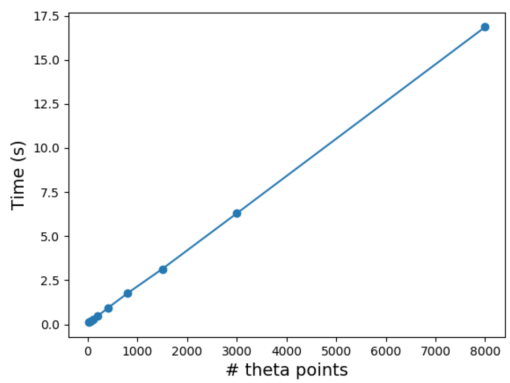

(a) Varying number of θ points in the simulation, with the number of frequency points set to 512.

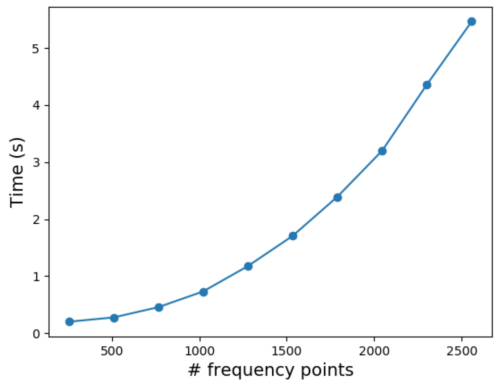

(b) Varying number of frequency points in the simulation, with the number of θ points set to 100.

Figure 3.10: Running time (in seconds) of the simulation code with the labelled parameter varied.

§ 3.4 Simulation Incorporating the Radar Effects

3.4.1 Introduction

Measured HF radar data are now used to check the validity of a spectrum simulated using the method of section 3.3. This can be done in a location where both HF radar and directional wave buoy data are available; the directional wave buoy data (which provides $S(\mathbf{k})$) is used as input to the simulation and the resulting simulated Doppler spectrum is then compared with the measured Doppler spectrum.

To ensure the simulation is correct, a monostatic HF radar data set has been acquired alongside directional wave buoy data in the coverage area. Both datasets are described in detail in section 5.2.1. Figure 3.11 shows both simulated and measured Doppler spectra for an overlapping time and the resulting spectra are very similar.

The simulation was also tested using the bistatic WERA dataset and the directional wave buoy off the south coast of France, described in section 3.2. At the location of the wave buoy, $\varphi_{bi} = 43^\circ$ and the differences between the measured and simulated Doppler spectra are large. An example is given in figure 3.12. In the simulated spectra, the first order peaks are clear and narrow. However, in the measured spectra, the first order peaks are visibly broadened and therefore, as first highlighted by Grosdidier [29], the radar cross section expression is not representative of these Doppler spectra for large φ_{bi}.

When equations 3.1 and 3.2 are not representative of the data, they cannot be reliably used to

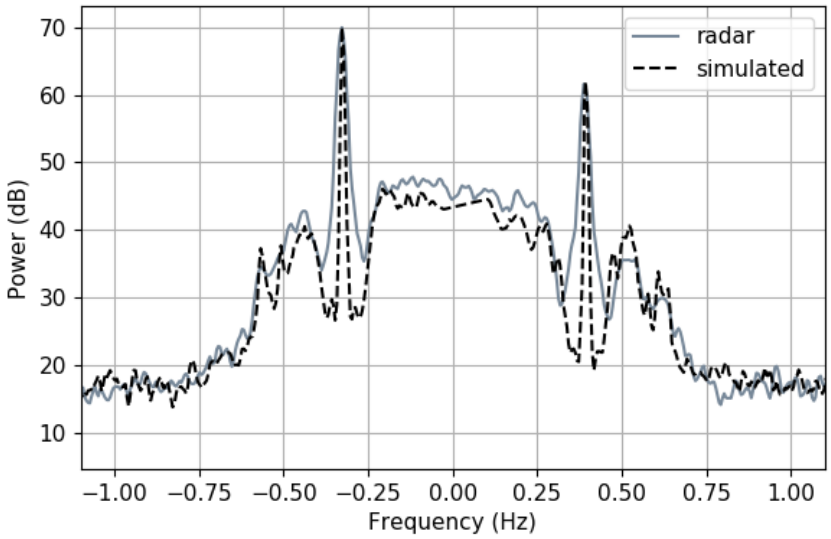

Figure 3.11: Comparison of measured and simulated monostatic Doppler spectra on 01/11/2012 20:05. The figure shows a comparison of a spectrum from the Wave Hub HF dataset at the location of the wave buoy, and a Doppler spectrum simulated using equations 3.1 and 3.2 with $S(\mathbf{k})$ from the wave buoy input.

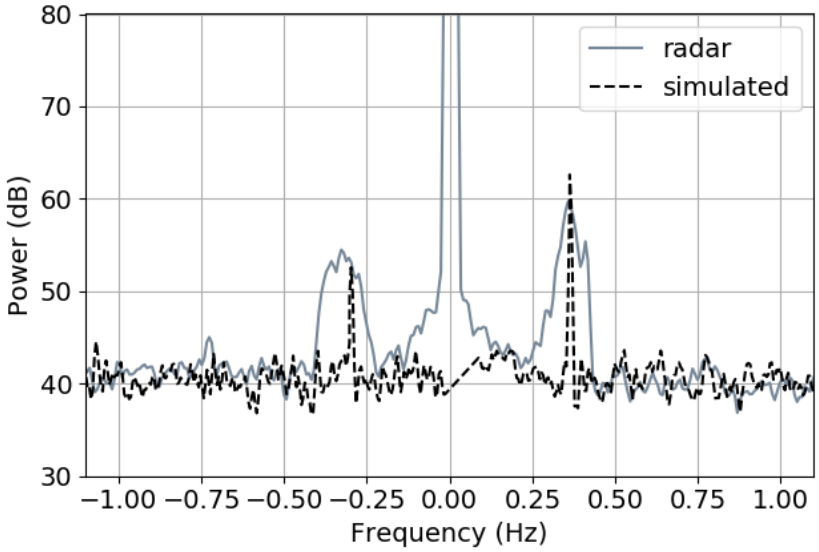

Figure 3.12: Comparison of measured and simulated bistatic Doppler spectra on 09/07/2014 01:00. The figure shows a spectrum from the bistatic WERA dataset at the location of the wave buoy, and a spectrum simulated using the ocean spectrum, $S(\mathbf{k})$, measured by the wave buoy, as input to equations 3.1 and 3.2. At this location, $\varphi_{bi} = 43°$.

invert measured spectra, to obtain $S(\mathbf{k})$. Therefore, as the ultimate aim is to invert measured bistatic Doppler spectra, the equations must be modified so that they represent the data more

accurately.

Grosdidier *et al.* [29] address the problem by including the radar effects in the simulation. In their work, they define the measured radar cross section at a given cell, $\sigma_{\text{exp}}(\omega)$, as

$$\sigma_{\text{exp}}(\omega) = \int_{\text{sea}} \mathcal{G}\sigma(\omega)\, dA$$

where

$$\mathcal{G} = \frac{P_e \lambda_0^2 F_t G_t F_r G_r W}{(4\pi)^3 R_t^2 R_r^2}$$

is the *cell weighting function*, similar to the radar equation in equation 1.14. In the expression, P_e is emitted power, G is gain, F represents path losses, R is is distance, λ_0 is the emitted radiowave wavelength and W is a weighting value of a window convolved with range. A subscript of r refers to the receiver and t, to the transmitter. By including the antenna gains, the beam pattern of the radar in included in the simulation and thus too is the variation in the Bragg frequency with bistatic angle. Their results show an improvement in the simulations and the first order peaks are appropriately broadened.

3.4.2 Methodology

Here, similarly to Grosdidier *et al.* [29], a method is proposed to create more realistic simulated Doppler spectra by including the radar effects. However, instead of a weighted sum of the Doppler spectra in the frequency domain, the individually simulated Doppler spectra are converted to time series and combined in the time domain at the receiving antennas. Then, when a signal is required from a particular angle, the data is beamformed in the same way as the measured radar data. This method has been chosen, instead of that of Grosdidier *et al.*, for two reasons. Firstly, by generating time series at the antennas, there is an opportunity for testing different beamforming methods in the future. Secondly, the size of the final data structure is smaller and from this, a signal from any direction can be obtained by beamforming, unlike the rigidity of a fixed grid.

The method is tested using the radar setup of the bistatic WERA dataset; the results can then be validated by comparing the simulated Doppler spectra against the measured Doppler spectra, described in section 3.2.1. There are a number of islands in the vicinity of the receiver meaning that the radar does not receive scatter from some areas. Therefore, after consulting with Dr. Yves Barbin, who worked on the radar, a map of valid scattering locations has been created, as shown in figure 3.13.

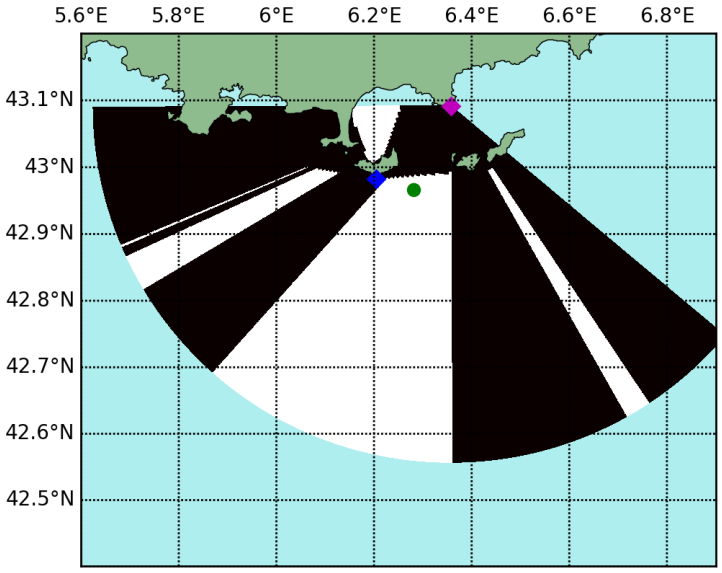

Figure 3.13: Scatter weights for the bistatic WERA radar. White indicates areas of viable scatter and black, not.

With a 1° and 1 km resolution, angles 110° through to 290°, for ranges of 1-39 km, are all considered for contributing to the resulting signal. To begin, each cell is checked against the scattering locations in figure 3.13, then, if the cell is viable, a Doppler spectrum is simulated. In the simulation, current data from the Globcurrent dataset is used to calculate the Doppler shift, alongside WW3 data which is used as input to a Pierson Moskowitz spectrum, with a $\cos^{2s}$ directional model, to model $S(\mathbf{k})$. The bistatic geometry, along with the radar frequency and ocean depth is also input. The simulated spectrum is then multiplied by a weight, which is inversely proportional to its distance to the receiver and to the transmitter, namely

$$\frac{1}{R_R^2 R_T^2}.$$

Once all of the Doppler spectra have been simulated, the set of Doppler spectra for each beam angle is convolved with a Blackman-Harris window to emulate the effects of the signal processing methods used to obtain the range-resolved time series. Then, for each beam, spectra in groups of three (namely for each 3 km) are averaged, to mimic the real data which has a range resolution of 3 km.

Finally, for each range, the simulated Doppler spectra are Fourier transformed into the time domain and then, using the range and angle of the scatter location from the eight receive antennas, the time series are delayed appropriately (in a way analogous to beamforming) to produce eight time series. All of the simulated time series at each antenna are then summed

and an array of eight complex time series for every range is output.

3.4.2.1 Limitations

Although, ideally, the transmitter gain would have been included in the simulation process, we were unable to obtain the information and this has therefore been omitted. Also, following Grosdidier*et al.* [29], the path attenuation factors, F_R and F_T, have also been included as binary values, whereby they equal 0 when an island is encountered and 1 otherwise. Having accurate values for both path loss and antenna gain would improve the simulation further and would be something to consider in future experiments.

Another issue is the speed/resolution tradeoff of the simulation method. Preferably the original spectra would be 4096 point spectra, to mimic the bistatic WERA data with which it is being compared, however, this is infeasible due to calculation time. To counter this, simulations of 676 points from -1.27 to 1.27 Hz (which is a subset of the measured spectra range) have been generated which are then beamformed, before the resulting time series are processed using 75% overlapping windows of size 338. Over this interval, both the measured and simulated spectra comprise 338 points and are directly comparable.

Finally, the resolution of the simulations may not be fine enough. Particularly at long ranges, the spatial difference between 1° will be more significant and information may be missed. However, to increase the resolution means to slow the simulation down. Keeping in mind that the more complex simulation process is more important at shorter ranges, where φ_{bi} is larger, the resolution can be justified.

3.4.3 Results

The simulation method was tested on the dates where overlapping radar and WW3 data was available, namely the 9, 10, 12 and 13 July 2014. The results depend on the accuracy of the WW3 data for the period and also how well a Pierson-Moskowitz spectrum with a cosine directional distribution models the real directional spectrum. For some of the dates tested, there were obvious differences between the actual ocean spectrum and the modelled spectrum, as the ratio of the first order peaks (or the *Bragg ratio*) of the simulated and measured Doppler spectra were substantially different. In such circumstances, where the WW3 model does not accurately represent the ocean state, the simulated Doppler spectrum has not been compared with the measured Doppler spectrum as they will be substantially different.

Figure 3.14 shows the results of the simulation for 12/07/2014 03:21 at two different locations, where the Bragg ratios of the measured and simulated data were in agreement. In each

example, the simulated and measured Doppler spectra have been adjusted to have the same maximum magnitude, for easy comparison; additionally, the spike at zero Doppler, for each measured spectrum, is due to land return which is not simulated in this work. For the chosen time, h_s ranges between 2 and 4 m so it is large enough to generate substantial second order sidebands. Both examples show that the Doppler peaks become broadened, as in the measured data, when the radar effects are included in the simulation.

As was also found by Grosdidier *et al.* [29], the second order contribution to the spectrum did not change much. This does suggest that the existing wave inversion methods could work if they only rely on the second order sidebands. More work must be done to investigate this point, however, the results of Wyatt *et al.* [109] showed that inversion of similar spectra was not possible.

Summary

In this chapter, the numerical solution of the bistatic radar cross section was calculated, enabling one to simulate the expected bistatic radar return for any given ocean spectrum. When validating the theory and simulation, the resulting signal was compared against real bistatic HF radar measurements and large differences occurred, in scattering locations where φ_{bi} substantially varied. In such scenarios, the radar effects cannot be ignored and a method of including them was presented. The method was shown to improve the simulations and the resulting simulated spectra were much more similar to the measured data.

In the next chapter, inversion methods are discussed and proposed, so that we can obtain current, wind and wave measurements from bistatic HF radar data, by using the results of this chapter.

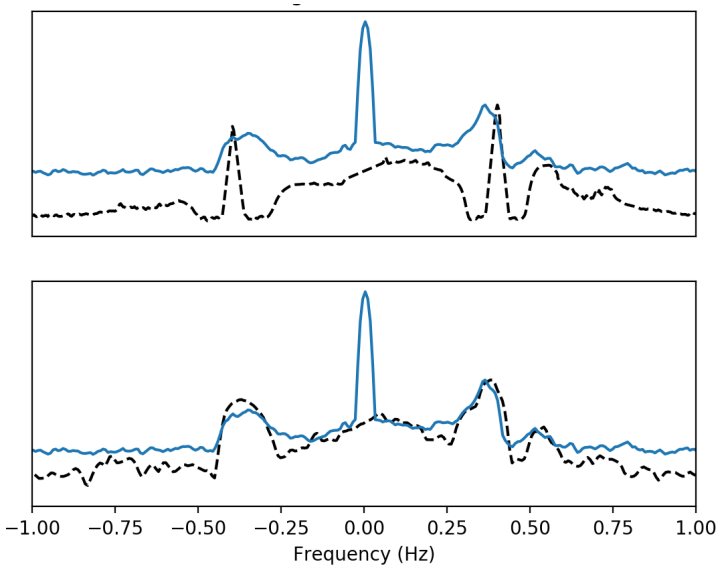

(a) Spectra at a bistatic range of 10.2 km and a bearing of 220°. At this location, $\varphi_{bi} \approx 30°$.

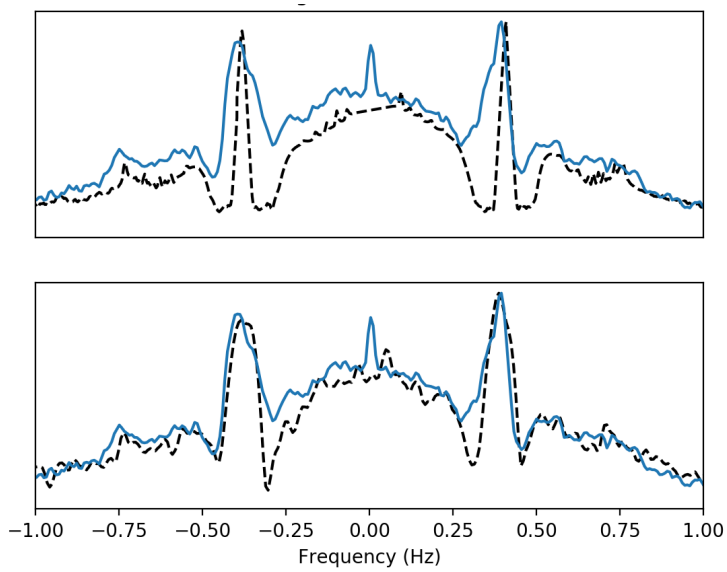

(b) Spectra at a bistatic range of 16.2 km and a bearing of 200°. At this location, $\varphi_{bi} \approx 25°$.

Figure 3.14: Simulated Doppler spectra compared with measured Doppler spectra, from the bistatic WERA data, on 12/07/2014 03:01:00. In both figures (a) and (b), the top plot shows a simulated Doppler spectrum using the 'standard' method of section 3.3 and the bottom plot shows a simulated spectrum using the method outlined in section 3.4.2, where radar effects are included. In each plot, the simulated data are shown by the dashed line and the measured spectrum by the solid line. The y axis shows the power in the spectrum in dB.

Chapter 4

HF Radar Inversion Methods

In Chapter 2, a model for the bistatic radar cross section of the ocean, $\sigma(\omega)$, was derived and then, in Chapter 3, its numerical solution was presented. In other words, a solution to the forward problem was given. In this chapter, methods for solving the inverse problem - for currents, wind directions and waves - are discussed. In section 4.1, methods for retrieving current measurements from bistatic data are described and then in section 4.2, wind direction inversion methods are outlined, with a focus on the maximum likelihood method of Wyatt *et al.* [108]. In section 4.3, an introduction to wave inversion is given before a new method for obtaining the directional ocean spectrum, using a neural network, is proposed. To support the proposal, an introduction to neural networks is given in section **??**, before the details of the neural network inversion method are given in section 4.4.

§ 4.1 Ocean Surface Currents

In 1974, Stewart and Joy [85] showed that near-surface ocean currents displace the first order Bragg peaks from their predicted frequencies. The displacement was shown, in equation 3.36, to be

$$\triangle\omega = 2k_0\nu_E(\varphi)\cos\varphi_{bi}, \tag{4.1}$$

where $\nu_E(\varphi)$ is the component of the current velocity in the normal elliptical direction for a radar beam angle, φ. Therefore, $\nu_E(\varphi)$ can be obtained by calculating

$$\nu_E(\varphi) = \frac{\triangle\omega}{2k_0\cos\varphi_{bi}}. \tag{4.2}$$

For high quality radar data, with high resolution and low sidelobes, identifying the first order peaks necessary to measure the shift, $\triangle\omega$, is straightforward. However, for data with large sidelobes, current shear or low resolution with a varying bistatic angle (as seen in figure 3.12), the first order peaks are broadened and hence it becomes more difficult to identify the appropriate Bragg peaks' positions.

If the peaks can be successfully identified, then the corresponding elliptical component can be calculated using equation 4.2. However, with just one measurement, there is not enough information to compute the total current vector. Usually, to compute this, Doppler spectra measured by at least 2 different radars are used. If one obtains two elliptical components, $\nu_E(\varphi_1)$ and $\nu_E(\varphi_2)$ (for radar beam angles φ_1 and φ_2, measured clockwise from north), then a current, $\boldsymbol{\nu}$, travelling in a direction, θ, can be calculated absolutely. With $u = \nu \sin\theta$ and $v = \nu \cos\theta$, the east and north components of $\boldsymbol{\nu}$, the two radar measurements can be written in terms of u and v by

$$\nu_E(\varphi_1) = v\cos\theta_1 + u\sin\theta_1 \qquad\qquad \nu_E(\varphi_2) = v\cos\theta_2 + u\sin\theta_2, \tag{4.3}$$

where θ_1 and θ_2 are the respective Bragg bearings for the radar beam angles, φ_1 and φ_2, calculated by $\theta_i = \varphi_i + [\varphi_{bi}]_i$ (where $[\varphi_{bi}]_i$ is the bistatic angle for radar beam φ_i). The east and north components can then be recovered from $\nu_E(\varphi_1)$ and $\nu_E(\varphi_2)$ in equation 4.3 by

$$u = \frac{\nu_E(\varphi_1)\cos\theta_2 - \nu_E(\varphi_2)\cos\theta_1}{\sin(\theta_1 - \theta_2)} \qquad v = \frac{\nu_E(\varphi_1)\sin\theta_2 - \nu_E(\varphi_2)\sin\theta_1}{\sin(\theta_2 - \theta_1)}. \tag{4.4}$$

If more than two measurements are available then least squares methods can be used as explained by Paduan and Washburn [76].

This theory has been used and validated in many studies for monostatic radar (see Paduan and Cook [76] or Chapman and Graber [15] for example) and is now operational all over the globe, as discussed in section 1.3.2. Current measurement using bistatic radar has since been introduced, where multistatic radars collect and use both radial and elliptical current measurements. An outline of the theory, with validation, is given by Lipa *et al.* [75] and further experiments have been carried out, for example, by Whelan and Hubbard [99] who showed that the inclusion of elliptical current data, alongside the radials, reduced the uncertainty in the total current measurements whilst substantially increasing the spatial coverage as shown in figure 4.1. Real-time multistatic current measurements are also provided by the Meditteranean Institute of Oceanography [69], where current vectors are available off the coast of Toulon, every 20 minutes, from January 2012.

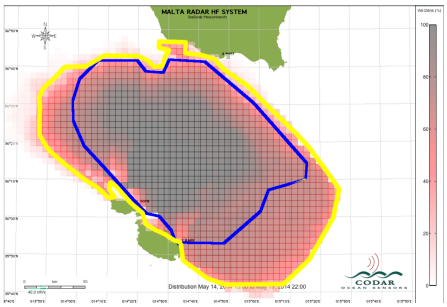

Figure 4.1: A comparison of the percent coverage of total current vectors, when radial-only measurements are used and when elliptical vectors are also included, for a multistatic radar site, presented by Whelan and Hubbard [99]. Although they are imperceptible on the plot, a Seasonde receiver is situated on the south coast of Sicily (top island) and two transmitters (one of which also receives) are situated on the north-east coast of Malta (bottom islands). Radial-only results are outlined in blue and the elliptical-inclusive results are outlined in yellow. The colour bar represents the density of the data coverage for the elliptical-inclusive data.

§ 4.2 Wind Directions

Extracting wind direction measurements from HF radar data was introduced by Long and Trizna [61] and Stewart and Barnum [84], who showed how to get the mean wind direction, θ^*, from experimental data by analysing the ratio of the first order Bragg peaks (also known as the Bragg ratio) of the Doppler spectrum. The Bragg peaks are used for this purpose as the contributing Bragg waves are assumed to be short enough to be driven by local winds, especially at higher radar frequencies.

The positive and negative Bragg peaks, B^+ and B^-, are given by $\sigma(\omega_B)$ and $\sigma(-\omega_B)$ in equation 3.1; namely,

$$B_\pm = 2^5 \pi k_0^4 \cos^4 \varphi_{bi} S(\pm \mathbf{k_B}).$$

The ratio of the first order peaks, R, is then found by calculating $\dfrac{B^+}{B^-}$, which, in dB, is

$$R = 10 \log \left(\frac{S(\mathbf{k_B})}{S(-\mathbf{k_B})} \right). \tag{4.5}$$

From section 1.2.4.3, $S(\mathbf{k})$ is defined by

$$S(\mathbf{k}) = S(k, \theta) = E(k) G(k, \theta), \tag{4.6}$$

where $E(k)$ is the non-directional ocean spectrum and $G(k, \theta)$ is the normalised directional

distribution. Therefore, using equation 4.6 in equation 4.5 gives

$$R = 10 \log \left(\frac{G(\theta_B + \pi)}{G(\theta_B)} \right), \tag{4.7}$$

where θ_B is in the direction of the Bragg bearing, away from the radar setup.

To retrieve the wind direction, θ^*, from equation 4.7, Stewart and Barnum [84] substituted the $\cos^{2s}$ model,

$$G(\theta) = D \cos^{2s}((\theta - \theta^*)/2) \tag{4.8}$$

(for normalisation factor D given in equation 1.28), into equation 4.7 to give

$$R = 10 \log \left(\tan^{2s} \left(\frac{|\theta_d|}{2} \right) \right), \tag{4.9}$$

where $\theta_d = \theta^* - \theta_B$. Equation 4.9 can then be solved for θ_d, such that

$$|\theta_d| = 2 \tan^{-1} \left(10^{\frac{R}{20s}} \right)$$

and thus the mean wind direction can be obtained by calculating

$$\theta^* = \theta_B \pm |\theta_d| = \theta_B \pm 2 \tan^{-1} \left(10^{\frac{R}{20s}} \right). \tag{4.10}$$

This solution, whose ambiguity is evident, depends on s which is, as yet, unknown. Figure 4.2 shows the relationship between R and θ_d in equation 4.9, using the $\cos^{2s}$ model, for different values of s. The figure shows how the value of s can affect the predicted values for any wind direction not perpendicular to the Bragg direction; the error is as much as 40° for the presented values of s.

Stewart and Barnum [84] used a model for the value of s, which in their case, produced good results between predicted and measured wind directions. For a single radar setup, they used any knowledge of local winds to resolve the ambiguity where possible and then resolved the other directions by assuming continuity in the wind field. Heron and Rose [40] proposed an alternative method of resolving the ambiguity, whilst finding a suitable value for s, which used three radar beams, spaced 30° apart. This method, however, assumes that both θ^* and s are stationary over the - possibly large - area, which may pose a problem for nonhomogeneous wind fields. A further potential problem is the choice of directional model; the $\cos^{2s}$ model may not be appropriate in some situations and the aforementioned method does not allow for evaluation of the model. Wyatt *et al.* [108] therefore proposed a method which combats

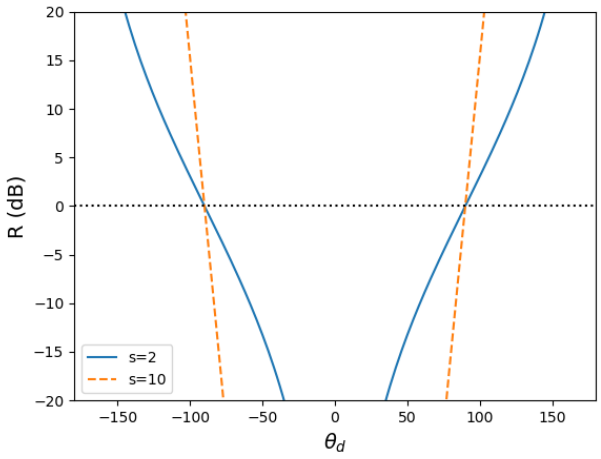

Figure 4.2: The ratio, R, of the Bragg peaks for a varying angle, θ_d, between the wind direction and Bragg direction, calculated using equation 4.9. Two values for the spreading value s in the $\cos^{2s}$ model in equation 4.8 are shown.

these two specific problems. They use the maximum likelihood method to fit the direction and spread parameters, where the stationarity requirements are relaxed to a 10 km^2 area and different models for $G(\theta)$ can be evaluated. The method was designed for use with two radars so that the ambiguity is solved absolutely, however, the method can be applied to a single radar setup, as neighbouring measurement cells are included in the calculations.

The methods outlined in the preceding paragraph, which were introduced and tested for monostatic radars, can be easily adapted for use with a bistatic setup. The theory remains the same, the only difference is the calculation of the Bragg bearing, θ_B. One thing to note is that for large bistatic angles, the associated Bragg waves are longer. Therefore, a range of different Bragg waves may be measured during an inversion of bistatic data and care must be taken when interpreting the results.

Huang [46] has previously shown how to apply the method of Heron and Rose [40] to bistatic radar data and backed it up with experimental results, which showed good agreement with other data sources. In Chapter 5, the maximum likelihood method of Wyatt *et al.* [108] is used to invert both simulated and measured bistatic HF radar data.

4.2.1 Maximum Likelihood Method For Estimating Wind Directions and their Spatial Distribution

The maximum likelihood method, or MLM, finds values for the parameters of a model, based on the likelihood of the data observed. Explicitly, given a data set, $\mathbf{x}$, the MLM seeks to find

the model parameters which maximise the probability of $\mathbf{x}$ occurring.

Following Wyatt *et al.* [108], the ratio of the Bragg peaks was previously found to vary according to an F distribution. The probability density function, or pdf, of the measured Bragg peak ratio is given by

$$P(r_i'; r_i(\theta^*, s)) = \frac{\frac{1}{r_i}\Gamma(\nu)\left(\frac{r_i'}{r_i}\right)^{\nu/2-1}}{\left[\Gamma\left(\frac{\nu}{2}\right)\right]^2\left(1+\frac{r_i'}{r_i},\right)^{\nu}}, \tag{4.11}$$

where Γ is the gamma function, ν is the degrees of freedom of the distribution (explained below), r_i' is the observed Bragg ratio and r_i is the true Bragg ratio. The value of r_i is calculated using a directional model, which for illustrative purposes is here the $\cos^{2s}$ model, which depends on θ^* and s. The degrees of freedom, ν, is determined by the signal processing techniques used to obtain the Doppler spectrum. Namely,

$$\frac{1}{\nu} = \frac{1}{2M}\left[1 + 2\rho^2(75\%) + 2\rho^2(50\%) + 2\rho^2(25\%)\right] - \frac{1}{M^2}\left[\rho^2(75\%) + 2\rho^2(50\%) + 3\rho^2(25\%)\right],$$

where M is the number of data segments used in averaging the signal and $\rho(n\%)$ is the $n\%$ overlap coefficient for the window used (given by Harris [34]).

The MLM thus tries to find the parameters, θ^* and s, which maximise

$$P(r'; r(\theta^*, s)) = \prod_{i=1}^{n} P(r_i'; r_i(\theta^*, s)), \tag{4.12}$$

or, equivalently, the parameters which minimise

$$P(r'; r(\theta^*, s)) = \sum_{i=1}^{n} -\ln\left(P(r_i'; r_i(\theta^*, s))\right), \tag{4.13}$$

for n Bragg ratios. The n ratios are measured in an area where the wind distribution is assumed to be stationary and may be from multiple radars. Wyatt *et al.* [108] assumed a stationary wind distribution over 10 km^2 grids where data from two radars were used. Minimisation routines, such as the *Scipy.optimize.minimize* module in Python can then be used to find the solution; in this case a Nelder Mead function has been used. The confidence interval for each solution can be found by finding the inverse of a Hessian matrix as described in detail by Wyatt *et al.*.

Different models for $G(\theta)$ can be evaluated in this method by replacing the model used to generate the r values in the code and rerunning the minimisation routine. The model which

outputs a lower minimum for the same set of data is deemed the better choice.

§ 4.3 Waves

Wave measurements, both ocean surface parameters (such as significant waveheight) and the directional spectrum, are routinely obtained from HF radar data. Works of Lipa [57][58][60], Wyatt [103] and Hisaki [41], amongst others, are notable in the history of inverting $\sigma(\omega)$ for $S(\mathbf{k})$ numerically. Lipa and Nyden [60] adapt the radar cross section so that it is applicable to broad beam radars - such as the CODAR Seasonde - and then perform a least squares fitting on a linearized version of the radar cross section and the second order sidebands to predict h_s, t_p and θ_m. However, due to the broad beam, they assume that the ocean spectrum is homogeneous over a whole range annulus, which limits their wave inversion procedure to close ranges. The method of Wyatt [103], which is applicable to narrow beam radars such as the WERA phased array radar, is described in more detail in section 4.3.1. Empirical methods such as that of Gurgel [32], who empirically fits waveheight to the second order sidebands using a wave buoy, are also possible if one wants to avoid inverting the integral equation.

The methods mentioned in the preceding paragraph were designed and tested for monostatic radar systems. In theory, and as stated by Anderson [4], the existing algorithms should work for a bistatic system if the inverted integral equation is changed to the bistatic expression in equations 3.1 and 3.2. Zhang and Gill [111] have developed an inversion algorithm to obtain the nondirectional wave spectrum from bistatic radar data and when tested on simulated data, they obtained good results. Silva *et al.* [80] have also presented results of simulated bistatic HF radar data inversion where the directional wave spectrum was estimated using Tikhonov regularization. They achieved good results for simulated data, yet the method is limited as a model is assumed for the direction of the spectrum, which may not always be appropriate. No results have thus far been presented of real bistatic HF radar data inversion; results of this kind are presented for the first time in Chapter 5.

The Seaview inversion method, described in section 4.3.1, is currently being modified to allow for bistatic radar wave inversion and results will be presented in the near future.

4.3.1 Seaview Inversion Method

As first presented by Wyatt [103], the Seaview inversion (so named because it is being further developed by and is available from Seaview Sensing Ltd.) is an iterative method which begins with an estimated directional spectrum and progressively modifies it to minimise the difference between the calculated and measured Doppler spectra. As explained by Wyatt [104],

the initially estimated spectrum is modelled using a Pierson Moskowitz spectrum with a sech directional model, using an empirically estimated waveheight and a wind direction derived from analysis of the first order peaks. The monostatic second order radar cross section expression in equation 2.123 is used to calculate the Doppler spectrum using the estimated $S(\mathbf{k})$ and the output is compared to the measured Doppler spectrum. The spectrum $S(\mathbf{k})$ is then updated as by the rules of the algorithm, and the process is continued until an accepted level of tolerance is achieved between the predicted and measured Doppler spectra. The method is restricted to the frequencies close to the Bragg peaks, where the shorter wave, $\mathbf{k_2}$, is assumed to be approximately equal to the Bragg wavevector and thus driven by local winds. The initially estimated spectrum can then be used to model $\mathbf{k_2}$ and then equation 2.123 is simplified and the resulting expression is quasi-linear.

Two Doppler spectra are used at every location in order to resolve the directional ambiguity and only the sidebands (± 0.6 Hz) around the dominant Bragg peak are used. Furthermore, a signal to noise ratio of 15 dB of the largest sideband is a minimum requirement and each spectrum is normalised by the power in the first order peak, to remove radar effects such as path loss.

4.3.2 Limitations and Motivation

The majority of the wave inversion methods mentioned use the second order sidebands to obtain wave information. This means that the inversion is less reliable than the wind and current inversions (whose methods mainly use the first order contribution) due to a lower SNR. Furthermore, the perturbation method of Barrick [5], which was followed in Chapter 2, to derive the radar cross section expression is used in the mathematical inversions but it is only valid for small ocean wave heights in comparison to the radar wavelength. Hence the theory breaks down for particularly high wave conditions. Therefore, if one wishes to observe larger waves, lower frequencies should be used.

Alternatively, Wyatt *et al.* [106] explain how, in the Seaview method, the first order Bragg peaks are scaled, such that the second order continuum is increased in comparison to the first, for a given waveheight. The scaling is based on the work of Creamer *et al.* [18], who showed that a second order contribution - due to the combination of first and third order ocean waves - was missed in the derivation of the radar cross section by Barrick [5][7] and is significant at larger waveheights. The improvement in the results when the scaling is included is shown in the work of Wyatt *et al.* [106].

In addition to the low SNR and high sea state issues, the Doppler spectrum can be contam-

inated by sidelobes, current shear, or variation due to low cell resolution - as described in section 3.4. In these situations, the radar cross section is no longer representative of the data and therefore these data are not suitable for the inversion methods based on the expression. Therefore, if any potential, expected, inaccuracies of the radar data can be included in the radar cross section expressions, then successful inversion of the updated radar cross section should recover the information.

§ 4.4 Neural Network Inversion Method

With the limitations discussed in section 4.3.2 in mind, a new inversion method is proposed, where an artificial neural network, or ANN, is used to invert radar Doppler spectra, $\sigma(\omega)$, to infer $S(\mathbf{k})$.

Fundamentally, an ANN is a nonlinear regression model, that learns by example, usually by using a vast dataset of input and output pairs, $(\mathbf{x_i}, \mathbf{y_i})$. The ANN, such as that shown in figure 4.3, consists of an input layer, a number of hidden layers and an output layer, each of which comprises a varying number of *nodes*. In a process called forward propagation, a single node receives input from either an external source or a number of other internal nodes and then performs a weighted sum, where the weights represent the importance of the node connection. A non-linear function, g, known as an activation function, is then applied to the sum, which allows it to model non linear functions. Mathematically, at layer l, we compute the value $\mathbf{a}^{(l)}$, in vectorised form, as

$$\mathbf{a}^{[l]} = g\left(\mathbf{z}^{[l]}\right); \qquad \mathbf{z}^{[l]} = \mathbf{w}^{[l]}\mathbf{a}^{[l-1]} + \mathbf{b}^{[l]}, \tag{4.14}$$

where $\mathbf{z^{[l]}} \in \mathbb{R}^{m\times 1}$, $\mathbf{w}^{[l]} \in \mathbb{R}^{m\times n}$, $\mathbf{a}^{[l-1]} \in \mathbb{R}^{n\times 1}$ and $\mathbf{b}^{[l]} \in \mathbb{R}^{m\times 1}$, for an additional bias vector $\mathbf{b}^{[l]}$ which makes the model more flexible. This process is continued, from left to right, until the output layer is reached and a prediction, $\hat{\mathbf{y}}$, is made, based on the input $\mathbf{x}$.

The goal of a neural network is to learn appropriate values for randomly initalised weights and biases, $\mathbf{w}$ and $\mathbf{b}$, in order to accurately map some input vector $\mathbf{x}$ to an output vector $\hat{\mathbf{y}}$, in consideration of a metric $C(\mathbf{y}, \hat{\mathbf{y}})$, called the *cost function*. The cost function measures how well a neural network is performing by quantifying how close the predicted values, $\hat{\mathbf{y}}$, are to the desired values, $\mathbf{y}$. Although there are a number of possible metrics to use [21], in this work, we use the mean squared error cost function, which is given by

$$C(\mathbf{w}, \mathbf{y}) = \frac{1}{2M}\sum_{i=1}^{M} \left|\hat{\mathbf{y}}(\mathbf{w})_i - \mathbf{y}_i\right|^2, \tag{4.15}$$

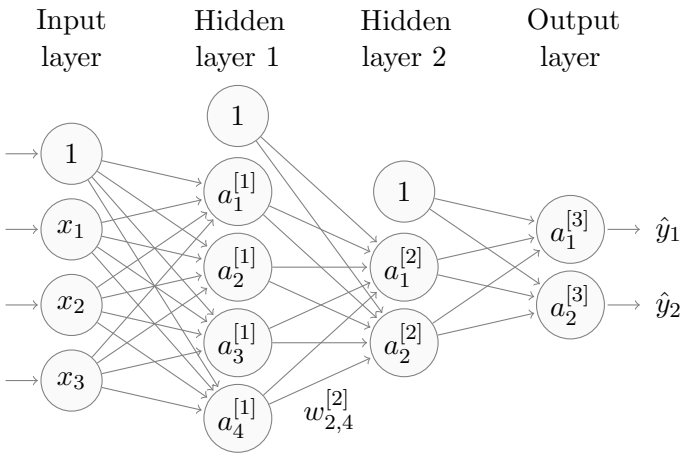

Figure 4.3: Basic neural network architecture with 3 input features, $\mathbf{x}$, 4 and 2 nodes in two hidden layers and 2 output features, $\hat{\mathbf{y}}$. Additional bias nodes are shown at the top of the first three layers which make the model more flexible. The weights are represented by the lines connecting the nodes and weight $w_{2,4}^{[2]}$ is shown to highlight the notation.

where M is the total number of training examples. An accurate model corresponds to a smaller value for $C(\mathbf{w}, \mathbf{y})$ and hence, the goal is minimise $C(\mathbf{w}, \mathbf{y})$.

To minimise the cost function, its derivatives, with respect to the weights and biases, are calculated in a process called backpropagation and then the weights are updated by an optimising algorithm such as gradient descent, Adam [52] or RMSProp [90]. The training algorithm, which consists of calculating forward and then backward propagation, before updating the weights, is repeated over the data pairs, until either a set number of iterations are executed, or a specific accuracy level, between the predicted $\hat{\mathbf{y}}$ and desired $\mathbf{y}$, has been reached. An unbiased test is then carried out, using a *test set*, which is a reserved portion of the dataset that the neural network was not been trained on. The test set shows how well the neural network performs on unseen data which is more of an indicator of how it will perform operationally.

The performance of the neural network largely depends on its architecture, and the following *hyperparameters* can be influential: (1) the number of hidden layers, (2) the number of nodes per layer, and (3) the number of iterations. Although, not technically hyperparameters, in this work, we also treat the optimisation method and the activation function choice as hyperparameters too, as we found the choice of these impacted the results. There is no one rule on how to choose the optimal values of the hyperparameters, it is often a case of investigating different combinations and finding one that is within a tolerance. In this work, we use a genetic algorithm to search more intelligently through the solution space; although omitted here, a rigorous introduction to the subject of genetic algorithms is given by Mitchell [71].

A third data set - known as the *validation set* - should be used to choose the optimal hyper-parameters. The third set is used to avoid the algorithm becoming biased toward the test set, and unable to accurately invert unseen data. Again, there is no set rule for how to split the dataset, however, it is important that the ANN has enough data to be trained on, especially if it is a complex function. Furthermore, each of the training/test/validation sets should have similar characteristics to make the test fair.

In comparing how well the ANN performs on the training and test sets, we can diagnose problems such as *overfitting*, which is where the model fits the training data *too* well and cannot generalise to unseen data, or *underfitting*, where the model does not fit either the training or test data well. To remedy overfitting, a regularization method can be used, where the cost function is penalised, preventing it from becoming too near zero. To remedy underfitting, we must adjust the neural network architecture.

In this work, the goal is to train an artificial neural network that can accurately predict directional wave spectra, $S(\mathbf{k})$, from radar Doppler spectra, $\sigma(\omega)$. To do this, the ANN is trained on data pairs consisting of $\sigma(\omega)$ as the input and $S(\mathbf{k})$ as the output. The values for $\sigma(\omega)$ are generated using the simulation methods of Chapter 3 with measured/modelled $S(\mathbf{k})$ input. The motivation is that there is currently no reliable way to invert Doppler spectra that cannot be accurately modelled by the radar cross section integral expression. As an ANN learns by example, it *should* be able to learn to invert that data, as long as the problem is set up correctly. It is also of interest to see how it compares with existing inversion methods.

Although this is the first time that a neural network has been used to invert Doppler spectra for the directional ocean spectra, they have been used for obtaining wind speeds and predicting the sea level. Mathew *et al.* [67], trained a neural network which used HF radar measured values of significant waveheight, wave period, wave direction and wind direction as input, to predict wind speed as measured by a wave buoy. Zeng *et al.* [110] did the same but removed wave direction from the dataset. Similarly, Shen *et al.* [79] trained a neural network to predict wind speed using the measurements of a local wave buoy and HF measured first order Bragg peaks. Wahle and Stanev [97] trained a neural network to learn the relationship between tidal gauge data and HF radar current measurements to predict sea level from HF current data. They also trained a neural network to forecast sea level. Seemingly all of the previous neural network applications in the field have used other measuring devices, such as wave buoys, to train their algorithms. In this work, by using simulations, no other device is necessary and thus the HF radar system remains independent, with no dependence on other devices.

In Chapter 5, the results of two experiments, both where an ANN is used to invert Doppler spectra, are presented. In the first experiment, two ANNs are trained to invert monostatic

Doppler spectra that are simulated using the numerical method of section 3.3. This experiment is to test whether the ANN inversion method can invert Doppler spectra that can be accurately modelled by the radar cross section equations. In the experiment, the established Seaview inversion method, which has been validated on monostatic radar data, is used as a benchmark for the ANN method. The method is further validated using directional spectrum data from a wave buoy. A first ANN is trained on data in a single location, then a second ANN is trained on a number of different locations in an effort to understand the effects of the radar beam angles on the Doppler spectra.

A second experiment is then carried out to see if the inversion method can invert bistatic Doppler spectra. Firstly, an ANN is trained on data simulated using the numerical method described in section 3.3. A second ANN is then trained on data simulated using the method in section 3.4, where the radar effects are included.

To summarise, four neural networks will be trained to invert:

1 monostatic Doppler spectra, simulated using the numerical method of section 3.3, in a single location (SLNN);

2 monostatic Doppler spectra, simulated using the numerical method of section 3.3, in multiple locations (MLNN);

3 bistatic Doppler spectra, simulated using the numerical method of section 3.3, in a single location (BNN);

4 bistatic Doppler spectra, simulated to include radar effects using the simulation method of section 3.4, in a single location (CBNN).

4.4.1 Method

Although it may be possible for a neural network to learn to resolve the directional ambiguity that exists for a single radar, this is yet to be tested. Therefore, to resolve the directional ambiguity, two radars will be used to provide two spectra for each location. Consequently, in general, the neural network will have two radar Doppler spectra as the input and the corresponding directional ocean spectrum as the output.

Depending on where the radars are situated, we define φ_1 and φ_2 as the beam angles, measured clockwise from north, from each radar to a measurement point (see figure 4.4). As the beam angles are different for each measurement location in the radar coverage area, the resulting Doppler spectra are also different. Therefore, either a different neural network must

be trained for every desired location, which will be referred to as the single location neural network (SLNN), or a single neural network must be able to represent the relationship between φ_1, φ_2 and the related Doppler spectra, which will be referred to as the multi location neural network (MLNN).

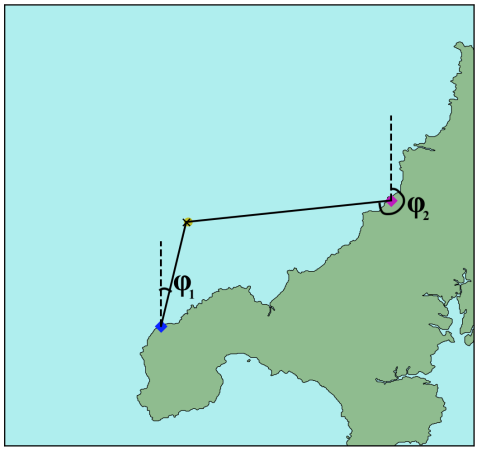

Figure 4.4: Beam angles φ_1 and φ_2 for two radars, shown by the blue and magenta diamonds, where both are measured, clockwise from north, from the radar to a scatter point (which is shown by the cross).

For both neural network experiments, the training/test data is generated in the same way. Beginning with a large dataset of directional ocean spectra, whether modelled or measured, we use a prescribed simulation method, to simulate the corresponding Doppler spectra at a particular location, for both radars. The radar frequencies, the depth of the ocean and the beam angles (φ_1 and φ_2) are fixed and two 512-point Doppler spectra ranging from -1.27 Hz to 1.27 Hz are simulated. These simulations should mimic the real data as closely as possible to make the neural network's task less complicated and therefore, appropriate noise floor and general noise levels have been included in the simulations, after analysing the available measured radar data.

Then, any Doppler spectrum input to the neural network - so either the simulated data or the measured validation data - are filtered and processed. Firstly, a SNR of 10 dB for the second order peaks has been set as a minimum requirement for a Doppler spectrum to be used in the neural network and anything below is discarded, as high noise levels may complicate the neural network model. This is below the 15 dB limit used in the Seaview inversion and, from experimenting, it is a variable that does impact the results. A number of neural networks were trained to test the effect of the SNR limit and a higher value of 15 dB negatively impacted the results, possibly due to the smaller resulting training dataset. Secondly, any Doppler shifts induced by currents are removed and then the resulting Doppler spectra are normalised

so that the first order peaks are set to 1 and -1, with the highest Bragg peak set to a fixed value, here 70 dB. Thirdly, values ± 0.6 around each peak are used as input to the neural network, which in these experiments gives a 174 point array for each radar, say $\sigma(\eta)_1$ and $\sigma(\eta)_2$, resulting in a 348 point array when combined as $[\sigma(\eta)_1, \sigma(\eta)_2]$. This smaller subset of points is retained so that the neural network focusses on the more important second order peaks whilst ignoring the less important, more noisy, outer parts of the Doppler spectrum. Finally, the output values, $\hat{\mathbf{y}}$, the directional spectra, are interpolated onto a grid of 36×98, where there are 36 directional values in the range $[0,\ 2\pi]$ and 98 wavenumber values in the range [0.004, 0.986]. The values are then each multiplied by the wavenumber k, for scaling purposes, and the 2D matrix is flattened, to form a vector of size 3528, ready for processing.

In each ANN, an elu function, namely

$$g(x) = \begin{cases} x, & x \geq 0 \\ \alpha(\mathrm{e}^x - 1), & x < 0 \end{cases}$$

is used as the activation function in the final layer to encourage the output spectrum values to be positive. The cost function, $C(\hat{\mathbf{y}}, \mathbf{y})$ is defined as the mean squared error of the predicted and actual values, as given in equation 4.15. To implement the neural network, the Tensorflow framework [88] for Python 3 has been used.

4.4.1.1 Single-location Neural Network

In training the neural network for a single location, so for the SLNN, BNN and CBNN inversions, φ_1 and φ_2 are fixed and are therefore unnecessary to the learning process. Thus, the i^{th} input vector, $\mathbf{x_i}$, is defined as the two radar Doppler spectra subsets joined together, $[\sigma(\eta)_1, \sigma(\eta)_2]$, and the i^{th} output vector, $\mathbf{y_i}$, is defined as the directional ocean spectrum, $S(\mathbf{k})$, that was used to generate $\sigma(\eta)_i$ vectors (see figure 4.5).

4.4.1.2 Multi-location Neural Network

For a neural network being trained to understand location during the inversion, or the MLNN, the beam angles φ_1 and φ_2 must also be passed into the algorithm. Thus the i^{th} input, $\mathbf{x_i}$ is defined as the 350-point vector $[\varphi_1, \sigma(\eta)_1, \varphi_2, \sigma(\eta)_2]$ and the i^{th} output, $\mathbf{y_i}$, is the corresponding, flattened, $S(\mathbf{k})$; see figure 4.6. The values for φ_1 and φ_2 are also scaled to be the same order as the Doppler spectra values.

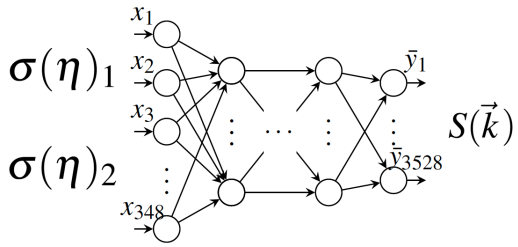

Figure 4.5: Neural network structure for the SLNN inversion, with input Doppler spectra, $[\sigma(\eta)_1, \sigma(\eta)_2]$, and output directional ocean spectra, $S(\mathbf{k})$. Note that bias nodes are omitted in the figure but are included in the training process.

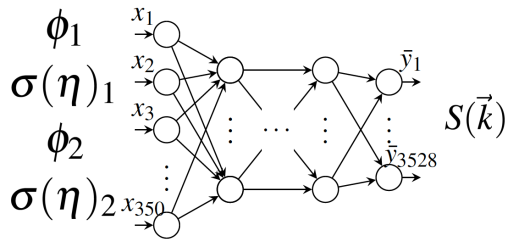

Figure 4.6: Neural network structure for the MLNN inversion, with input $[\varphi_1, \sigma(\eta)_1, \varphi_2, \sigma(\eta)_2]$ and output direction ocean spectrum, $S(\mathbf{k})$. As in figure 4.5, the bias nodes have been omitted but are included in the training process.

Summary

In this chapter, methods for obtaining current, wind direction and wave measurements from bistatic HF radar data have been introduced. Details of how to adapt the existing monostatic methods for use with a bistatic radar were given and then a new inversion method was proposed for obtaining the directional wave spectrum. The method uses an artificial neural network, with the motivation that it should be able to invert data where the radar effects cannot be ignored, which is when the existing methods are not applicable.

In the next chapter, a number of the methods introduced in this chapter are tested. The maximum likelihood method is used to obtain wind direction distributions from both simulated and measured bistatic HF radar data. The neural network inversion method is then tested on monostatic radar data and validated using directional wave buoy data and the Seaview inversion method. It is further tested on bistatic HF radar data where the effects of the radar are included; the data of a directional wave buoy is again used to validate the results.

Chapter 5

HF Radar Inversion Results

In this chapter, wind direction and wave inversion algorithms introduced in Chapter 4 are tested. In section 5.1, the maximum likelihood method, or MLM, is used to obtain wind direction distributions from bistatic HF radar data and the results are validated using scatterometer data. In section 5.2, monostatic Doppler spectra are inverted using the neural network inversion method described in section 4.4 and the results are validated with the Seaview inversion method and a directional wave buoy. In section 5.3, the neural network inversion method is tested on bistatic Doppler spectra and validated using a directional wave buoy. Two neural networks are tested: (1) trained using bistatic Doppler spectra simulated using the numerical method of section 3.3 and (2) trained using bistatic Doppler spectra simulated using the method of section 3.4, where radar effects are included.

§ 5.1 Maximum Likelihood Method for Estimating Wind Direction and its Spatial Distribution

As a preliminary test, the MLM (first applied to wind direction inversion by Wyatt *et al.* [108] as explained in section 4.2.1) is used to invert simulated ratio values. This is done to see how the algorithm performs on inverting data with varying degrees of freedom and for different directional models. The method is then tested on the bistatic WERA dataset, described in section 3.2.1, where ASCAT scatterometer data is available to validate the results. For both the simulated and measured data experiments, the data is for a single radar. Hence this work is a test of the ability of the algorithm to use only neighbouring cells to resolve, or not, this ambiguity.

Like Wyatt *et al.* [108], Doppler spectra in ~ 10 km^2 grids have been used to calculate each measurement which leads to 9 spectra for this data resolution and single radar setup. For

both experiments, the Scipy.optimize.minimize module was used to find the best values for the wind direction and spread parameters, using a Nelder-Mead algorithm. For each location, the algorithm was initialised with a number of different wind directions so that it did not get stuck in any local minima. Two directional models were evaluated in both experiments to see which was more appropriate:

- $G(\theta) = D\cos^{2s}\left((\theta - \theta^*)/2\right)$, where θ^* and the spreading value, s, are sought;
- $G(\theta) = D\beta\,\mathrm{sech}(\beta(\theta - \theta^*))$, where θ^* and the spreading value, β, are sought.

In both models, the factor D is the normalisation term given in equation 1.28.

5.1.1 Simulated Data

As the MLM method will also be tested on the bistatic WERA radar dataset, the bistatic setup of that radar is emulated when testing the method on simulated ratio values. The range resolution of the radar is 3 km so ratio values, in 3 km increments (by bistatic range), have been simulated from 5 to 47 km; for each range, the ratios are simulated in 5° increments from 160° to 235°, so that the coverage area is similar to the real dataset.

The ratio values are simulated using equation 4.7, explicitly

$$R = 10\log\left(\frac{G(\theta_B + \pi)}{G(\theta_B)}\right), \tag{5.1}$$

where θ_B is the Bragg bearing in the direction away from the radar setup. Both the sech and $\cos^{2s}$ directional models are substituted into equation 5.1 and individually tested. For this preliminary test, a uniform wind field has been assumed. Noise is added to the simulated ratios, which is randomly distributed from the F-distribution for varying degrees of freedom, ν. The noisy ratio values are then inverted and the resulting θ^* and spread values are compared with the input values.

So that the results of the directional models are directly comparable, the *spreading angle*, σ_s, which indicates the directional variation of the waves from the mean direction, has been used. From Hauser *et al.* [37], the spreading angle of the sech model is given by

$$\sigma_{\mathrm{sech}} = \left(2\left(1 - \frac{\pi}{2\beta\sinh(\pi/(2\beta))}\right)\right)^{1/2} \tag{5.2}$$

and for the $\cos^{2s}$ model, it is

$$\sigma_{\cos} = \left(\frac{2}{s+1}\right)^{1/2}. \tag{5.3}$$

Using equations 5.2 and 5.3, values for s and β can be found such that $\sigma_{\text{sech}} = \sigma_{\cos}$. An example of the MLM inversion results where $\theta^* = 88°$ and $\sigma_s = 25°$ is shown in figure 5.1, where the root mean square error, or RMSE, of the derived θ^* and σ_s values are shown for a range of ν values. A subset of the derived parameters are shown in figure 5.2, to show the affect of the added noise.

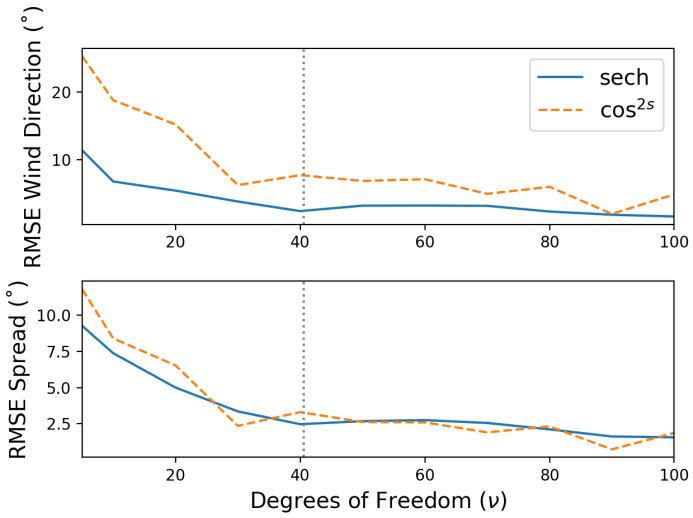

Figure 5.1: RMSE values for the MLM derived wind directions and spreading angles, both in degrees. A comparison of the results for the sech and $\cos^{2s}$ models is shown. The dashed vertical lines indicate the degrees of freedom used in the inversion of the bistatic WERA dataset.

Both directional models perform similarly when inverting the spreading angle, however, the sech model performs slightly better than the $\cos^{2s}$ model, when θ^* is measured. As expected, the accuracy of the MLM results increase as the degrees of freedom increase, with values of $\nu >\sim 30$ performing well.

5.1.2 Real Data

To test the method further, the bistatic WERA data described in section 3.2.1 is inverted. 'Advanced SCATterometer' (ASCAT) data from EUMETSAT [24] for the same time period is used to validate the derived wind directions. There are seven occasions when the radar and ASCAT datasets overlap and due to the ASCAT having less fine resolution than the radar,

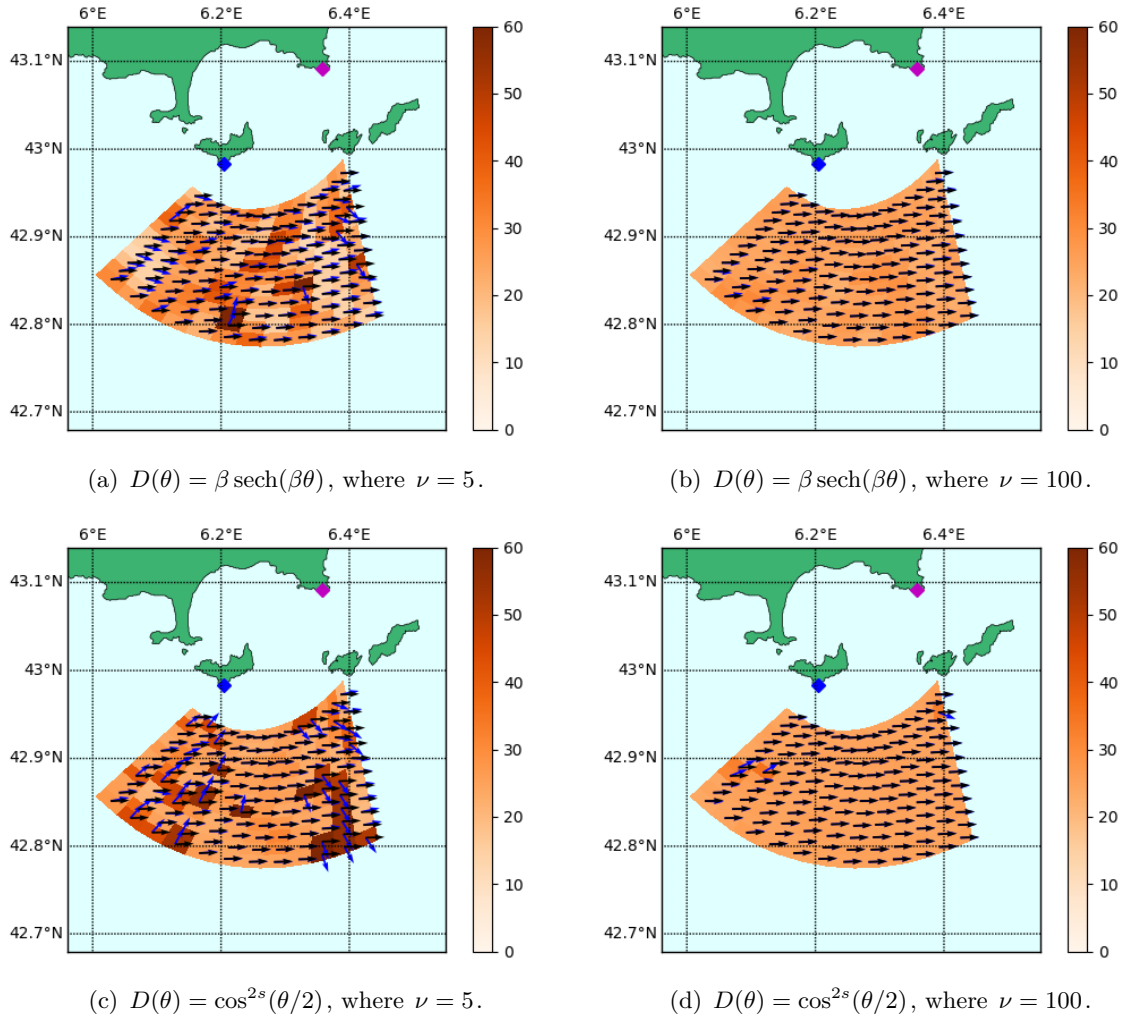

(a) $D(\theta) = \beta\,\mathrm{sech}(\beta\theta)$, where $\nu = 5$.

(b) $D(\theta) = \beta\,\mathrm{sech}(\beta\theta)$, where $\nu = 100$.

(c) $D(\theta) = \cos^{2s}(\theta/2)$, where $\nu = 5$.

(d) $D(\theta) = \cos^{2s}(\theta/2)$, where $\nu = 100$.

Figure 5.2: MLM derived values for θ^* and spread (in degrees), shown by the blue arrows and background colour, respectively, for two directional models and two values of degrees of freedom, ν. The simulated values of θ^*, which should be 88°, are shown by the black arrows. The simulated value of σ_c is 25°.

there are only 57 data points to compare in total. Directional ocean spectra from a local CANDHIS wave buoy (described in section 3.2.2) were also obtained but, unfortunately, the buoy is situated in an area where there is a substantial variation in the Bragg frequency (and hence first order spreading) and a low SNR. It has, therefore, not been used for validating the method, just for analysing the wave spectra in the area.

Determining the location of the Bragg peaks was challenging in parts of the radar coverage area, due to broadened Bragg peaks. In an attempt to identify the appropriate peaks, pairs of points at a distance of $2\omega_B$ apart were compared and then the pair with the largest combined total amplitude was chosen. A SNR of 5 dB for both peaks was set as a minimum

requirement for a spectrum to be inverted. The radar data - which has 3 km range resolution - was beamformed onto a grid with 5° azimuthal resolution which corresponds to distances of $\sim$ 2 km, at range 6 km, to $\sim$ 4 km, at range 57 km. The radar measured time series consist of 4096 samples and to obtain the power spectrum, 75% overlapping Nuttall windows of length 512 have been averaged; this results in the degrees of freedom, $\nu \approx 40.6$, and figure 5.1 suggests that we should therefore expect results with an error of less than 10°, in both direction and spread.

The results of the MLM algorithm, for one of the seven overlapping times, is shown in figure 5.3; in this example, the sech directional model has been used. The nearest ASCAT data to this time is also shown for comparison. The derived winds are generally travelling in an easterly direction, however, there are some clear cases where the ambiguity has not been resolved correctly.

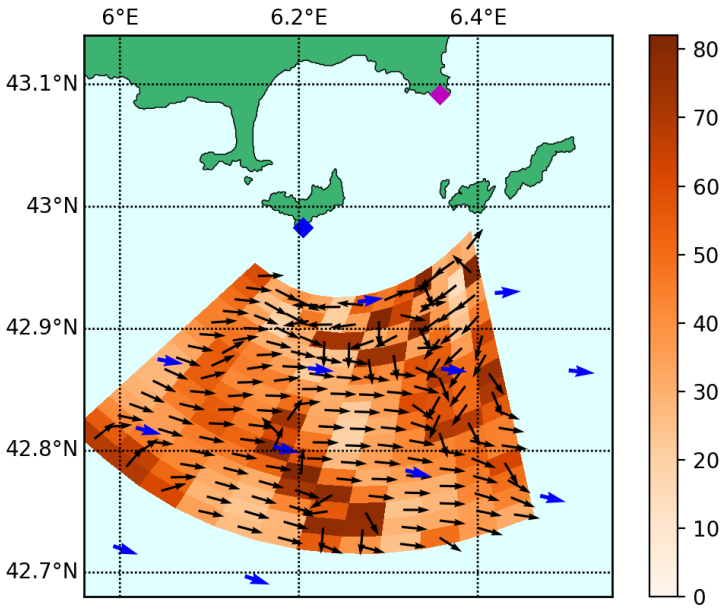

Figure 5.3: Derived wind direction and spread values using the MLM on the bistatic WERA radar data described in section 3.2.1 on 12$^{\text{th}}$ July 2014 09:21. The sech directional model has been used where the spreading angle, in degrees, is shown by the background colour and the derived wind direction is shown by the black arrows. The blue arrows show ASCAT wind direction data for the same date at 09:18.

To address this problem, the directions have been retrospectively rotated around their Bragg bearing if it makes the wind field more consistent. The resulting wind directions, for both the sech and $\cos^{2s}$ models are shown in figure 5.4. The directions derived, using both models, look to be fairly consistent with the ASCAT data, with the sech model slightly more so, especially along the left-hand side. A numerical comparison was carried out for the whole

dataset, where the derived directions closest to each of the ASCAT measured wind directions in the coverage area were used. The results are shown in table 5.1, where the RMSE and median error have been calculated. The sech model has a higher RMSE but a lower median error than the $\cos^{2s}$ model but both have a larger RMSE than median error value. The large RMSE values are due to a small subset of the dataset having substantial discrepancies; this is shown by the lower values for the median errors.

	RMSE	Median
sech	41.78°	14.19°
$\cos^{2s}$	30.85°	15.49°

Table 5.1: Numerical comparison of the wind directions derived by the MLM - for both the sech and $\cos^{2s}$ models and the directions measured by the ASCAT data [24]. The error is quantified by the root mean square error (RMSE) and median error values of 57 results.

The $\cos^{2s}$ and sech directional models were compared by the minimum value each model achieved when running the minimising algorithm and the results, for the same example date as in figures 5.3 and 5.4, are shown in figure 5.5. In 76% of the locations, the sech model was found to have a lower minimum and hence be more suitable. In fact, the sech model was found to be the more suitable model in every instance, where - on average - it was found to be more appropriate for over 80% of the area. This could possibly be to do with the sech directional model function being more suitable for mathematical minimisation, or because the model is more appropriate for the area, due to the model allowing for waves in the direction opposite to the wind direction.

The wind directions derived using the MLM show fairly good agreement with the validating ASCAT data, especially considering that this was for data from a single radar. However, after analysing the results, the algorithm seems to struggle at locations where the value of φ_{bi} is large (see figure 5.6). For this particular dataset, there is a clear difference in the derived wind directions along the right-hand side, and, in this area, the values of φ_{bi} are larger than the rest of the coverage area. This is perhaps caused by a problem in the peak finding algorithm, where sidelobes from other locations, for different values of φ_{bi}, have made it difficult to identify the correct peaks. Another possible explanation is that the different Bragg waves, that are being measured, are not all wind-driven. An analysis of CANDHIS wave buoy spectra, shown in figure 5.7, shows how the Bragg wave frequency varies over the experiment area in comparison to the measured wave spectra. Given the radar frequency of 16.127 MHz and the scattering geometry of the radar, the frequencies of the Bragg waves vary between 0.34 and 0.41, which, by studying the spectra should, indeed, be picking out the wind wave spectrum, not swell. Therefore, it is likely that it is a peak identification problem and a more sophisticated method must be sought to solve it.

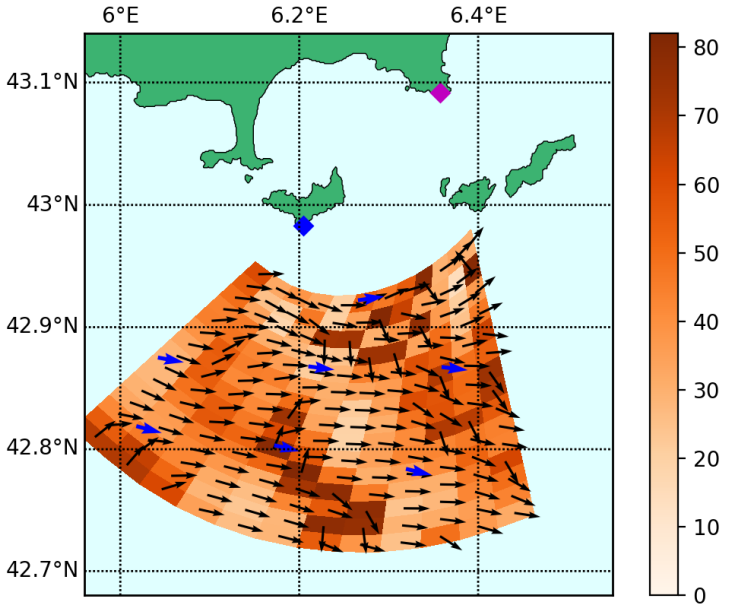

(a) Sech model

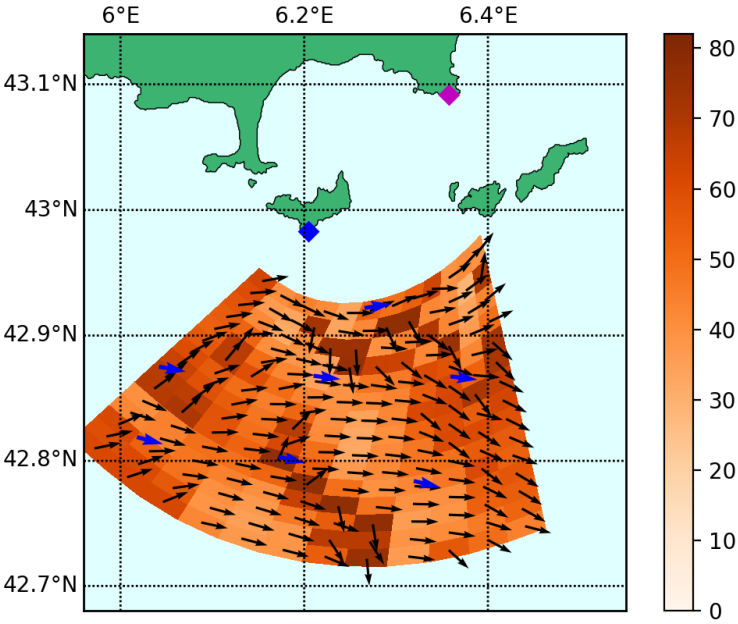

(b) $\cos^{2s}$ model

Figure 5.4: Comparison of the derived wind directions and spreading angles using the MLM for two different directional models, for the same bistatic data as figure 5.3. Continuity of the wind field has been added. In both cases, the spread value is shown in degrees by the background colour and the derived wind direction is shown by the black arrows. The blue arrows show ASCAT wind direction data.

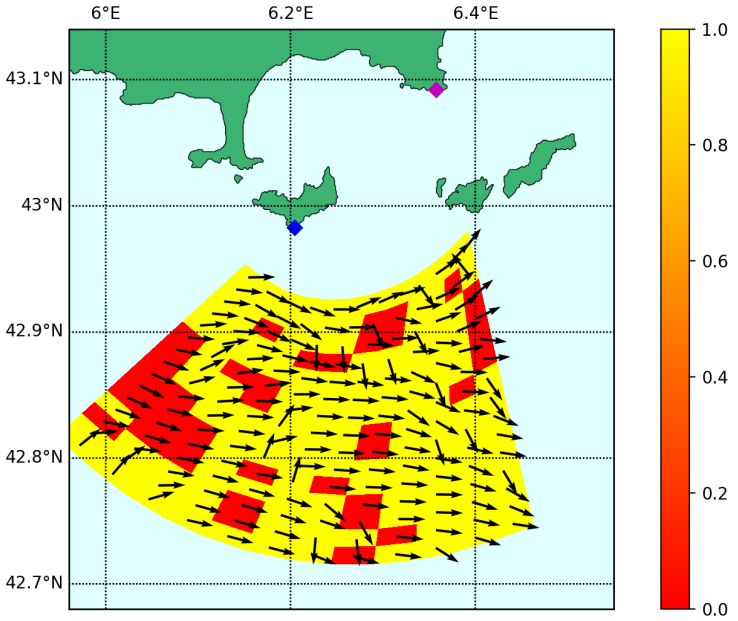

Figure 5.5: Results of the evaluation of the directional models $G(\theta)$ for the bistatic data described in figure 5.3. Where the sech model produced a lower minimum, the location is coloured yellow and where the $\cos^{2s}$ model did, the location is coloured red. The MLM-derived values of θ^* for the sech model are shown by the black arrows.

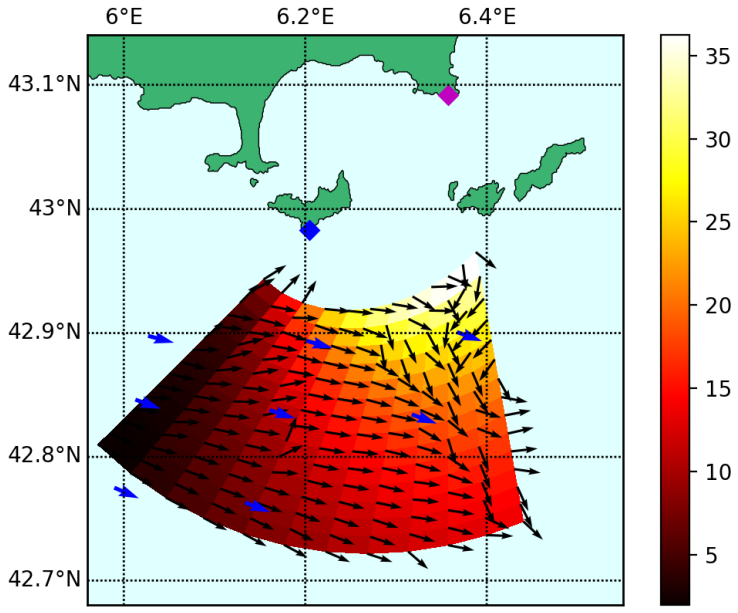

Figure 5.6: MLM-derived values for θ^*, modelled with a sech directional model, for bistatic WERA data on 10/07/2014 09:01:00. The background colour shows the value of φ_{bi}, in degrees, for each location. The blue arrows show the ASCAT wind direction values for 10/07/2014 09:06:01.

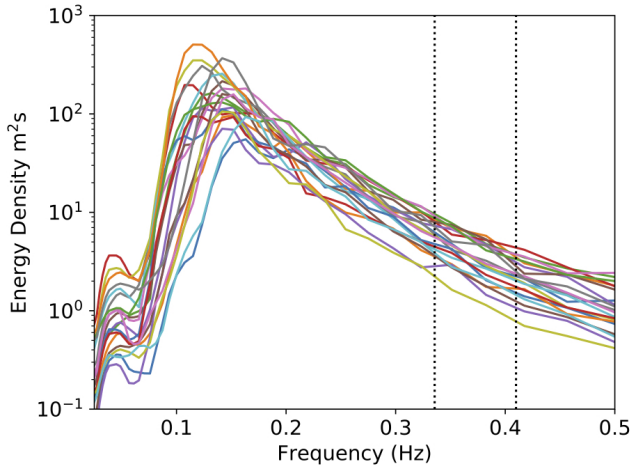

Figure 5.7: Measured wave spectra from the CANDHIS wave buoy, for a range of dates, are shown by colour. The dotted vertical lines show the minimum and maximum frequencies of the Bragg waves measured in the bistatic WERA experiment coverage area.

§ 5.2 Monostatic HF Radar Neural Network Inversion

In this section, the neural network inversion method is tested on monostatic HF radar data using a local wave buoy for validation. The method is further validated by comparing the results against the Seaview inversion method described in section 4.3.1.

In section 5.2.1, the datasets used in the experiment are described. The experimental details are given in section 5.2.2, before the results for both the ANN and Seaview inversion methods are presented in section 5.2.3.

5.2.1 Data

5.2.1.1 HF Radar

In the experiment, HF radar data, obtained by two monostatic WERA HF radar systems [31] on the north coast of Cornwall (Conley 2013, unpublished data), are used to validate the inversion methods. The radars, operated by Plymouth University, were set up to aid the experiments at a test site for offshore renewable energy, known as Wave Hub. A full description is given by Lopez *et al.* [63]. At the experiment site, shown in figure 5.8, one radar is situated at Pendeen (50.16°N, 5.67°W), operating at approximately 12.355 MHz, and a second radar is situated, approximately 40 km away, at Perranporth (50.33°N, 5.18°W), operating at approximately 12.364 MHz. Radar data from November 2012 are used in this work with hourly measurements available. Each transmitter consists of 4 elements arranged in a square, placed

approximately parallel to the coast, and each phased array receiver consists of 16 antennas. The received signals are digitally beamformed onto a rectangular grid with a resolution of 1 km per cell. This dataset will be referred to as the *Wave Hub HF radar data*.

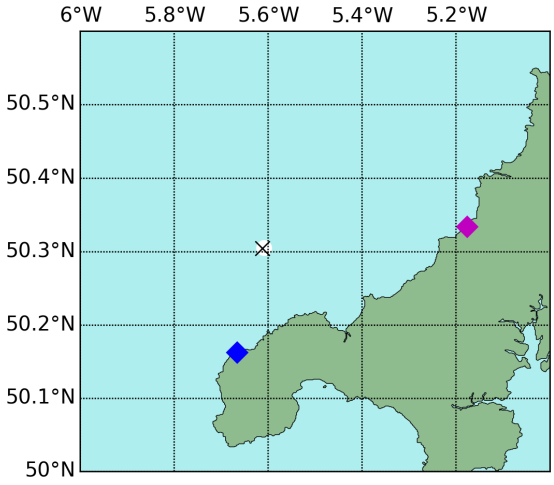

Figure 5.8: Geometry of the Wave Hub HF radar, where the Pendeen radar is shown by the blue diamond (left) and the Perranporth radar by the magenta diamond (right). The wave buoy is shown by the white circle beneath the black cross, which shows the location of the closest available HF radar data.

5.2.1.2 Wave buoy

A directional wave buoy situated in the radar coverage area (50.31°N, 5.61°W), where the water depth is 53 m, is used to (1) provide sea-truth and (2) provide directional spectra to train the neural network. Approximately 20 km from the Pendeen radar and 30 km from the Perranporth radar, measurements from the 'Seawatch Mini II directional buoy' are in 30 minute intervals, and the directional spectra are calculated using a maximum entropy method (see work of Lopez *et al.* [63] for details and figure 1.12 for an example spectrum from the dataset). Two different datasets from the buoy have been used in this study; one for simulating radar Doppler spectra, used to train the neural network, and one for validating the method. The specifications of both datasets are given in table 5.2. The two datasets overlap, every hour, in November 2012, so to avoid bias in the neural network the overlapping data has been removed from the simulation dataset. Note that in the simulations, the buoy data is linearly interpolated to calculate the radar cross section.

	Simulation	Validation
Dates	01/09/2012-20/12/2012	01/11/2012-30/11/2012
Time resolution	30 minutes (with data overlapping the validation set removed)	60 minutes
Frequency resolution	0.0078 Hz in [0-1 Hz] (129 measurements)	0.0078 Hz in [0-1 Hz]
Directional resolution	0.22 rads in [0-2π] (30 measurements)	0.07 rads in [0-2π] (90 measurements)
Data points	4830	648

Table 5.2: Specifications of the wave buoy datasets.

5.2.1.3 WaveWatch III

Wave Watch III data, or WW3 data, as introduced in section 1.2.4, from the IOWAGA database [49], is used in this experiment, alongside the wave buoy data, to simulate Doppler spectra. This particular dataset provides partition parameters for significant waveheight, peak period and wave direction, on a grid with resolution $\sim$3 km. Data is available at a 3 hourly resolution, for January 2010-December 2012, although there are some gaps. A total of 7058 directional spectra have been modelled using the WW3 data, where a Pierson Moskowitz model with $\cos^{2s}$ directional spreading (where $s = 2$), has been used.

5.2.2 Experiment Details

5.2.2.1 Single-location Neural Network (SLNN)

In order to validate the method, the location of the simulation is set to the position nearest to the wave buoy where operational radar data is available. At this position, the beam angles are $\varphi_1 = 15^\circ$ and $\varphi_2 = 264^\circ$, and the ocean depth is 53 m.

In training and testing the ANN, Doppler spectra simulated using both the WW3-modelled and wave buoy-measured directional spectra are included in the dataset. Both datasets are used as the larger the training set is, the most robust the algorithm will be. After filtering by the SNR limit, a total of 4804 training examples were available which were then split into 66%/33% training/test sets for the learning phase. After some experimenting, the values shown in table 5.3 were chosen for a genetic algorithm to search through. In this experiment, as well as the other neural network inversion experiments in this work, the number of nodes in each layer are equal; this is to limit the number of possible combinations that can occur.

Number of Nodes	[179, 256, 512, 880]
Number of Layers	[6, 7, 8, 9]
Minimising Algorithm	[RMSProp, Adam]
Activation Function	[elu, relu]
Number of Iterations	[2500, 3000, 3500]

Table 5.3: The sets of parameters for the genetic algorithm to search through, for the SLNN.

5.2.2.2 Multi-location Neural Network (MLNN)

For the MLNN, the experiment has been carried out on a relatively small scale, where 9 locations - including the location nearest to the wave buoy with available radar data - have been chosen, as shown in figure 5.9. For the 9 positions, φ_1 ranges between 9° and 42° and φ_2 ranges between 261° and 288°. At each position, Doppler spectra are simulated using the wave buoy and WW3 data at the location nearest to the radar. Post filtering, the data set contained $109,971$ data pairs which were then divided into the training/test sets by a 67%/33% split.

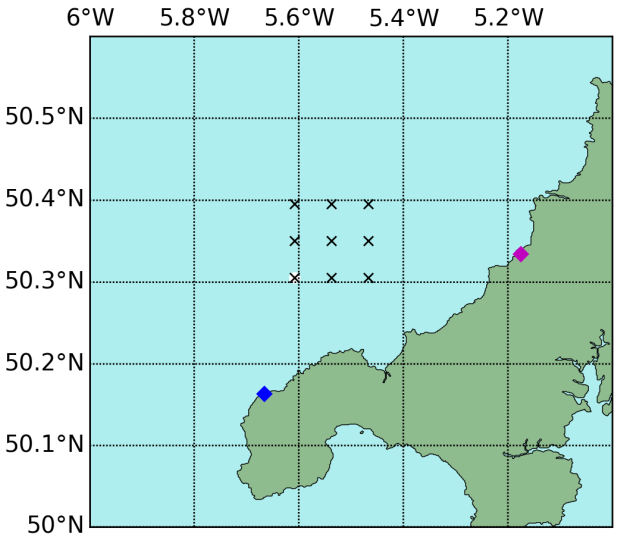

Figure 5.9: Geometry of the MLNN inversion method. For the Wave Hub HF radar, the Pendeen radar is shown by the blue diamond (left) and the Perranporth radar by the magenta diamond (right). The locations of the 9 radar data points, where the neural network is trained, are shown by the black crosses and the wave buoy is shown by the white circle, coinciding with the bottom left radar data location.

Similarly to the SLNN, some experimenting was carried out to decide on the parameters for the genetic algorithm. The resulting parameters are shown in table 5.4.

Number of Nodes	[444, 497, 512, 666, 701, 768, 800, 999]
Number of Layers	[4, 5, 6, 7, 8, 9]
Minimising Algorithm	[RMSProp, Adam]
Activation Function	[elu, relu]
Number of Iterations	[2000, 2500, 3000, 3500]

Table 5.4: The sets of parameters for the genetic algorithm to search through for the MLNN.

5.2.3 Results

To measure the accuracy of the inversion, the values of mean wave direction, θ_m, peak wave direction, θ_p, peak period, t_p, energy period, t_E, and significant waveheight, h_s, defined in section 1.2.3, are calculated from the buoy-measured and algorithm-predicted directional wave spectra. To quantitatively compare the results, the root mean square error (RMSE) and correlation coefficient (CC) of each parameter is calculated and presented for each inversion method. Scatter plots of the predicted ocean parameters against the measured values are given, as well as time series plots of the normalised residuals, to present the results qualitatively.

5.2.3.1 Seaview Inversion Method

The results of the inversion using the Seaview inversion method, for 501 spectra in November 2012, are shown in figures 5.11 and 5.10, and the scatter plot, inparticular, shows that the majority of the waves are travelling from a westerley direction - where swell is arriving from the Atlantic. The accompanying numerical results are given in table 5.7. The accuracy of this method is evident across all parameters, and these results show why this method has been chosen as the benchmark for the neural network algorithm. An example of derived waveheights and mean wave directions across the whole radar coverage area, for a sample date, is shown in figure 5.12, where high resolution detail is clear, in both θ_m and h_s.

In figures 5.11 and 5.10, particularly for the values of θ_m and θ_p, the anomalous results appearing around 16/11/2012 are due to low seas. In these cases, the linearisation struggles and as such, the results are usually filtered out when the software is operational.

5.2.3.2 Single-location Neural Network Inversion Method

For the SLNN, the genetic algorithm was run for a total of 96 hours, on a GPU, in its search for the optimal neural network parameters. The algorithm tested 173 combinations before the parameters were chosen as summarised in table 5.5. The numerical results for the training

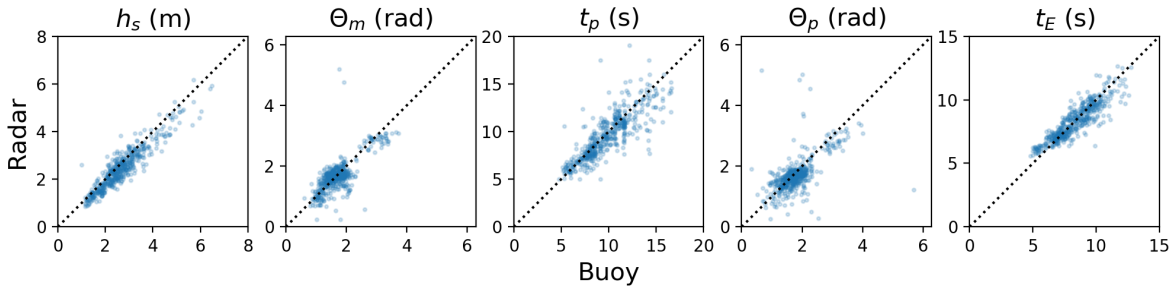

Figure 5.10: Scatter plots showing the results of the Seaview inversion on the Wave Hub HF radar data in November 2012. The wave buoy data, for the same period, is shown on the x axis of each plot and the inverted radar data is on the y axis.

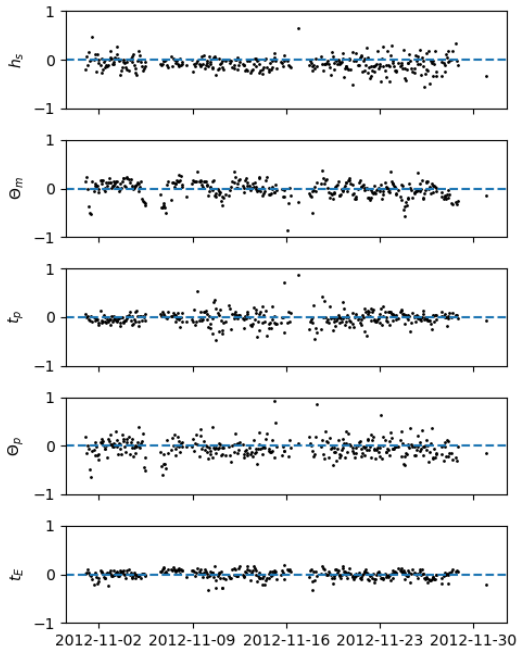

Figure 5.11: Time series plots, for November 2012, showing the residuals of the Seaview inversion on the Wave Hub HF radar data. In each plot, the residual has been divided by the mean of the relevant parameter (which is also shown in table 5.7).

and test sets are given in table 5.6 and scatter plots are shown in figure 5.13. The results show a strong correlation between the simulated and predicted values of each ocean parameter.

The results of the trained neural network, when applied to the Wave Hub HF radar data, are shown in table 5.8. The monthly comparisons of the ocean spectrum parameters are shown in figures 5.14 and 5.15. Note that for this inversion method there are more available radar data than the Seaview method due to a difference in the SNR restriction levels, however, a comparison of the same dataset is given in table 5.7. The results show good correlation between the predicted and measured values of each ocean parameter for both the wave buoy

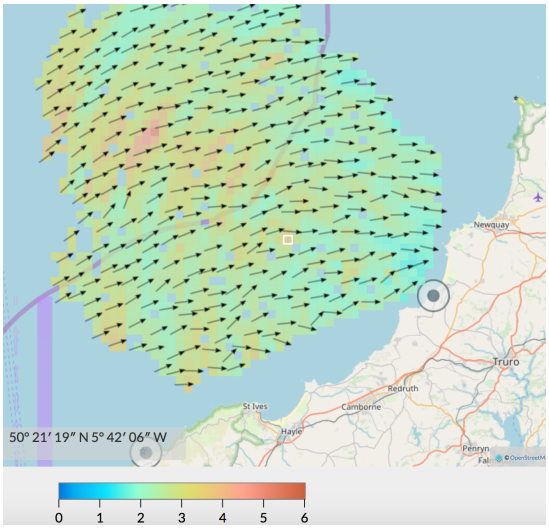

Figure 5.12: Example of whole field inversion, for 20 November 2012 at 03:00, using the Seaview inversion method on the Wave Hub HF radar data. Significant waveheight, measured in metres, is shown by the background colour of each cell and the mean wave direction is shown by the black arrows.

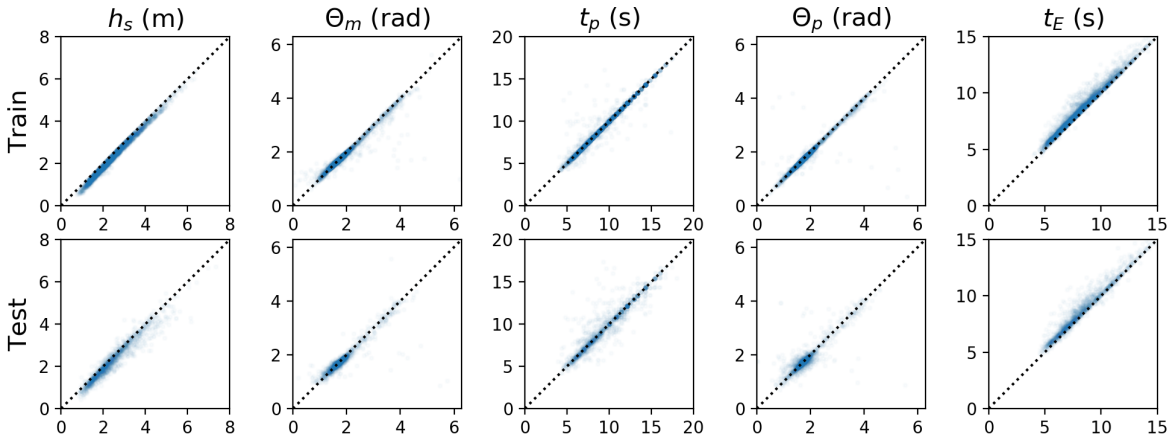

Figure 5.13: Scatter plots showing the results of the SLNN on the training (top) and test (bottom) datasets. The simulated values are shown on the x axes and the predicted values on the y axes.

and the Seaview inversion; the derived values of θ_m are particularly encouraging, with the same westerley wave systems apparent, as in the Seaview inversion, however, on the other hand, t_E appears to be overestimated. Interestingly, the numerical comparison of the SLNN and Seaview inversions, for the same dates, does not affect the results much indicating that the SLNN is performing well on the data with a lower SNR.

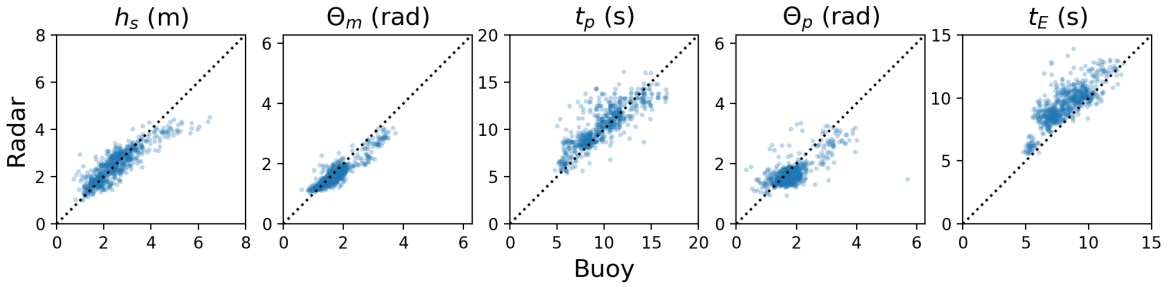

Figure 5.14: Scatter plots showing the results of the SLNN inversion on the Wave Hub HF radar data in November 2012. The wave buoy data, for the same period, is shown on the x axis of each plot and the inverted radar data is on the y axis.

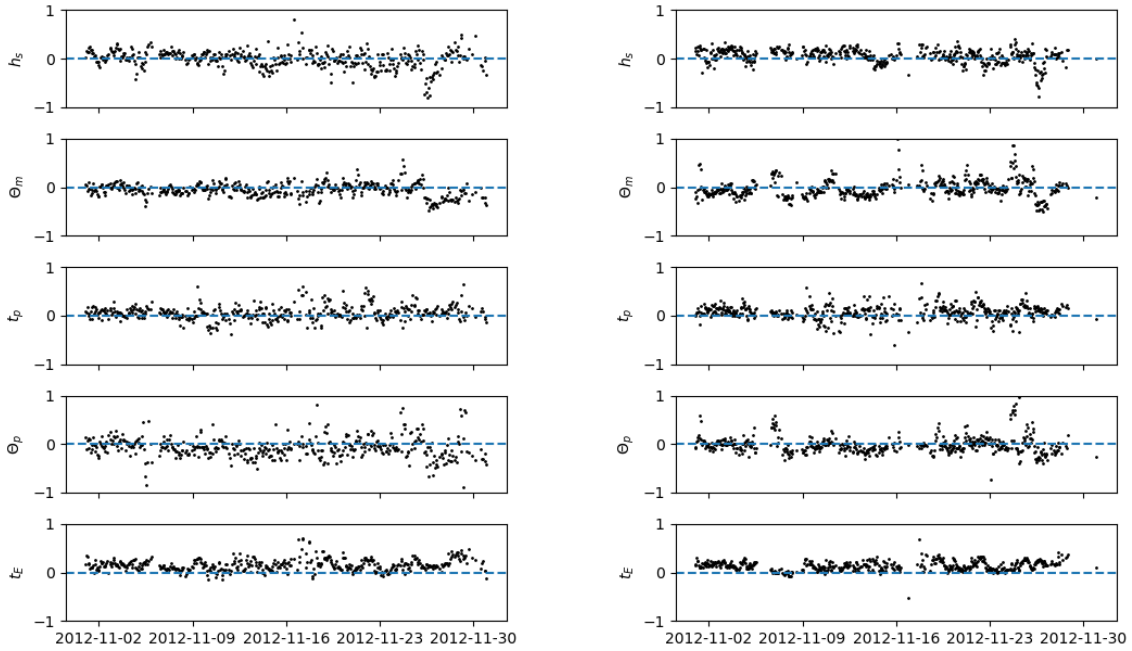

(a) SLNN vs. wave buoy

(b) SLNN vs. Seaview

Figure 5.15: Time series plots, for November 2012, showing the residuals of the SLNN inversion on the Wave Hub HF radar data. Residuals of the SLNN-predictions compared with both the wave buoy data and Seaview inversion predictions are shown, for comparison. In each plot, the residuals have been divided by the mean of the relevant parameter (which are given in tables 5.8 and 5.7 for the wave buoy measurements and Seaview inversion, respectively).

5.2.3.3 Multi-location Neural Network Inversion Method

For the MLNN inversion, the genetic algorithm was, similarly to the SLNN, run for a total of 96 hours on a GPU. The algorithm tested 67 combinations before the parameters were chosen as summarised in table 5.5. The results of the inversion, when applied to the training

and test sets, are shown numerically in table 5.6 and visually in figure 5.16.

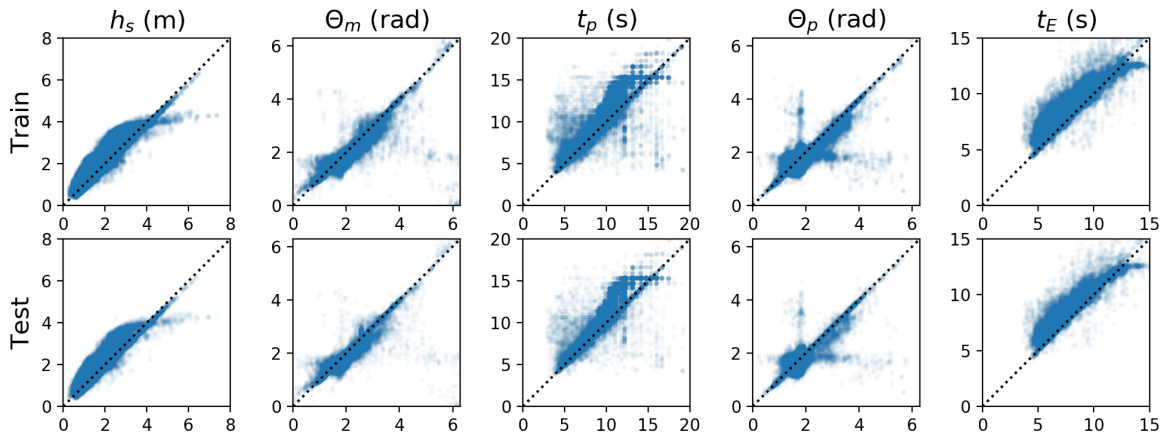

Figure 5.16: Scatter plots showing the results of the MLNN on the training (top) and test (bottom) datasets. The simulated values are shown on the x axis and the predicted values on the y axis.

The results of the trained neural network, when applied to the Wave Hub HF radar data, are shown in table 5.8; the results of the direct comparison with the Seaview method are shown in table 5.7. The monthly comparisons of the chosen ocean spectrum parameters are shown in figures 5.17 and 5.18.

An example of derived waveheights and mean wave direction for the 9 trained locations is shown in figure 5.19; the date and time of this example is the same as the Seaview inversion example in figure 5.12. The map, seen in figure 5.20, shows the results of the MLNN inversion at locations it has not been trained at, for significant waveheight and mean wave direction. The values of θ_m are all very similar, in contrast to the more varied derived values from the Seaview inversion. A possible reason for this is that in training the neural network, the algorithm got stuck in a local minimum and learned to predict the average values for θ_m and θ_p. This is further suggested by the results of the inversion of the entire dataset, shown in figure 5.17, where θ_p, in particular, seems inclined to predict the mean value of the dataset. To counter this, a training dataset with more varied locations could be used and perhaps a larger neural network would also be beneficial.

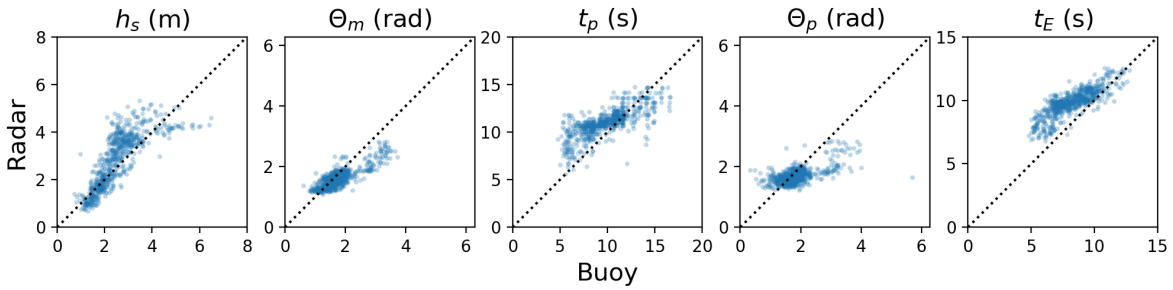

Figure 5.17: Scatter plots showing the results of the MLNN inversion on the Wave Hub HF radar data in November 2012. The wave buoy data, for the same period, is shown on the x axis of each plot and the inverted radar data is on the y axis.

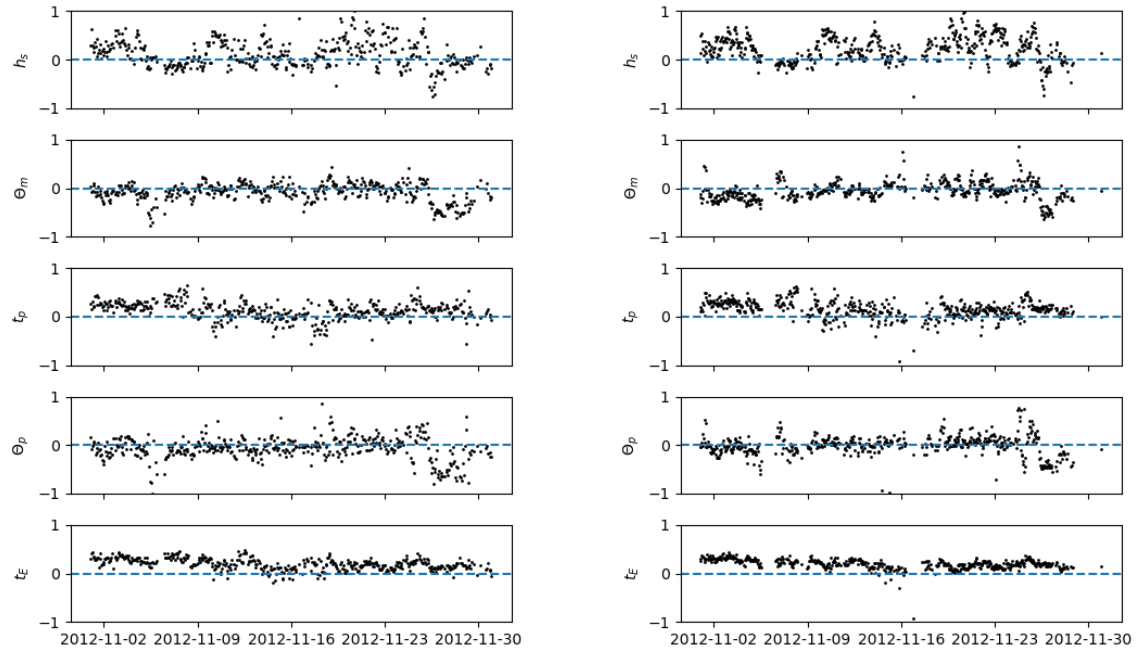

(a) MLNN vs. wave buoy

(b) MLNN vs. Seaview

Figure 5.18: Time series plots, for November 2012, showing the residuals of the MLNN inversion on the Wave Hub HF radar data. Residuals of the MLNN-predictions compared with both the wave buoy data and Seaview inversion predictions are shown, for comparison. In each plot, the residuals have been divided by the mean of the relevant parameter (which are given in tables 5.8 and 5.7 for the wave buoy measurements and Seaview inversion, respectively).

§ 5.3 Bistatic HF Radar Neural Network Inversion

5.3.1 Experiment Details

In this section, two single-location neural networks are trained to invert two bistatic HF radar datasets, $\sigma_B(\omega)$. They are defined as:

	SLNN	MLNN
Number of Layers	8	9
Number of Nodes	880	999
Minimising Algorithm	Adam	Adam
Activation Function	elu	relu
Number of Iterations	3000	3000

Table 5.5: The hyperparameters chosen by genetic algorithms for the SLNN and MLNN inversion methods.

	SLNN				MLNN				Data Statistics			
	Train		Test		Train		Test		Train		Test	
	CC	RMSE	CC	RMSE	CC	RMSE	CC	RMSE	Mean	SD	Mean	SD
h_s	1.0	0.18	0.96	0.31	0.9	0.44	0.9	0.44	2.47	0.96	2.45	0.96
θ_m	0.96	0.15	0.91	0.19	0.86	0.28	0.87	0.28	1.89	0.65	1.85	0.61
t_p	0.98	0.52	0.94	1.03	0.87	1.69	0.86	1.69	9.36	2.81	9.60	2.89
θ_p	0.95	0.16	0.88	0.26	0.82	0.32	0.82	0.33	1.90	0.64	1.85	0.61
t_E	0.99	0.54	0.97	0.63	0.91	1.12	0.91	1.12	08.14	2.07	8.28	2.12

Table 5.6: Numerical results of the SLNN and MLNN inversion methods, on the training and test datasets. The correlation coefficients (CC) and root mean square errors (RMSE) are given. The mean and standard deviation of each parameter, for both the training and test datasets, are also given to provide context for the RMSE values.

	Seaview		SLNN		MLNN		Wave Buoy Statistics	
	CC	RMSE	CC	RMSE	CC	RMSE	Mean	SD
h_s	0.93	0.4	0.88	0.46	0.77	1.49	2.66	0.93
θ_m	0.75	0.36	0.88	0.27	0.68	0.4	1.71	0.52
t_p	0.83	1.47	0.84	1.46	0.77	3.15	9.82	2.52
θ_p	0.59	0.45	0.69	0.4	0.7	0.43	1.80	0.56
t_E	0.85	0.85	0.83	1.48	0.83	2.52	8.26	1.61

Table 5.7: Numerical results of a direct comparison of 501 inversions, of the Seaview, SLNN and MLNN inversion methods, tested on the Wave Hub HF radar data. The correlation coefficients (CC) and root mean square errors (RMSE) are given. The results are for a subset of the Wave Hub data, on which the Seaview inversion results are based. The mean and standard deviation of each parameter, for the wave buoy dataset, are also given to provide context for the RMSE values.

1 the 'bistatic neural network', or BNN, where the data is simulated using the numerical method of section 3.3 and

2 the 'complex bistatic neural network', or CBNN, where the data is simulated using the method of section 3.4, where the radar effects are included.

The first experiment is carried out to see if a neural network can learn the relationship between a Doppler spectrum with a large bistatic angle, and the corresponding directional ocean spec-

	SLNN		MLNN		Wave Buoy Statistics	
	CC	RMSE	CC	RMSE	Mean	SD
h_s	0.87	0.47	0.8	1.51	2.50	0.94
θ_m	0.91	0.26	0.83	0.37	1.78	0.60
t_p	0.82	1.56	0.75	3.18	9.77	2.55
θ_p	0.70	0.42	0.62	0.47	1.85	0.59
t_E	0.80	1.64	0.82	2.53	8.18	1.62

Table 5.8: Numerical results of the SLNN and MLNN inversion methods, tested on the Wave Hub HF radar data. The SLNN and MLNN results are for the inversion of 644 Doppler spectra, where the correlation coefficients (CC) and root mean square errors (RMSE) are given. The mean and standard deviation of each parameter, for the wave buoy dataset, are also given to provide further context for the RMSE values.

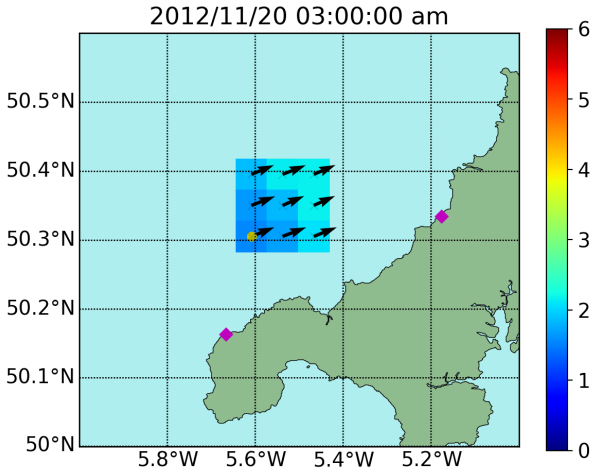

Figure 5.19: Example of MLNN-derived values at each of the nine locations that the MLNN was trained at, on 20 November 2012 at 03:00. Significant waveheight, measured in metres, is shown by the background colour of each cell and the mean wave direction is shown by the black arrows.

trum $S(\mathbf{k})$. The second experiment is to see whether a neural network can learn to accurately invert bistatic Doppler spectra that are contaminated with sidelobes or with a varying Bragg frequency causing first order peak broadening. In both experiments, a monostatic dataset, $\sigma_M(\omega)$, is also simulated using the numerical method of section 3.3 and is used to resolve the wave directions; the input data are of the form $[\sigma_M(\omega), \sigma_B(\omega)]$.

For both neural networks, the resulting algorithm will be tested on the bistatic WERA data described in section 3.2.1. The results will then be validated using the directional wave buoy data (at the same location) described in section 3.2.2. Four days of overlapping radar and buoy data have been obtained in July 2012, however the SNR of the second order bands in the radar data was too low, at the location of the wave buoy, to get meaningful results. An

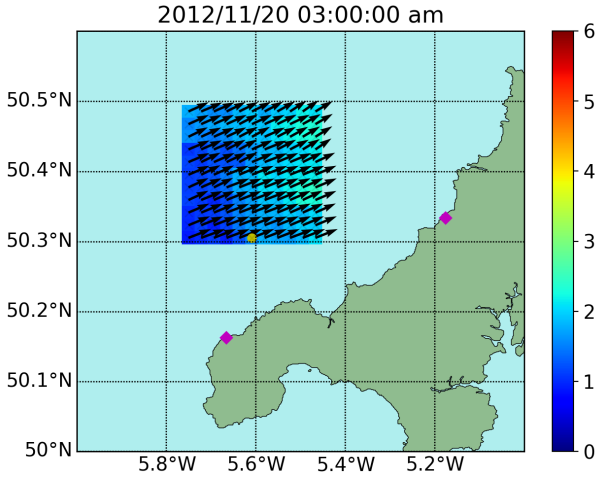

Figure 5.20: Example of a whole field inversion, for 20 November 2012 at 03:00, using the MLNN inversion method, where Doppler spectra from untrained locations have also been inverted. Significant waveheight, measured in metres, is shown by the background colour of each cell and the mean wave direction is shown by the black arrows.

example of a Doppler spectrum from the wave buoy location is shown in figure 5.21(a). At this location, which is shown in figure 5.22, the bistatic angle is $\sim 43^\circ$ which, due to the $\cos^4 \varphi_{bi}$ factor in the second order radar cross section (equation 3.2), is the likely cause of the low SNR spectra. Therefore, a location 9.98 km away from the wave buoy, shown in figure 5.22, has been used to validate the method instead, where the SNR is adequate (see figure 5.21(b) for an example of a Doppler spectrum measured at this location). In using this location to validate the method, we must assume that the ocean spectrum is stationary between the two locations and treat the results with caution.

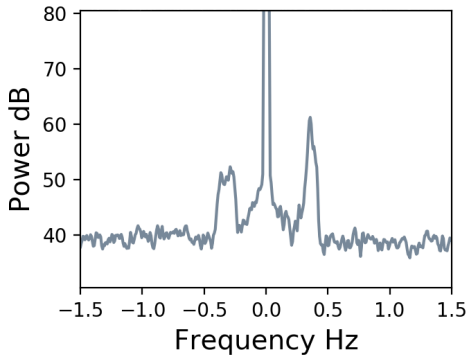

(a) Spectrum measured at the location closest to the wave buoy, at a bistatic range of 11.7 km and a beam direction of 202°.

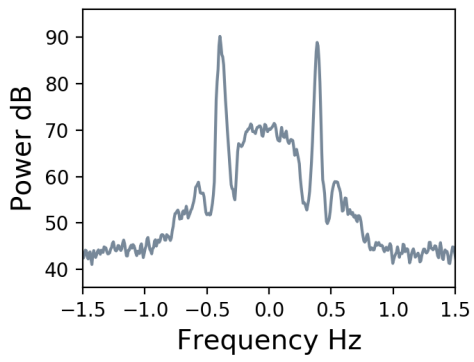

(b) Spectrum measured at the test location, where the bistatic range is 19.2 km and the beam direction is 190°.

Figure 5.21: Bistatic Doppler spectra from the bistatic WERA dataset, described in section 3.2.1, on 9$^{\text{th}}$ July 2014 at 04:01.

To simulate the Doppler spectra for the training data of both neural networks, the locations of the transmitter and receiver are retained, as shown in figure 5.22, however, an imaginary receiver has been added at the same place as the transmitter to resolve the directional ambiguity, operating in monostatic mode. Consequently, in order to test the neural network on the bistatic WERA data, a monostatic data set has been simulated, to accompany the measured bistatic data, using the directional CANDHIS wave buoy spectra as the input. The scatter geometry for both monostatic and bistatic modes is shown in figure 5.23, where $\varphi_M = 144.4^\circ$ and $R_M = 14.3$ km for the monostatic radar and $\varphi_B = 190^\circ$ and $R_B = 19.2$ km for the bistatic radar.

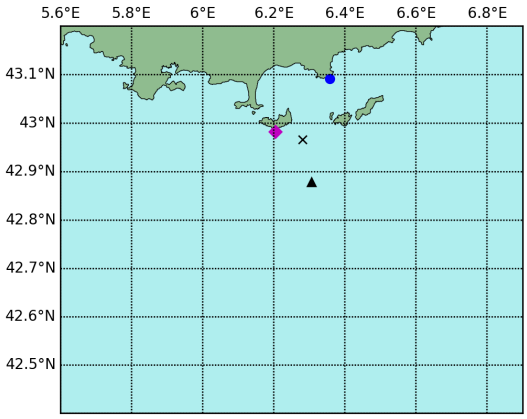

Figure 5.22: Geography of the bistatic neural network experiments. The radar on the left, shown by the pink diamond, both transmits and receives signals (in monostatic mode). The radar on the right, depicted by the blue circle, receives bistatic scatter from the transmitter. The testing location is shown by the black triangle and the location of the wave buoy is shown by the black cross.

In order to compare the neural network performance on the two differently simulated bistatic datasets, the same values for $S(\mathbf{k})$ are used as input to both simulation methods. To simulate $S(\mathbf{k})$, the WW3 dataset described in section 3.2.3 is used. A total of 4556 Doppler spectra, during 2013 - 2016, were simulated using both methods, where single parameters for h_s, t_p, θ_m and s were input to a Pierson Moskowitz model with a $\cos^{2s}$ directional spreading model. After analysing the wave buoy and Pierson Moskowitz modelled wave spectra for the validation period, the overlapping data have not been removed as they were deemed sufficiently different and hence would not influence the results. For the training set used to train the CBNN, time series were generated exactly as described in section 3.4 and they were then beamformed to obtain the Doppler spectrum nearest to the location chosen in the experiment.

Post filtering, with a 10 dB SNR minimum, there were 4095 data pairs for training the BNN and 4496 pairs for training the CBNN. For both experiments, the simulated data pairs were

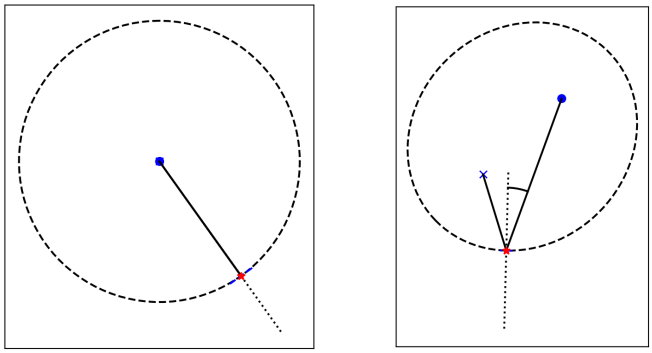

(a) Monostatic (b) Bistatic

Figure 5.23: The scattering geometry of the bistatic neural network experiments. In both figures, the receiver is shown by the blue circle and, for the bistatic radar, the transmitter is shown by the blue cross. The scatter point is shown by the red star and the Bragg bearing is shown as the straight dotted line intersecting this point. The bistatic angle is also shown in the bistatic figure.

split into 67%/33% training/test sets. Good results were achieved by testing just a few neural networks with varying hyperparameters so a genetic algorithm was not necessary in either case. The parameters chosen for each neural network are given in table 5.9.

	BNN	CBNN
Number of Layers	4	5
Number of Nodes	123	654
Minimising Algorithm	Adam	rmsprop
Activation Function	elu	relu
Number of Iterations	1750	550

Table 5.9: The hyperparameters used for the BNN and CBNN inversions.

5.3.2 Results

Similarly to the SLNN and MLNN results in section 5.2, the values of θ_m, θ_p, t_p, h_s and t_E are derived from the directional ocean spectra output by the neural network. These values are then compared with either the simulated values (for the training and test datasets) or the wave buoy measured values (for the bistatic WERA dataset). Scatter plots show the results qualitatively and the RMSE and CC of each parameter are also given to 2 decimal places.

In the validation of the results, where the bistatic WERA dataset is inverted, a total of 184 spectra were available after the 10 dB SNR filter.

5.3.2.1 Bistatic Neural Network

The results of the BNN inversion for the training and test datasets are shown in figure 5.24 and the numerical results are given in table 5.10. Together, they show that the neural network can accurately invert the simulated Doppler spectra.

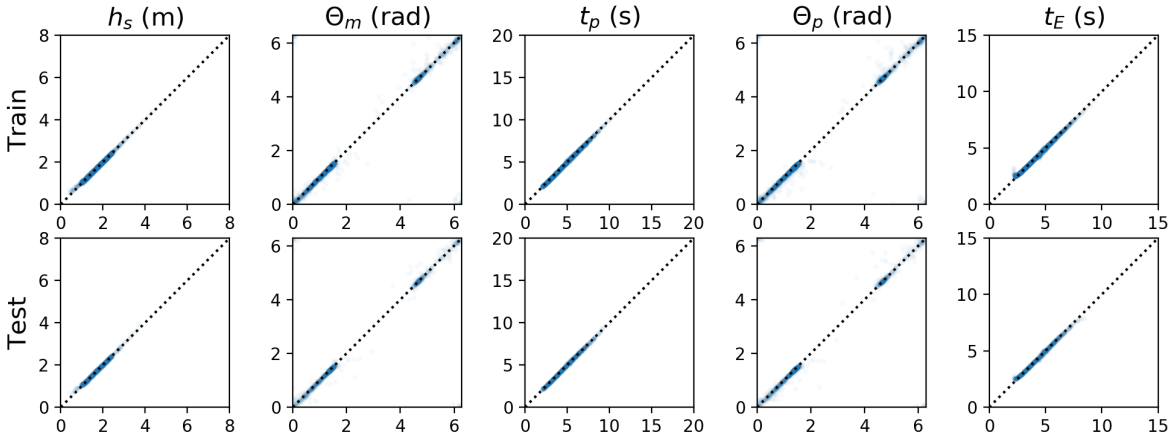

Figure 5.24: Scatter plots showing the results of the BNN on the training (top) and test (bottom) datasets. The simulated values are shown on the x axis and the predicted values on the y axis.

The results of the inversion of the bistatic WERA dataset are shown in figure 5.25, with the accompanying numerical values given in table 5.11. These show that the algorithm is performing reasonably well on real bistatic data, except for θ_p (and in some cases θ_m) which appear to be struggling.

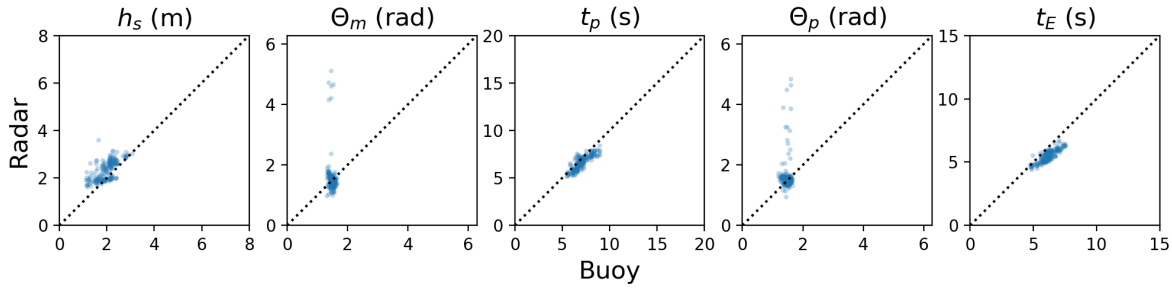

Figure 5.25: Scatter plots showing the results of the BNN on the bistatic WERA data, compared with the directional wave buoy. The wave buoy measured values are shown on the x axis and the predicted values on the y axis.

5.3.2.2 Complex Bistatic Neural Network

The results of the CBNN on the training and test datasets are shown in figure 5.26, with the numerical values given in table 5.10. These show that the algorithm can invert Doppler spectra including the radar effects reasonably well but to not the same level as the BNN inversion.

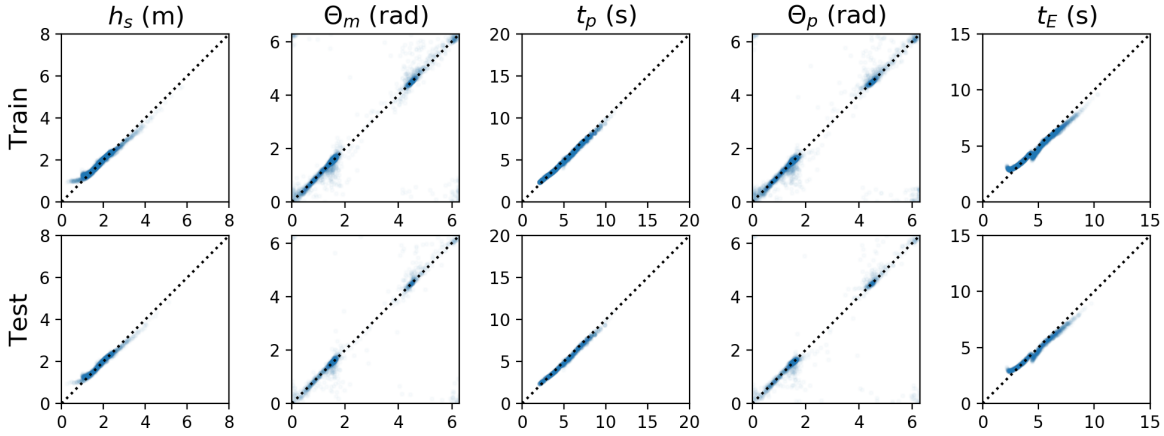

Figure 5.26: Scatter plots showing the results of the CBNN on the training (top) and test (bottom) datasets. The simulated values are shown on the x axes and the predicted values on the y axes.

The results of bistatic WERA data inversion are shown in figure 5.27 and table 5.11. They show increased performance on both θ_m and θ_p, with similar performance in obtaining the other three parameters. However, in predicting h_s, t_p and t_E, the inversion method appears to be predicting a mean value for each parameter; a more varied dataset is necessary to investigate this further. It should be noted that the poor correlation coefficients for both directional parameters result from the small amount of variance in the values measured by the wave buoy. The RMSE values must therefore be taken into account when evaluating the performance of the method.

Summary

In this chapter, inversion methods for obtaining wind direction and wave measurements have been tested. The MLM was used to infer wind direction distributions from bistatic data for the first time and the results were validated with scatterometer data. A neural network was used, also for the first time, to infer the directional wave spectrum and encouraging results were presented. A first experiment was carried out where simulated and high quality radar-measured monostatic data were inverted and the results were compared against those

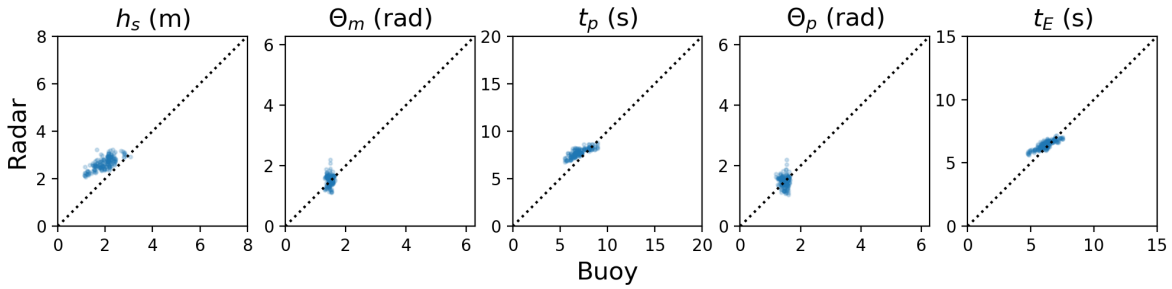

Figure 5.27: Scatter plots showing the results of the CBNN on the bistatic WERA data, compared with the directional wave buoy. The wave buoy measured values are shown on the x axes and the predicted values on the y axes.

	BNN				CBNN			
	Train		Test		Train		Test	
	CC	RMSE	CC	RMSE	CC	RMSE	CC	RMSE
h_s	1.0	0.03	1.0	0.04	0.99	0.12	0.99	0.12
θ_m	0.96	0.1	0.96	0.1	0.94	0.26	0.96	0.27
t_p	1.0	0.05	1.0	0.06	1.0	0.21	1.0	0.22
θ_p	0.96	0.12	0.95	0.12	0.96	0.26	0.96	0.29
t_E	1.0	0.09	1.0	0.09	0.99	0.32	0.99	0.32

Table 5.10: Numerical results of the BNN and CBNN inversion methods, on the training and test datasets. Values for the correlation coefficient (CC) and root mean square error (RMSE) are given to 2 decimal places.

	BNN		CBNN		Wave Buoy Statistics	
	CC	RMSE	CC	RMSE	Mean	SD
h_s	0.64	0.5	0.72	0.75	1.96	0.4
θ_m	-0.18	0.57	0.04	0.18	1.5	0.07
t_p	0.84	0.6	0.81	0.9	7.04	0.82
θ_p	-0.02	0.57	-0.05	0.21	1.47	0.1
t_E	0.85	0.74	0.85	0.46	6.17	0.62

Table 5.11: Numerical results of the BNN and CBNN inversion methods, tested on the bistatic WERA HF radar data. The correlation coefficients (CC) and root mean square errors (RMSE) are given to 2 decimal places.

obtained by the well established Seaview method. A second experiment was carried out, where simulated and - for the first time - radar-measured bistatic data (along with simulated monostatic data) were inverted. Radar effects were included in the simulations and it was shown that a neural network can indeed learn to invert such radar Doppler spectra and consequently, improve the results.

Chapter 6

Discussion and Conclusion

§ 6.1 Conclusions

In the introduction, the four research aims of this thesis were set:

1 To derive an expression for the bistatic radar cross section of the ocean surface which reduces to the monostatic expression of Barrick [5][7], when $\theta = 0$.

2 To model bistatic radar data where the radar effects are included.

3 To infer values of ocean surface parameters - namely wind direction and directional wave spectrum information - from bistatic radar data.

4 To see whether machine learning, in particular, artificial neural networks, can be used to estimate ocean surface parameters from HF radar data.

Aim (1) was addressed in Chapter 2, where the bistatic radar cross section was derived, before the numerical solution was presented in Chapter 3. A comparison of simulated bistatic Doppler spectra with real measured bistatic Doppler spectra reinforced the differences highlighted by Grosdidier *et al.* [29], for scenarios where the radar effects cannot be ignored. To counter this, and to address Aim (2), a new simulation method was proposed to model bistatic HF radar data including the radar effects, where the resulting simulated spectra were more similar to the measured radar data.

To satisfy Aim (3), methods for inverting bistatic radar Doppler spectra were described in Chapter 4. Existing inversion methods for obtaining currents, winds and waves were outlined and a new method which uses a neural network to invert radar Doppler spectra for the directional wave spectra was proposed. In Chapter 5, the maximum likelihood method of

Wyatt *et al.* [108] was used to invert real bistatic data to obtain wind direction measurements, which, when compared with ASCAT scatterometer data, gave encouraging results. This experiment highlighted the difficulty of locating the first order peaks when there is significant first order spreading due to a varying Bragg frequency in the measurement location and/or sidelobes; a crude algorithm was implemented which examines each pair of peaks, separated by a distance of $2\omega_B$, and then picks the pair with the highest combined total amplitude. The resulting wind directions were mostly consistent but there were a number of erroneous directions chosen, which is likely to be due to the difficulty in identifying the appropriate peaks. Furthermore, the larger the value of ω_B, the larger the Bragg wave and this could be a potential issue in complex ocean systems.

Aim (4) was covered in Chapter 5, when it was shown that a neural network can be used to invert HF radar Doppler spectra to obtain the associated directional wave spectra. Four neural networks were trained using HF radar simulated for: (1) a monostatic radar in a single location, (2) a monostatic radar in multiple locations (3) a bistatic radar in a single location and (4) a bistatic radar in a single location, where radar effects were included. Key ocean statistics, namely mean and peak wave direction, energy period, peak wave period and significant waveheight, were estimated by the neural network inversion and, in each case, were then compared with the same parameters from a wave buoy.

The single-location neural network, or SLNN, inversion, showed good agreement with the wave buoy, which shows the potential of machine learning algorithms in the field of remote sensing using HF radar. The numerical comparison of the neural network and Seaview inversion methods in table 5.8, shows that the results for the SLNN and Seaview methods are similar, with the SLNN performing better on θ_m and θ_p, approximately equal on t_p and worse on h_s and t_E. At sea states above approximately 4.5 m, the neural network is underestimating h_s and the network seems to constantly overestimate the value of t_E.

The multi-location neural network, or MLNN, inversion, although providing encouraging results, does not perform as well on the real data as the SLNN does. For the inversion results on the subset of the data which are directly comparable with the Seaview inversion, only θ_p is more accurately predicted. The average correlation coefficient is 0.75 compared with 0.83 for the SLNN and 0.79 for the Seaview inversion. The average root mean square error for the MLNN is 1.6, compared with 0.81 for the SLNN and 0.71 for the Seaview inversion. The results for the training/testing dataset inversions are worse than for the SLNN too. This could be because only nine locations were trained in the neural network which were not far apart. Perhaps training data simulated at locations further apart would help the neural network create a better model of the relationship between the beam angles and the Doppler spectra. Or

perhaps including more locations with fewer data at each would be beneficial. Fundamentally, more work must be done to accurately invert data across a larger expanse of the ocean using this neural network method.

The two neural networks trained to invert bistatic HF radar data, both with and without radar effects, gave excellent results on the training and test data. This showed that a neural network can successfully invert bistatic data, both when the bistatic radar cross section does or does not hold. When the algorithms were tested on measured bistatic HF radar data, together with simulated monostatic data, both neural networks derived the values of h_s, t_p and t_E adequately. The neural network trained *without* the radar effects, struggled to measure the directions of the wave spectra, however, improvement was seen when the radar effects were included in the training process. The wave buoy used to validate the estimates was, however, in a different location and therefore, these results must be treated with caution.

§ 6.2 Future Work and Limitations

6.2.1 Neural Network Inversion Method

A limitation of the existing inversion methods is also apparent in the neural network inversion method. The perturbation theory of Rice [78], used in Chapter 2 to derive the radar cross section, assumes small slopes compared to radar wavelength. Therefore, for high seas with large significant waveheight, the theory breaks down and the simulations that the neural network is trained on do not represent the real data well. This is apparent in the results of the neural network inversion, for the higher values of h_s. A modification to the simulation, similar to that used by Wyatt *et al.* [106], could be made for significant waveheights over a given threshold; this is a possibilty for the future.

More work must also be done on successfully including the radar beam angle in the neural network algorithms. The main advantage of HF radar is its ability to provide measurements across a larger expanse of the ocean, as opposed to the single point measurement of a wave buoy, say. As the neural network inversion works well in a single location, there is no reason why it should not also be able to learn the relationship between φ_1 and φ_2, and the Doppler spectra, to the same level of accuracy. This is seemingly a case of getting the correct neural network architecture and having a big enough dataset for the training process.

There are a number of variables not yet varied in the training phase which may impact the accuracy of the neural network. For instance, the points of the Doppler spectrum 0.6 either side of each Bragg peak were used as the input of the neural network and the effect of varying

this range has not yet been tested. Valuable information may be missed in the training phase or useless information may be being passed in and wasting resources. A convolutional neural network may be more suitable for tackling this issue, and is something to try in the future. Other machine learning methods may also be successful in inverting Doppler spectra, and a comparison of different methods would be interesting.

The high cost of training the neural network, in both time and computing resources, is another limitation. Other methods, such as the Seaview inversion method, require no prior knowledge of the radar data/setup; one just has to set the variables, such as radar frequency and location and then the algorithm is ready to be implemented. As the neural network procedure is dependent on factors such as the noise floor and locations of the radars, simulations and the training process must be carried out for each new radar site. If a radar were to be moved, the whole process must be carried out again meaning a few days of operational downtime would occur. To train a neural network to recognise all different radar frequencies and angles would be theoretically possible, although one would need a large amount of computing power to train a much larger neural network with a vast, varied dataset. On the other hand, once trained, the neural network inversion method is cheap to run, and would provide fast results operationally.

6.2.2 Simulating and Inverting Bistatic Data

The speed of computing a bistatic Doppler spectrum, using the derived bistatic radar cross section, is between 0.2 and 2 seconds, with sufficient resolution. The new proposed method, to simulate Doppler spectra including the radar effects, where over 1000 spectra are simulated, therefore takes around 5 minutes, even when computed in parallel. Considering the large number of Doppler spectra that must be computed for each simulation, this slowness is not surprising, yet there are ways of speeding it up. The individual Doppler spectra would benefit from being simulated in a lower level language such as C, where the readability of the code is sacrificed for speed. This would make it more feasible to simulate an extensive training set for the neural network inversion process, which thus far has only been trained on a few thousand spectra, at most.

Along with the need for more data, more realistic directional spectra should be used in simulating the training set, too. The WW3 data used in both bistatic neural network experiments contained only single ocean parameters and these were used as input to a Pierson Moskowitz model, which is not likely to be appropriate for all times, given the limited fetch in the area, for some directions and the possible presence of swell. Furthermore, it is not realistic to have such 'perfect' ocean spectra; if the neural network was tested on a Doppler spectrum gener-

ated using multi-modal - less perfect and hence more realistic - data, it would likely predict inaccurate results.

Although the bistatic neural network was tested on real HF radar data and validated with a directional wave buoy dataset, the dataset was particularly small (only 4 days) and unvaried. Additionally, a monostatic data set was simulated using the wave buoy data which is not authentic and furthermore, as the SNR was too low in the location of the wave buoy, the location of the test was moved to a location 10 km away so the results may be inaccurate. An ideal future experiment would have a multistatic radar setup, with a directional wave buoy in the coverage area to validate the results (in an area with a sufficient SNR), and directional ocean spectra WW3 model data to simulate the Doppler spectra for the training dataset.

6.2.3 Wind Inversion

The same SNR issue as in the bistatic wave inversion experiment applied in the wind direction inversion experiment in section 5.1, except then, there was ASCAT data available to validate the results. The varying value of φ_{bi} did seem to affect the inversion of the wind directions, though. Care must be taken in interpreting the wind directions as one will measure Bragg waves of different lengths over an area with substantially varying bistatic angles. This may also raise an issue when inverting wind directions from multistatic radar. If the Bragg frequencies in a location are significantly different for the monostatic and bistatic radars, then different Bragg waves will be measured and the dataset used in the maximum likelihood method will not be consistent. More work must be done - specifically using a multistatic radar - to see how much this will affect the inversion. However, in similar situations for monostatic radar setups, where two radars operate on two different frequencies, good results were obtained [102]. On the other hand, there is a possibility that the radar data inversion picked up different features of the wind system, than the ASCAT data showed. This is only speculation though and is not possible to prove at this time, so further studies must be undertaken.

In general, in areas where the bistatic angle is large (when $\varphi_{bi} \to 90°$), the measured Doppler spectra may have to be discarded. Troubled by low SNR and Bragg peak broadening, it has not been possible to invert these data in this work. Other datasets must be analysed to see whether or not this will be possible.

Bibliography

[1] Abascal, A. J. et al. "Application of HF radar currents to oil spill modelling". In: *Marine pollution bulletin* 58.2 (2009), pp. 238–248.

[2] *About CODAR*. 2018. URL: `http://www.codar.com/about.shtml` (visited on 10/26/2018).

[3] *About WERA*. 2018. URL: `http://wera.cen.uni-hamburg.de/WERA.shtml` (visited on 10/29/2018).

[4] Anderson, S. "Directional wave spectrum measurement with multistatic HF surface wave radar". In: *Geoscience and Remote Sensing Symposium, 2000. Proceedings. IGARSS 2000. IEEE 2000 International*. Vol. 7. IEEE. 2000, pp. 2946–2948.

[5] Barrick, D. E. "First-order theory and analysis of MF/HF/VHF scatter from the sea". In: *IEEE Transactions on Antennas and Propagation* 20.1 (1972), pp. 2–10.

[6] Barrick, D. E. "HF radio oceanography - a review". In: *Boundary-Layer Meteorology* 13.1-4 (1978), pp. 23–43.

[7] Barrick, D. E. *Remote Sensing of Sea State by Radar*. 1972.

[8] Barrick, D. E. "The ocean waveheight nondirectional spectrum from inversion of the HF sea-echo Doppler spectrum". In: *Remote Sensing of Environment* 6.3 (1977), pp. 201–227.

[9] Barrick, D. E. "Theory of HF and VHF propagation across the rough sea, 1, The effective surface impedance for a slightly rough highly conducting medium at grazing incidence". In: *Radio Science* 6.5 (1971), pp. 517–526.

[10] Barrick, D. E., Evans, M., and Weber, B. "Ocean surface currents mapped by radar". In: *Science* 198.4313 (1977), pp. 138–144.

[11] Barrick, D. E. and Lipa, B. J. "The second-order shallow-water hydrodynamic coupling coefficient in interpretation of HF radar sea echo". In: *IEEE Journal of Oceanic Engineering* 11.2 (1986), pp. 310–315.

[12] Booij, N., Ris, R., and Holthuijsen, L. H. "A third-generation wave model for coastal regions: 1. Model description and validation". In: *Journal of Geophysical Research: Oceans* 104.C4 (1999), pp. 7649–7666.

[13] Brodtkorb, P. A. et al. "WAFO-a Matlab toolbox for analysis of random waves and loads". In: *The Tenth International Offshore and Polar Engineering Conference*. International Society of Offshore and Polar Engineers. 2000.

[14] Cavaleri, L. et al. "Wave modelling in coastal and inner seas". In: *Progress in Oceanography* 167 (2018), pp. 164–233.

[15] Chapman, R. D. and Graber, H. C. "Validation of HF radar measurements". In: *Oceanography* 10.2 (1997), pp. 76–79.

[16] Conyers, L. B. *Ground-penetrating radar for archaeology*. AltaMira Press, 2013.

[17] Crapper, G. D. *Introduction to water waves*. Ellis Horwood Ltd., 1985.

[18] Creamer, D. B. et al. "Improved linear representation of ocean surface waves". In: *Journal of Fluid Mechanics* 205 (1989), pp. 135–161.

[19] Crombie, D. D. "Doppler spectrum of sea echo at 13.56 Mc./s." In: *Nature* 175.4459 (1955), p. 681.

[20] Donelan, M. A., Hamilton, J, and Hui, W. "Directional spectra of wind-generated ocean waves". In: *Philosophical Transactions of the Royal Society A: Mathematical, Physical and Engineering Sciences* 315.1534 (1985), pp. 509–562.

[21] Dreyfus, G. *Neural networks: methodology and applications*. Springer Science & Business Media, 2005.

[22] Dzvonkovskaya, A. "HF surface wave radar for tsunami alerting: from system concept and simulations to integration into early warning systems". In: *IEEE Aerospace and Electronic Systems Magazine* 33.3 (2018), pp. 48–58.

[23] *EMODnet: bathymetry viewing and download tool*. 2018. URL: `http://portal.emodnet-bathymetry.eu/?menu=19` (visited on 12/14/2018).

[24] *EUMETSAT: ASCAT*. 2018. URL: `www.eumetsat.int` (visited on 01/14/2019).

[25] Forney, R., Roarty, H., and Glenn, S. "Measuring waves with a compact HF radar". In: *OCEANS'15 MTS/IEEE Washington*. IEEE. 2015, pp. 1–5.

[26] Georges, T. M. et al. "Real-time sea-state surveillance with skywave radar". In: *IEEE Journal of Oceanic Engineering* 8.2 (1983), pp. 97–103.

[27] Gill, E. W. and Walsh, J. "High-frequency bistatic cross sections of the ocean surface". In: *Radio Science* 36.6 (2001), pp. 1459–1475.

[28] *Globcurrent*. 2018. URL: `http://www.globcurrent.org/` (visited on 12/14/2018).

[29] Grosdidier, S. et al. "HF bistatic ocean Doppler spectra: simulation versus experimentation". In: *IEEE Transactions on Geoscience and Remote Sensing* 52.4 (2014), pp. 2138–2148.

[30] Gurgel, K.-W., Essen, H.-H., and Kingsley, S. "High-frequency radars: physical limitations and recent developments". In: *Coastal Engineering* 37.3-4 (1999), pp. 201–218.

[31] Gurgel, K.-W. et al. "Wellen Radar (WERA): a new ground-wave HF radar for ocean remote sensing". In: *Coastal Engineering* 37.3 (1999), pp. 219–234.

[32] Gurgel, K.-W., Essen, H.-H., and Schlick, T. "An empirical method to derive ocean waves from second-order Bragg scattering: prospects and limitations". In: *IEEE Journal of Oceanic Engineering* 31.4 (2006), pp. 804–811.

[33] Harlan, J. et al. "National IOOS high frequency radar search and rescue project". In: *OCEANS'11 - MTS/IEEE Kona*. IEEE. 2011, pp. 1–9.

[34] Harris, F. J. "On the use of windows for harmonic analysis with the discrete Fourier transform". In: *Proceedings of the IEEE* 66.1 (1978), pp. 51–83.

[35] Hashimoto, N. "Analysis of the directional wave spectrum from field data". In: *Advances in Coastal and Ocean Engineering* 3 (1997), pp. 103–144.

[36] Hasselmann, K. et al. "Measurements of wind-wave growth and swell decay during the Joint North Sea Wave Project (JONSWAP)". In: *Ergänzungsheft 8-12* (1973).

[37] Hauser, D et al. "Measuring and analysing the directional spectra of ocean waves". In: *COST Action*. Vol. 714. 2005.

[38] Heron, M. L. "The Australian coastal ocean radar network facility". In: *Canadian Conference on Electrical and Computer Engineering*. IEEE. 2009, pp. 23–26.

[39] Heron, M. L. "Tsunami monitoring by HF ocean radar: time and space scales". In: *OCEANS 2007-Europe*. IEEE. 2007, pp. 1–5.

[40] Heron, M. L. and Rose, R. "On the application of HF ocean radar to the observation of temporal and spatial changes in wind direction". In: *IEEE Journal of Oceanic Engineering* 11.2 (1986), pp. 210–218.

[41] Hisaki, Y. "Nonlinear inversion of the integral equation to estimate ocean wave spectra from HF radar". In: *Radio science* 31.1 (1996), pp. 25–39.

[42] Hodgins, D. O. "Remote sensing of ocean surface currents with the SeaSonde HF radar". In: *Spill Science & Technology Bulletin* 1.2 (1994), pp. 109–129.

[43] Holden, G. J. and Wyatt, L. R. "Extraction of sea state in shallow water using HF radar". In: *IEE Proceedings part F: Radar and Signal Processing*. Vol. 139. 2. 1992, pp. 175–181.

[44] Holthuijsen, L. H. *Waves in oceanic and coastal waters*. Cambridge University Press, 2007.

[45] *How to set up a WERA Site*. 2018. URL: `http://wera.cen.uni-hamburg.de/WERA_Guide/WERA_Guide.shtml` (visited on 10/29/2018).

[46] Huang, W. et al. "Measurement of sea surface wind direction using bistatic high-frequency radar". In: *IEEE Transactions on Geoscience and Remote Sensing* 50.10 (2012), pp. 4117–4122.

[47] Hulsmeyer, C. "Hertzian wave projecting and receiving apparatus adapted to indicate or give warning of the presence of a metallic body, such as a ship or a train, in the line of projection of such waves". In: *UK Patent* 13 (1904).

[48] *IMOS Data Portal*. 2018. URL: `https://portal.aodn.org.au/` (visited on 10/29/2018).

[49] *IOWAGA database*. 2018. URL: `https://wwz.ifremer.fr/iowaga/` (visited on 12/14/2018).

[50] Johnstone, D. L. *Second-order electromagnetic and hydrodynamic effects in high-frequency radio-wave scattering from the sea*. Tech. rep. DTIC Document, 1975.

[51] Jordan, E. C. and Balmain, K. G. *Electromagnetic waves and radiating systems*. Prentice-Hall, 1968.

[52] Kingma, D. P. and Ba, J. "Adam: A method for stochastic optimization". In: *arXiv preprint arXiv:1412.6980* (2014).

[53] Kingsley, S. and Quegan, S. *Understanding radar systems*. Vol. 2. SciTech Publishing, 1999.

[54] Kinsman, B. *Wind waves: their generation and propagation on the ocean surface*. Courier Corporation, 1965.

[55] Komen, G. J. et al. *Dynamics and Modelling of Ocean Waves*. Cambridge University Press, 1996.

[56] Kuik, A., Van Vledder, G. P., and Holthuijsen, L. "A method for the routine analysis of pitch-and-roll buoy wave data". In: *Journal of Physical Oceanography* 18.7 (1988), pp. 1020–1034.

[57] Lipa, B. J. "Derivation of directional ocean-wave spectra by integral inversion of second-order radar echoes". In: *Radio Science* 12.3 (1977), pp. 425–434.

[58] Lipa, B. J. "Inversion of second-order radar echoes from the sea". In: *Journal of Geophysical Research: Oceans* 83.C2 (1978), pp. 959–962.

[59] Lipa, B. J. and Barrick, D. E. "Extraction of sea state from HF radar sea echo: Mathematical theory and modeling". In: *Radio Science* 21.1 (1986), pp. 81–100.

[60] Lipa, B. J. and Nyden, B. "Directional wave information from the SeaSonde". In: *IEEE Journal of Oceanic Engineering* 30.1 (2005), pp. 221–231.

[61] Long, A. E. and Trizna, D. B. "Mapping of North Atlantic winds by HF radar sea backscatter interpretation". In: *IEEE Transactions on Antennas and Propagation* 21.5 (1973), pp. 680–685.

[62] Longuet-Higgins, M. S., Cartwright, D. E., and Smith, N. D. "Observations of the directional spectrum of sea waves using the motions of a floating buoy". In: *Ocean Wave Spectra*. 1961, pp. 111–132.

[63] Lopez, G., Conley, D. C., and Greaves, D. "Calibration, Validation, and Analysis of an Empirical Algorithm for the Retrieval of Wave Spectra from HF Radar Sea Echo". In: *Journal of Atmospheric and Oceanic Technology* 33.2 (2016), pp. 245–261.

[64] Lucas, C. and Soares, C. G. "On the modelling of swell spectra". In: *Ocean Engineering* 108 (2015), pp. 749–759.

[65] Marconi, G. "Radio telegraphy". In: *Journal of the American Institute of Electrical Engineers* 41.8 (1922), pp. 561–570.

[66] Maresca Jr, J. W. and Georges, T. "Measuring rms wave height and the scalar ocean wave spectrum with HF skywave radar". In: *Journal of Geophysical Research: Oceans* 85.C5 (1980), pp. 2759–2771.

[67] Mathew, T. E. and Deo, M. C. "Inverse estimation of wind from the waves measured by high-frequency radar". In: *International Journal of Remote Sensing* 33.10 (2012), pp. 2985–3003.

[68] *Mediterranean Institute of Oceanography*. 2013. URL: `http://mio.pytheas.univ-amu.fr` (visited on 12/14/2018).

[69] *Mediterranean Institute of Oceanography - MOOSE HF Radar*. 2013. URL: `http://hfradar.univ-tln.fr/HFRADAR/` (visited on 01/07/2019).

[70] Meischner, P. *Weather radar: principles and advanced applications*. Springer Science & Business Media, 2005.

[71] Mitchell, M. *An introduction to genetic algorithms*. MIT press, 1998.

[72] Moskowitz, L. "Estimates of the power spectrums for fully developed seas for wind speeds of 20 to 40 knots". In: *Journal of Geophysical Research* 69.24 (1964), pp. 5161–5179.

[73] *National Center for Archiving Swell*. URL: `http://candhis.cetmef.developpement-durable.gouv.fr/` (visited on 02/23/2019).

[74] *Neptune Radar: PISCES*. 2018. URL: `http://www.neptuneradar.net/Pisces.html` (visited on 10/29/2018).

[75] Nyden, B. et al. "HF radar bistatic measurement of surface current velocities: Drifter comparisons and radar consistency checks". In: *Remote Sensing* 1.4 (2009), pp. 1190–1211.

[76] Paduan, J. D. and Washburn, L. "High-frequency radar observations of ocean surface currents". In: *Annual review of marine science* 5 (2013), pp. 115–136.

[77] Pierson, W. J. and Moskowitz, L. "A proposed spectral form for fully developed wind seas based on the similarity theory of SA Kitaigorodskii". In: *Journal of Geophysical Research* 69.24 (1964), pp. 5181–5190.

[78] Rice, S. O. "Reflection of electromagnetic waves from slightly rough surfaces". In: *Communications on Pure and Applied Mathematics* 4.2-3 (1951), pp. 351–378.

[79] Shen, W. et al. "Wind-speed inversion from HF radar first-order backscatter signal". In: *Ocean Dynamics* 62.1 (2012), pp. 105–121.

[80] Silva, M. T. et al. "An Improved Nonlinear Extraction of Directional Ocean Wave Spectrum from Bistatic HFSWR Using Tikhonov Regularization in Hilbert Scales". In: *OCEANS 2018 MTS/IEEE Charleston*. 2018, pp. 1–6.

[81] Skolnik, M. I. *Introduction to Radar Systems*. 1981.

[82] Skolnik, M. I. *Radar handbook*. 1970.

[83] Steele, J. H., Turekian, K. K., and Thorpe, S. A. *Encyclopedia of ocean sciences: Volume 5*. 2010.

[84] Stewart, R. H. and Barnum, J. R. "Radio measurements of oceanic winds at long ranges: An evaluation". In: *Radio Science* 10.10 (1975), pp. 853–857.

[85] Stewart, R. H. and Joy, J. W. "HF radio measurements of surface currents". In: *Deep Sea Research and Oceanographic Abstracts*. Vol. 21. 12. 1974, pp. 1039–1049.

[86] Stratton, J. A. *Electromagnetic theory*. John Wiley & Sons, 2007.

[87] Taylor, A. H., Young, L. C., and Hyland, L. A. *System for detecting objects by radio*. US Patent. 1934.

[88] *Tensorflow*. 2018. URL: `www.tensorflow.org` (visited on 02/01/2019).

[89] Thomas, J. B. *An introduction to statistical communication theory*. Wiley, 1969.

[90] Tieleman, T. and Hinton, G. "Lecture 6.5-rmsprop: Divide the gradient by a running average of its recent magnitude". In: *COURSERA: Neural networks for machine learning* 4.2 (2012), pp. 26–31.

[91] Tolman, H. L. "A mosaic approach to wind wave modeling". In: *Ocean Modelling* 25.1-2 (2008), pp. 35–47.

[92] Tolman, H. L. et al. "User manual and system documentation of WAVEWATCH III TM version 3.14". In: *Technical note, MMAB Contribution* 276 (2009).

[93] Trevett, J. W. *Imaging radar for resources surveys*. Springer Science & Business Media, 1986.

[94] Tucker, M. J. and Pitt, E. G. *Waves in ocean engineering*. 2001.

[95] Vera, A. et al. "The use of radar satellite for hydrocarbon exploration in Venezuela". In: *The Use and Applications of ERS in Latin America, Proceedings of an International seminar held in Vina del Mar, Chile*. Vol. 405. 12. 1997, pp. 143–150.

[96] Vincent, L. and Soille, P. "Watersheds in digital spaces: an efficient algorithm based on immersion simulations". In: *IEEE Transactions on Pattern Analysis & Machine Intelligence* 13.6 (1991), pp. 583–598.

[97] Wahle, K. and Stanev, E. "Consistency and complementarity of different coastal ocean observations: A neural network-based analysis for the German Bight". In: *Geophysical Research Letters* 38.10 (2011).

[98] Weber, B. L. and Barrick, D. E. "On the nonlinear theory for gravity waves on the ocean's surface. Part I: Derivations". In: *Journal of Physical Oceanography* 7.1 (1977), pp. 3–10.

[99] Whelan, C. and Hubbard, M. "Benefits of multi-static on HF Radar networks". In: *OCEANS'15 MTS/IEEE Washington*. 2015, pp. 1–5.

[100] Willis, N. J. *Bistatic radar*. SciTech Publishing, 2005.

[101] Wyatt, L. R. personal communication. June 16, 2014.

[102] Wyatt, L. R. personal communication. Mar. 20, 2019.

[103] Wyatt, L. R. "A relaxation method for integral inversion applied to HF radar measurement of the ocean wave directional spectrum". In: *International Journal of Remote Sensing* 11.8 (1990), pp. 1481–1494.

[104] Wyatt, L. R. “Measuring the ocean wave directional spectrum ‘First Five’ with HF radar”. In: *Ocean Dynamics* 69.1 (2019), pp. 123–144.

[105] Wyatt, L. R. “Wave and Tidal Power measurement using HF radar”. In: *OCEANS 2007-Europe*. 2007, pp. 1–5.

[106] Wyatt, L. R., Green, J. J., and Middleditch, A. “HF radar data quality requirements for wave measurement”. In: *Coastal Engineering* 58.4 (2011), pp. 327–336.

[107] Wyatt, L. R., Green, J. J., and Middleditch, A. “Wave, current and wind monitoring using HF radar”. In: *Current Measurement Technology, 2005. Proceedings of the IEEE/OES Eighth Working Conference on*. IEEE. 2005, pp. 53–57.

[108] Wyatt, L. R., Ledgard, L., and Anderson, C. “Maximum-likelihood estimation of the directional distribution of 0.53-Hz ocean waves”. In: *Journal of Atmospheric and Oceanic Technology* 14.3 (1997), pp. 591–603.

[109] Wyatt, L. R. et al. “Factors affecting the accuracy of SHOWEX HF radar wave measurements”. In: *Journal of Atmospheric and Oceanic Technology* 22.7 (2005), pp. 847–859.

[110] Zeng, Y. et al. “Wind speed inversion in high frequency radar based on neural network”. In: *International Journal of Antennas and Propagation* 2016 (2016).

[111] Zhang, J. and Gill, E. W. “Extraction of ocean wave spectra from simulated noisy bistatic high-frequency radar data”. In: *IEEE Journal of Oceanic Engineering* 31.4 (2006), pp. 779–796.

Appendix A

The Surface Roughness Spectrum; $S_s(p, q, wl)$

By the Wiener-Khinchin theorem, the Fourier transform of the autocovariance of the surface height function, f, gives the power spectrum of the surface, $S_s(k_x, k_y, \omega)$. The autocovariance of the surface, $f(x, y, t)$ (given in equation 2.1) is

$$\begin{aligned} R_{x_1,x_2} &= \langle f(x_1, y_1, t_1) f^*(x_2, y_2, t_2) \rangle \\ &= \left\langle \sum_{m,n,l} P(m, n, l) \mathrm{e}^{ia(mx_1+ny_1)-iwlt_1} \sum_{m',n',l'} P^*(m', n', l') \mathrm{e}^{-ia(m'x_2+n'y_2)+iwl't_2} \right\rangle \end{aligned}$$

and, from equation 2.70, R is nonzero only when $m' = m$, $n' = n$ and $l' = l$. Therefore,

$$R_{x_1,x_2} = \sum_{m,n,l} \langle P(m, n, l) P^*(m, n, l) \rangle \, \mathrm{e}^{-ia(m(x_2-x_1)+n(y_2-y_1))-iwl(t_1-t_2)}$$

and setting $x = x_2 - x_1$, $y = y_2 - y_1$ and $\tau = t_2 - t_1$ gives

$$R_{x,y,\tau} = \sum_{m,n,l} \langle P(m, n, l) P^*(m, n, l) \rangle \, \mathrm{e}^{-ia(mx+ny)+iwl\tau}. \tag{A.1}$$

Taking the Fourier transform of equation A.1, i.e.

$$\frac{1}{(2\pi)^3} \iiint_{-\infty}^{\infty} R_{x,y,\tau} \mathrm{e}^{ia(m_0x+n_0y)-iwl_0\tau} \, dx \, dy \, d\tau,$$

then gives the power spectrum of the surface as

$$S_s(m_0,n_0,l_0) = \sum_{m,n,l} \langle P(m,n,l)P^*(m,n,l)\rangle \\ \frac{1}{(2\pi)^3}\iiint_{-\infty}^{\infty} \mathrm{e}^{-ia((m-m_0)x+(n-n_0)y)-iw(l_0-l)\tau}\,dx\,dy\,d\tau. \tag{A.2}$$

The Dirac delta function,

$$\delta(p) = \frac{1}{2\pi}\int_{-\infty}^{\infty} \mathrm{e}^{ipx}\,dx,$$

is used to simplify equation A.2 to give

$$S_s(m_0,n_0,l_0) = \sum_{m,n,l} \langle P(m,n,l)P^*(m,n,l)\rangle \\ \delta(am_0-am)\delta(an_0-an)\delta(wl-wl_0). \tag{A.3}$$

If the sum in equation A.3 is approximated as an integral over m, n and l then

$$S_s(m_0,n_0,l_0) = \iiint_{-\infty}^{\infty} \langle P(m,n,l)P^*(m,n,l)\rangle \\ \delta(am_0-am)\delta(an_0-an)\delta(wl-wl_0)\,dm\,dn\,dl \tag{A.4}$$

and substituting $am = p$, $an = q$ and $wl = \omega$ in to equation A.4 gives

$$S_s(p_0,q_0,wl_0) = \frac{L^2T}{(2\pi)^3}\iiint_{-\infty}^{\infty} \langle P(m,n,l)P^*(m,n,l)\rangle \\ \delta(p_0-p)\delta(q_0-q)\delta(\omega-\omega_0)\,dp\,dq\,d\omega, \tag{A.5}$$

where $a = 2\pi/L$ and $w = 2\pi/T$ have been used. Now, by the sifting property of the delta function, equation A.5 becomes

$$S_s(p_0,q_0,wl_0) = \frac{L^2T}{(2\pi)^3}\langle P(m_0,n_0,l_0)P^*(m_0,n_0,l_0)\rangle$$

for any value of p_0, q_0 and wl_0. This expression can be averaged to give a general expression for p, q and wl, such that

$$S_s(p,q,wl) = \frac{L^2T}{(2\pi)^3}\langle P(m,n,l)P^*(m,n,l)\rangle,$$

which can be rearranged to give the result

$$\langle P(m,n,l)P^*(m,n,l)\rangle = \frac{(2\pi)^3}{L^2T}S_s(p,q,wl). \tag{A.6}$$

Appendix B

Walkthrough of the First Order Radar Cross Section

Each term in equation 2.80 is derived in the same way. A walkthrough of one of the terms - namely $\Phi^{(1)}_{Bx_1C'^*y'_1}$ - is here given as an example. Beginning with the expressions for B, C, x_1 and y_1 from equations 2.53, 2.54, 2.56 and 2.57 respectively;

$$\begin{aligned} B(t_1)x_1C'^*(t_2)y'_1 = &\sum_{mnl} \cos\varphi(k_0 + b(m,n)\cos\theta)\,\mathrm{sinc}(XR)\,\mathrm{sinc}(YR) \\ &(am - k_0)P(m-\nu,n,l)\mathrm{e}^{-i(\omega l+\omega_0)t_1} \\ &\sum_{m'n'l'} \sin\varphi(k_0 + b^*(m',n')\cos\theta)\,\mathrm{sinc}(XR')\,\mathrm{sinc}(YR') \\ &an'P'^*(m'-\nu,n',l')\mathrm{e}^{i(\omega l'+\omega_0)t_2} \end{aligned}$$

and from equation 2.75, $m = m'$, $n = n'$ and $l = l'$ for a non-zero value of $\langle PP^* \rangle$ and so

$$\begin{aligned} \langle B(t_1)x_1C'^*(t_2)y'_1\rangle = &\sum_{mnl} \cos\varphi\sin\varphi(k_0 + b(m,n)\cos\theta)(k_0 + b^*(m,n)\cos\theta) \\ &\mathrm{sinc}^2(XR)\,\mathrm{sinc}^2(YR)an(am-k_0)\mathrm{e}^{-i(\omega l+\omega_0)(t_1-t_2)} \\ &\frac{(2\pi)^3}{L^2T}S_s(am-a\nu,an,\omega l), \end{aligned} \tag{B.1}$$

where $\langle P(m,n,l)P'^*(m,n,l)\rangle = \dfrac{(2\pi)^3 S_s(am,an,wl)}{L^2T}$ has been used. Now, from Thomas [89]

$$\lim_{L\to\infty} L\left(\frac{\sin(XL/2)}{XL/2}\right)^2 = 2\pi\delta(X),$$

and so

$$\lim_{L\to\infty} L\left(\operatorname{sinc}(XR)\right)^2 = 2\pi\delta(k_0\sin\theta\cos\varphi - p) \tag{B.2}$$

and

$$\lim_{L\to\infty} L\left(\operatorname{sinc}(YR)\right)^2 = 2\pi\delta(k_0\sin\theta\sin\varphi - q). \tag{B.3}$$

Furthermore

$$\iiint \frac{(2\pi)^3}{L^2T} S_s(am - a\nu, an, wl)\,dm\,dn\,dl = \iiint S_s(p - k_0\alpha, q, \Omega)\,dp\,dq\,d\Omega, \tag{B.4}$$

by $a = 2\pi/L$ and $w = 2\pi/T$. Therefore, by equations B.2, B.3 and B.4, the limit of equation B.1 is found to be

$$\begin{aligned}\lim_{L\to\infty} L^2\langle B(t_1)x_1C'^*(t_2)y_1'\rangle =& 4\pi^2 \iiint_{-\infty}^{\infty} \cos\varphi\sin\varphi(k_0 + b(p,q)\cos\theta)(k_0 + b^*(p,q)\cos\theta) \\ & q(p-k_0)\delta(k_0\sin\theta\cos\varphi - p)\delta(k_0\sin\theta\sin\varphi - q) \\ & \mathrm{e}^{i(\Omega+\omega_0)\tau} S_s(p - k_0, q, \Omega)\,dp\,dq\,d\Omega,\end{aligned} \tag{B.5}$$

where

$$\tau = t_2 - t_1 \qquad\qquad \Omega = \lim_{T\to\infty} wl.$$

Integrating equation B.5 analytically over p and q using the delta functions gives

$$\begin{aligned}\lim_{L\to\infty} L^2\langle B(t_1)x_1C'^*(t_2)y_1'\rangle =& 4\pi^2\cos\varphi\sin\varphi k_0^4(1+\cos^2\theta)^2(\sin\theta\sin\varphi(\sin\theta\cos\varphi - 1)) \\ & \int_{-\infty}^{\infty} S_s(k_0\sin\theta\cos\varphi - k_0, k_0\sin\theta\sin\varphi, \Omega)\mathrm{e}^{i(\Omega+\omega_0)\tau}\,d\Omega\end{aligned} \tag{B.6}$$

and taking the Fourier transform, as defined in equation 2.66, gives

$$\begin{aligned}\Phi_{Bx_1C'^*y_1'} =& 4\pi^2\cos\varphi\sin\varphi k_0^4(1+\cos^2\theta)^2(\sin\theta\sin\varphi(\sin\theta\cos\varphi - 1)) \\ & \frac{1}{2\pi}\iint_{-\infty}^{\infty} S_s(k_0\sin\theta\cos\varphi - k_0, k_0\sin\theta\sin\varphi, \Omega)\mathrm{e}^{i(\Omega+\omega_0-\omega)\tau}\,d\tau\,d\Omega.\end{aligned} \tag{B.7}$$

Using

$$\delta(p) = \frac{1}{2\pi}\int_{-\infty}^{\infty} \mathrm{e}^{ipx}\,dx, \tag{B.8}$$

equation B.7 becomes

$$\begin{aligned}\Phi_{Bx_1C'^*y'_1} &= 4\pi^2\cos\varphi\sin\varphi k_0^4(1+\cos^2\theta)^2(\sin\theta\sin\varphi(\sin\theta\cos\varphi-1))\\ &\qquad\int_{-\infty}^{\infty} S_s(k_0\sin\theta\cos\varphi-k_0,k_0\sin\theta\sin\varphi,\Omega)\delta(\Omega+\omega_0-\omega)\,d\Omega\\ &= 4\pi^2\cos\varphi\sin\varphi k_0^4(1+\cos^2\theta)^2(\sin\theta\sin\varphi(\sin\theta\cos\varphi-1))\\ &\qquad S_s(k_0\sin\theta\cos\varphi-k_0,k_0\sin\theta\sin\varphi,\omega-\omega_0).\end{aligned} \tag{B.9}$$

By the same method, the other terms are found to be

$$\Phi_{Cy_1B'^*x'_1} = \Phi_{Bx_1C'^*y'_1} \tag{B.10}$$

$$\begin{aligned}\Phi_{Bx_1B'^*x'_1} &= 4\pi^2k_0^4\cos^2\varphi(1+\cos^2\theta)^2(\sin\theta\cos\varphi-1)^2\\ &\qquad S_s(k_0\sin\theta\cos\varphi-k_0,k_0\sin\theta\sin\varphi,\omega-\omega_0)\end{aligned} \tag{B.11}$$

$$\begin{aligned}\Phi_{Cy_1C'^*y'_1} &= 4\pi^2k_0^4\sin^2\varphi(1+\cos^2\theta)^2(\sin\theta\sin\varphi)^2\\ &\qquad S_s(k_0\sin\theta\cos\varphi-k_0,k_0\sin\theta\sin\varphi,\omega-\omega_0)\end{aligned} \tag{B.12}$$

$$\begin{aligned}\Phi_{Dz_1D'^*z'_1} &= 4\pi^2k_0^4\sin^2\theta(\sin\theta\cos\varphi-\sin^2\theta)^2\\ &\qquad S_s(k_0\sin\theta\cos\varphi-k_0,k_0\sin\theta\sin\varphi,\omega-\omega_0)\end{aligned} \tag{B.13}$$

$$\begin{aligned}\Phi_{Bx_1D'^*z'_1} &= -4\pi^2k_0^4\cos\varphi\sin\theta(1+\cos^2\theta)^2(\sin\theta\cos\varphi-\sin^2\theta)(\sin\theta\cos\varphi-1)\\ &\qquad S_s(k_0\sin\theta\cos\varphi-k_0,k_0\sin\theta\sin\varphi,\omega-\omega_0)\end{aligned} \tag{B.14}$$

$$\Phi_{Dz_1B'^*x'_1} = \Phi_{Bx_1D'^*z'_1} \tag{B.15}$$

$$\begin{aligned}\Phi_{Cy_1D'^*z'_1} &= -4\pi^2k_0^4\sin\varphi\sin\theta(1+\cos^2\theta)(\sin\theta\sin\varphi)(\sin\theta\cos\varphi-\sin^2\theta)\\ &\qquad S_s(k_0\sin\theta\cos\varphi-k_0,k_0\sin\theta\sin\varphi,\omega-\omega_0)\end{aligned} \tag{B.16}$$

$$\Phi_{Dz_1C'^*y'_1} = \Phi_{Cy_1D'^*z'_1}. \tag{B.17}$$

Finally, $\sigma^{(1)}(\omega)$ is calculated using equation 2.80. As all of the first order contributions include $4\pi^2k_0^4S_s(k_0\sin\theta\cos\varphi-k_0,k_0\sin\theta\sin\varphi,\omega-\omega_0)$, this will implied throughout the following calculation. Summing equations B.9 through to B.17 gives

$$\begin{aligned}\sum = \big(&\cos\varphi(1+\cos^2\theta)(\sin\theta\cos\varphi-1)+\sin\varphi(1+\cos^2\theta)(\sin\theta\sin\varphi)\\ &-\sin\theta(\cos\varphi\sin\theta-\sin^2\theta)\big)^2\end{aligned}$$

$$= \left(\cos^2\theta(\sin\theta - \cos\varphi) - \cos\varphi + \sin\theta + \sin^2\theta(\sin\theta - \cos\varphi)\right)^2$$
$$= 2^2\left(\sin\theta - \cos\varphi\right)^2.$$

So therefore, on division by π and letting $\theta = 90^\circ$, the first order radar cross section is

$$\sigma^{(1)}(\omega) = 2^4\pi k_0^4\left(1 - \cos\varphi\right)^2 S_s(k_0\cos\varphi - k_0, k_0\sin\varphi, \omega - \omega_0). \tag{B.18}$$

Appendix C

Walkthrough of the Second Order Radar Cross Section

By equation 2.99, the second order radar cross section term is found by calculating

$$\sigma^{(2)}(\omega) = \sigma^{(2)}(\omega)_1 + \sigma^{(2)}(\omega)_2 + \sigma^{(2)}(\omega)_3 + \sigma^{(2)}(\omega)_4, \tag{C.1}$$

for $\sigma^{(2)}(\omega)_i$ in equations 2.95-2.98. To show how to compute each term in equation C.1, the derivation of $\sigma^{(2)}(\omega)_3$ is given; the derivations of the other three terms are analogous. From equation 2.97,

$$\sigma^{(2)}(\omega)_3 = \frac{1}{\pi}\Phi^{(2)}_{-i\zeta b(q,r)\xi'^{*}\Gamma_H}, \tag{C.2}$$

where $\zeta(t) = [B(t)x_1 + C(t)y_1 + D(t)z_1]$ and $\xi(t) = [B(t)x_2 + C(t)y_2 + D(t)z_2]$, for B, C and D given in equations 2.53-2.55 and x_i, y_i and z_i given in equations 2.56-2.58. Therefore, the calculation of equation C.2 can be split into

$$\sigma^{(2)}(\omega)_3 = \frac{1}{\pi}\left(\Phi^{(2)}_{-ib(q,r)\Gamma_H B x_1 B'^{*} x_2'} + \Phi^{(2)}_{-ib(q,r)\Gamma_H C y_1 C'^{*} y_2'} + \Phi^{(2)}_{-ib(q,r)\Gamma_H B x_1 C'^{*} y_2'} + \cdots\right), \tag{C.3}$$

where L^2 and $\langle QQ'^{*}\rangle$ are implied in each of the nine terms, where $\langle QQ'^{*}\rangle$ is the average of four independent random variables, namely

$$\begin{aligned}\langle QQ'^{*}\rangle = \frac{\langle P(q-\nu,r,s)P(m-q,n-r,l-s)}{b(q,r)} \\ \frac{P(\nu-q',-r',-s')P(q'-m',r'-n',s'-l')\rangle}{b^{*}(q',r')}.\end{aligned} \tag{C.4}$$

From equation 2.74,

$$\langle P_1P_2P_3P_4\rangle = \underbrace{\langle P_1P_2\rangle\langle P_3P_4\rangle}_{T_1} + \underbrace{\langle P_1P_3\rangle\langle P_2P_4\rangle}_{T_2} + \underbrace{\langle P_1P_4\rangle\langle P_2P_3\rangle}_{T_3}, \tag{C.5}$$

and, as stated in section 2.4.3, the average, T_1, contributes to specular scatter at zero Doppler and is hence ignored. The second set of conditions, for a non zero average T_2, are

$$\begin{aligned} m &= m' & q &= q' \\ n &= n' & r &= r' \\ l &= l' & s &= s' \end{aligned} \tag{C.6}$$

and the third set, for a non zero average T_3, are

$$\begin{aligned} m &= m' & q' &= m - q + \nu \\ n &= n' & r' &= n - r \\ l &= l' & s' &= l - s. \end{aligned} \tag{C.7}$$

So for each of the nine terms in equation C.3, these two sets of conditions mean that there are 18 terms to calculate to find $\sigma^{(2)}(\omega)_3$. Repeating the process for each of the four terms in equation C.1, means that there are 72 calculations in total. To speed up the process, we can exploit the fact that each term consists of the same fundamental terms.

The structure, say χ, of each term is

$$\begin{aligned} \chi = L^2 &\sum_{mnl} f_1(m,n)\,\mathrm{sinc}(XR)\,\mathrm{sinc}(YR)\mathrm{e}^{-i(\omega l+\omega_0)t_1} \sum_{qrs} g_1(m,n,q,r) \\ &\sum_{m'n'l'} f_2(m',n')\,\mathrm{sinc}(XR')\,\mathrm{sinc}(YR')\mathrm{e}^{i(\omega l'+\omega_0)t_2} \sum_{q'r's'} g_2(m',n',q',r') \\ &\frac{Q(m,n,l,q,r,s)Q'^*(m',n',l',q',r',s')}{b(q,r)b^*(q',r')}, \end{aligned} \tag{C.8}$$

where f_1 and f_2 both represent one of B, C and D, excluding the sinc and $\mathrm{e}^{-i(wl+\omega_0)t}$ terms which have been included separately, and g_1 and g_2 both represent one of x_i, y_i and

z_i. Under the second set of conditions, given in equation C.6, the average of equation C.8 is

$$\begin{aligned}\langle\chi\rangle_2 = L^2 \sum_{mnl} & f_1(m,n) f_2(m,n) \operatorname{sinc}^2(XR) \operatorname{sinc}^2(YR) \\ & \sum_{qrs} g_1(m,n,q,r) g_2(m,n,q,r) \mathrm{e}^{i(\omega l + \omega_0)\tau} \\ & \left(\frac{(2\pi)^3}{L^2 T}\right)^2 \frac{S_s(aq - a\nu, ar, ws) S_s(am - aq, an - ar, wl - ws)}{b(q,r) b^*(q,r)},\end{aligned} \tag{C.9}$$

where $\tau = t_2 - t_1$. Taking the limit of equation C.9 as $L \to \infty$, using the relations

$$\begin{aligned} aq &\to p & am &\to p' \\ ar &\to q & an &\to q' \\ ws &\to \Omega & wl &\to \Omega' \\ a\nu &\to k_0 & b(m,n) &\to k_0 \gamma, \\ L \operatorname{sinc}^2(xL/2) &\to 2\pi\delta(x) \end{aligned} \tag{C.10}$$

gives

$$\begin{aligned}\lim_{L\to\infty} \langle\chi\rangle_2 = 2^2\pi^2 \int \cdots \int_{-\infty}^{\infty} & F_1(p',q') F_2(p',q') \delta(k_0 \sin\theta\cos\varphi - p') \delta(k_0 \sin\theta \sin\varphi - q') \\ & G_1(p',q',p,q) G_2(p',q',p,q) \mathrm{e}^{i(\Omega' + \omega_0)\tau} \\ & \frac{S_s(p - k_0, q, \Omega) S_s(p' - p, q' - q, \Omega' - \Omega)}{b(p,q) b^*(p,q)} \, dp \, dq \, d\Omega \, dp' \, dq' \, d\Omega',\end{aligned} \tag{C.11}$$

where F_1, F_2, G_1 and G_2 are the functions f_1, f_2, g_1 and g_2 with the limit taken. The delta functions in equation C.11 can then be used to evaluate the integrals over p' and q'. So letting $p' = k_0 \sin\theta\cos\varphi$ and $q' = k_0 \sin\theta\sin\varphi$ gives

$$\begin{aligned}\lim_{L\to\infty} \langle\chi\rangle_2 = 2^2\pi^2 \iiiint_{-\infty}^{\infty} & F_1(\theta,\varphi) F_2(\theta,\varphi) G_1(k_0 \sin\theta\cos\varphi, k_0 \sin\theta\sin\varphi, p, q) \\ & \frac{S_s(p - k_0, q, \Omega) S_s(k_0 \sin\theta\cos\varphi - p, k_0 \sin\theta\sin\varphi - q, \Omega' - \Omega)}{b(p,q) b^*(p,q)} \\ & G_2(k_0 \sin\theta\cos\varphi, k_0 \sin\theta\sin\varphi, p, q) \mathrm{e}^{i(\Omega' + \omega_0)\tau} \, dp \, dq \, d\Omega \, d\Omega'.\end{aligned} \tag{C.12}$$

Taking the Fourier transform of equation C.12, using the definition of the delta function (defined in equation B.8) to integrate the result over Ω' and then dividing the result by π

gives

$$\begin{aligned}\Phi_{\chi,2} = 2^2\pi \iiint & F_1(\theta,\varphi)F_2(\theta,\varphi)G_1(k_0\sin\theta\cos\varphi, k_0\sin\theta\sin\varphi, p, q) \\ & \frac{S_s(p-k_0,q,\Omega)S_s(k_0\sin\theta\cos\varphi-p, k_0\sin\theta\sin\varphi-q, -\omega_0+\omega-\Omega)}{b(p,q)b^*(p,q)} \\ & G_2(k_0\sin\theta\cos\varphi, k_0\sin\theta\sin\varphi, p, q)\,dp\,dq\,d\Omega.\end{aligned} \tag{C.13}$$

For each f and g term that the radar cross section is calculated for, the respective F and G terms are

$$\begin{aligned} x_1 = x_1' &\to k_0(\sin\theta\cos\varphi - 1) \\ y_1 = y_1' &\to k_0\sin\theta\sin\varphi \\ z_1 = z_1' &\to k_0^2(\sin\theta\cos\varphi - \sin^2\theta) \\ x_2 = x_2' &\to k_0\left((k_0\sin\theta\cos\varphi - p)(k_0 - p) + (1-\sin\theta\cos\varphi)b^2(p,q)\right) \\ y_2 = y_2' &\to k_0\left((k_0\sin\theta\sin\varphi - q)(k_0 - p) - \sin\theta\sin\varphi)b^2(p,q)\right) \\ z_2 = z_2' &\to k_0^2((p-k_0)(k_0\sin^2\theta - p\sin\theta\cos\varphi - q\sin\theta\sin\varphi) \\ &\qquad + (\sin^2\theta - \sin\theta\cos\varphi)b^2(p,q)) \\ B = B' &\to k_0\cos\varphi(1+\cos^2\theta) \\ C = C' &\to k_0\sin\varphi(1+\cos^2\theta) \\ D = D' &\to -\sin\theta. \end{aligned} \tag{C.14}$$

A similar process, using the third set of conditions from equation C.7, shows that

$$\begin{aligned}\Phi_{\chi,3} = 2^2\pi \int_{-\infty}^{\infty}\iiint & F_1(\theta,\varphi)F_2(\theta,\varphi)\mathcal{G}_1(k_0\sin\theta\cos\varphi, k_0\sin\theta\sin\varphi, p, q) \\ & \frac{S_s(p-k_0,q,\Omega)S_s(k_0\sin\theta\cos\varphi-p, k_0\sin\theta\sin\varphi-q, -\omega_0+\omega-\Omega)}{b(p,q)b^*(k_0\sin\theta\cos\varphi-p+k_0, k_0\sin\theta\sin\varphi-q)} \\ & \mathcal{G}_2(k_0\sin\theta\cos\varphi, k_0\sin\theta\sin\varphi, p, q)\,dp\,dq\,d\Omega,\end{aligned} \tag{C.15}$$

where $\mathcal{G}_1$ and $\mathcal{G}_2$ denote the relevant expressions for the transformed g_1 and g_2 functions using the third set of conditions. The values for F_1 and F_2 remain the same. In fact, only the transformed values of x_2', y_2' or z_2' are different under the third set of conditions. They

are

$$\begin{aligned} x_2' &\to k_0\left((k_0\sin\theta\cos\varphi - p)(k_0 - p) + (1 - \sin\theta\cos\varphi)b^2(\eta,\psi)\right) \\ y_2' &\to k_0\left(q(p - k_0\sin\theta\cos\varphi) - \sin\theta\sin\varphi)b^2(\eta,\psi)\right) \\ z_2' &\to k_0^2((k_0\sin\theta\cos\varphi - p)(\sin\theta\cos\varphi(p - k_0) + q\sin\theta\sin\varphi) \\ &\qquad + (\sin^2\theta - \sin\theta\cos\varphi)b^2(\eta,\psi)), \end{aligned} \tag{C.16}$$

where, for convenience,

$$\eta = k_0\sin\theta\cos\varphi - p + k_0 \qquad\qquad \psi = k_0\sin\theta\sin\varphi - q. \tag{C.17}$$

To find the value of $\sigma^{(2)}(\omega)_3$, each combination of the terms alluded to in equation C.3 is substituted into equations C.13 and C.15 and then the results summed. Note that each term contributing to $\sigma^{(2)}(\omega)_3$ includes a factor of $b(q,r)$, which transforms to $b(p,q)$. Therefore, the factor of $b(p,q)$ in the denominator of equation C.8 cancels and hence there are no $b(p,q)$ terms in the denominators of the resulting forms of $\Phi_{\chi,2}$ and $\Phi_{\chi,3}$. Furthermore, each term is multiplied by $-i\Gamma_H$. In the case of $\Phi^{(2)}_{-ib(p,q)\Gamma_H Bx_1C^*y_2'}$, substituting the values for B, C, x_1 and y_2' from equation C.14 into equation C.13 gives the contribution from the second set of conditions as

$$\begin{aligned} \Phi^{(2)}_{[-ib(q,r)\Gamma_H Bx_1C'^*y_2'],2} = -2^2\pi i \iiint_{-\infty}^{\infty} &\Gamma_H k_0^4\cos\varphi\sin\varphi(1+\cos^2\theta)^2(\sin\theta\cos\varphi - 1) \\ &\frac{S_s(p - k_0, q, \Omega)S_s(k_0\sin\theta\cos\varphi - p, k_0\sin\theta\sin\varphi - q, -\omega_0 + \omega - \Omega)}{b^*(p,q)} \\ &\left((k_0\sin\theta\sin\varphi - q)(k_0 - p) - \sin\theta\sin\varphi)b^2(p,q)\right)\, dp\, dq\, d\Omega. \end{aligned}$$

Substituting the same values for B, C and x_1 into equation C.15, along with the value for y_2' from equation C.16, gives

$$\begin{aligned} \Phi^{(2)}_{[-ib(q,r)\Gamma_H Bx_1C'^*y_2'],3} = -2^2\pi i \iiint_{-\infty}^{\infty} &\Gamma_H k_0^4\cos\varphi\sin\varphi(1+\cos^2\theta)^2(\sin\theta\cos\varphi - 1) \\ &\frac{S_s(p - k_0, q, \Omega)S_s(k_0\sin\theta\cos\varphi - p, k_0\sin\theta\sin\varphi - q, -\omega_0 + \omega - \Omega)}{b^*(k_0\sin\theta\cos\varphi - p + k_0, k_0\sin\theta\sin\varphi - q)} \\ &\left(q(p - k_0\sin\theta\cos\varphi) - \sin\theta\sin\varphi)b^2(\eta,\psi)\right)\, dp\, dq\, d\Omega, \end{aligned}$$

Upon calculating the other combinations of terms, in much the same way, and letting $\theta = 90^\circ$ for grazing incidence, the results are summed to give the contribution from the second set of

conditions as

$$\Phi_{3,2}^{(2)} = -2^4 k_0^4 \pi i (1-\cos\varphi) \iiint_{-\infty}^{\infty} \Gamma_H \frac{\big((k_0-p)(k_0-p\cos\varphi-q\sin\varphi)-(1-\cos\varphi)b^2(p,q)\big)}{b^*(p,q)}$$
$$S_s(p-k_0,q,\Omega) S_s(k_0\cos\varphi-p, k_0\sin\varphi-q, -\omega_0+\omega-\Omega)\,dp\,dq\,d\Omega,$$

and, from the third set, as

$$\Phi_{3,3}^{(2)} = -2^4 k_0^4 \pi i (1-\cos\varphi) \iiint_{-\infty}^{\infty} \Gamma_H \frac{\big((k_0\cos\varphi-p)(\cos\varphi(k_0-p)-q\sin\varphi)-(1-\cos\varphi)b^2(\eta,\psi)\big)}{b^*(k_0\cos\varphi-p+k_0, k_0\sin\varphi-q)}$$
$$S_s(p-k_0,q,\Omega) S_s(k_0\cos\varphi-p, k_0\sin\varphi-q, -\omega_0+\omega-\Omega)\,dp\,dq\,d\Omega.$$

Letting

$$a_1 = (k_0-p)(k_0-p\cos\varphi-q\sin\varphi)-(1-\cos\varphi)b^2(p,q),$$

$$a_2 = (k_0\cos\varphi-p)(\cos\varphi(k_0-p)-q\sin\varphi)-(1-\cos\varphi)b^2(\eta,\psi),$$

$$b_1 = b(p,q)$$

and

$$b_2 = b(k_0\cos\varphi-p+k_0, k_0\sin\varphi-q),$$

the sum of $\Phi_{3,2}^{(2)}$ and $\Phi_{3,3}^{(2)}$ is

$$\Phi_3^{(2)}(\omega) = -2^4 k_0^4 \pi i (1-\cos\varphi) \iiint_{-\infty}^{\infty} \Gamma_H \left(\frac{a_1}{b_1^*}+\frac{a_2}{b_2^*}\right) S_s(p-k_0,q,\Omega) \tag{C.18}$$
$$S_s(k_0\cos\varphi-p, k_0\sin\varphi-q, -\omega_0+\omega-\Omega)\,dp\,dq\,d\Omega.$$